

Spectroscopic Studies on Interaction of Silica and Metallic Nano Particles with Dyes of Biomedical Significance

By

Beena Jain

Enrolment No. PHYS03200704009

Raja Ramanna Centre for Advanced Technology,

Indore-452013, India

A thesis submitted to the

Board of Studies in Physical Sciences

In partial fulfillment of requirements

For the Degree of

DOCTOR OF PHILOSOPHY

of

HOMI BHABHA NATIONAL INSTITUTE



August, 2013

Homi Bhabha National Institute

Recommendations of the Viva Voce Board

As members of the Viva Voce Board, we certify that we have read the dissertation prepared by **Beena Jain** entitled “**Spectroscopic studies on interaction of silica and metallic nano particles with dyes of biomedical significance**” and recommend that it may be accepted as fulfilling the dissertation requirement for the Degree of Doctor of Philosophy.

P. K. Gupta

Date: 17.01.14.

Chairman – Dr. P. K. Gupta

Shailendra Kumar

Date: 17/1/14

Guide / Convener -Dr. S. Kumar

Dr. D. K. Palit

Date: 17/01/2014

Member – Dr. D. K. Palit

Kaushik Das

Date: 17/1/14

Technical Guide – Dr. K. Das

Anindya Datta

Date: 17/01/2014

External Examiner – Dr. Anindya Datta

Final approval and acceptance of this dissertation is contingent upon the candidate's submission of the final copies of the dissertation to HBNI.

I hereby certify that I have read this dissertation prepared under my direction and recommend that it may be accepted as fulfilling the dissertation requirement.

Date: 17/1/2014

Guide: *Shailendra Kumar*

(Dr. Shailendra Kumar)

Place: Indore, RRCAT.

STATEMENT BY AUTHOR

This dissertation has been submitted in partial fulfillment of requirements for an advanced degree at Homi Bhabha National Institute (HBNI) and is deposited in the Library to be made available to borrowers under rules of the HBNI.

Brief quotations from this dissertation are allowable without special permission, provided that accurate acknowledgement of source is made. Requests for permission for extended quotation from or reproduction of this manuscript in whole or in part may be granted by the Competent Authority of HBNI when in his or her judgment the proposed use of the material is in the interests of scholarship. In all other instances, however, permission must be obtained from the author.

Beena Jain

(Beena Jain)

DECLARATION

I, hereby declare that the investigation presented in the thesis has been carried out by me. The work is original and has not been submitted earlier as a whole or in part for a degree / diploma at this or any other Institution / University.

Beena Jain

(Beena Jain)

I dedicate this work to my family

and

the 'Mother Nature'

ACKNOWLEDGEMENTS

Although this thesis describes the work carried out during the last five years only, the background knowledge which was involved had been gained right from my childhood. Therefore, first of all I thank all my 'gurus', from the bottom of my heart, for the knowledge and confidence they provided in me to take up this research work.

It is my pleasure to acknowledge here the efforts of many people who have made possible the work described in this thesis.

I am highly obliged and thankful to Prof. P. K. Gupta who encouraged and supported me to pursue this research work. I wish to record my deepest gratitude to Dr. K. Das, my technical guide, for his erudite guidance and active support all through this work. I am extremely grateful to Dr S. Kumar, for accepting himself as my guide and for his constant encouragement and moral support. I am grateful to Prof. D. K. Palit, BARC, and all the members of my Ph.D. committee, for their constructive criticism, guidance and motivation.

I owe thanks to Dr. A. Uppal for her help in nanoparticle preparation and in the cell work and to Dr. R. Shrivastava, Sh. H. S. Patel, Sh. M. Swami and B. Bose for their participation in different experiments. I would like to give especial thanks to Dr. A. Dube for providing the photosensitizers for the experiments and Dr. A. Shrivastava and Shri P. Mondal for TEM imaging of the nanoparticles.

I would like to thank all my lab members including Dr. K. D. Rao, Dr. S. K. Majumder, Dr. M. Sharma, Dr. R. Dasgupta, Dr. Y. Verma, Mr. K. Sahu, Mr. R. Verma, Mrs. S. Ahlawat and Mrs. H. Bansal for creating a healthy scientific atmosphere in the labs which helped me to bring this thesis to its present status. I wish to thank all other members of Laser Biomedical Applications and Instrumentation Division for their help.

I am thankful to my friends Dr. B. N. Rajasheker, Dr. R. Chari, Dr. A. Ingale, Mrs. S. Joshi, Mrs. A. Mokhariwale and many others who were always there to give me moral support during the course of this thesis.

I would like to convey my deepest regards to my parents for their never-ending love and their enormous encouragement and support which motivated me in my academic growth. I am thankful to sisters, my aunts and uncles, my in-laws, for their love and affection and especially to my bhuaji, for her selfless support and encouragement. I want to thank, my lovely son Ashish and inquisitive daughter Garima, who are a constant source of joy, for allowing me free to use their part of precious time for this research work. Finally, I want to express my greatest appreciation for my husband Shri Girish Kumar Jain, for his support and sacrifice.

Beena Jain

Table of Contents

Synopsis	1
List of Publications	8
List of Figures	10
List of Tables.....	15
CHAPTER 1.....	16
1 INTRODUCTION.....	16
1.1 Introduction and historical background.....	16
1.2 Properties of nanoparticles	18
1.3 Biomedical Applications	18
1.4 Silica NP and their applications:	21
1.4.1 Organically modified silica (ORMOSIL) nanoparticles.....	23
1.5 Metal NPs	26
1.5.1 Gold NPs	28
1.5.2 Gold nanorods and Photothermal processes.....	29
1.6 Excited state processes	32
1.7 Experimental plan.....	36
1.8 Outline of the thesis.....	38
CHAPTER 2.....	40
2 EXPERIMENTAL DETAILS	40
2.1 Synthesis of NPs.....	40
2.1.1 ORMOSIL NP (SiNP-V, SiNP-VA).....	40
2.1.2 Gold Nanorods	42
2.1.3 Polymeric ((poly(lactic- <i>co</i> -glycolic) acid (PLGA)) NP.....	43
2.1.4 Liposomes	44
2.2 Characterization of NPs.....	44
2.2.1 Transmission Electron Microscopy	44
2.2.2 Hydrodynamic radius measurement.....	47
2.2.3 Zeta potential measurements.....	48
2.2.4 FTIR spectroscopy	50

2.3	UV-visible spectroscopy	54
2.3.1	Absorption spectroscopy	54
2.3.2	Emission spectroscopy	54
2.3.3	Fluorescence lifetime measurement	54
2.4	MTT Assay, to determine the cell survival	57
2.5	Molarity calculation of the NPs.....	57
2.6	Conclusion.....	58
CHAPTER 3.....		59
3 PHOTOPHYSICAL STUDIES ON THE INTERACTION OF ANS, TNS & MC540 WITH ORMOSIL NANOPARTICLES		59
3.1	Introduction	59
3.2	Experimental Methodology	62
3.3	Results and Discussion	63
3.3.1	Spectroscopic studies of ANS and TNS with SiNP-V and SiNP-VA	64
3.3.2	Spectroscopic studies of MC540 with SiNP-VA.....	71
3.3.3	Light induced photostability and phototoxicity of MC540 and its SiNP complex	74
3.4	Conclusion.....	76
CHAPTER 4.....		77
4 INTERACTION OF CHLORIN P₆ WITH SiNP-VA: PHOTOPHYSICAL AND PHOBIOLOGICAL STUDIES		77
4.1	Introduction	78
4.2	Experimental Details	80
4.3	Results	83
4.3.1	Effect of SiNP on the absorption and emission of Cp ₆ from pH 8.0 to 3.0... ..	83
4.3.2	FCS studies of the free Cp ₆ and Cp ₆ -SiNP complex.....	90
4.3.3	Intracellular uptake, localization and phototoxicity of free Cp ₆ and its SiNP complex	91
4.3.4	Relative photo-stability of the free Cp ₆ and Cp ₆ -SiNP complex	93
4.4	Discussion	94
4.5	Conclusion.....	99

CHAPTER 5.....	101
5 SPECTROSCOPIC INVESTIGATION OF CONVERSION OF PURPURIN 18 TO CHLORIN P₆ IN THE PRESENCE OF SILICA, LIPOSOME & POLYMERIC NPs	101
5.1 Introduction	102
5.2 Experimental details	104
5.3 Results and Discussion	105
5.4 Conclusion.....	112
CHAPTER 6.....	117
6 SPECTROSCOPIC STUDIES ON METHYLENE BLUE AND NILE BLUE BOUND TO COATED GOLD NANORODS	117
6.1 Introduction	118
6.2 Experimental Details	118
6.2.1 Absorption & Fluorescence spectroscopy.....	119
6.3 Results	120
6.3.1 Absorption properties of dye-AuNR systems	121
6.3.2 Fluorescence properties of the dye-AuNR systems	124
6.4 Discussion	128
6.5 Conclusion.....	132
CHAPTER 7.....	133
7 PHOTOPHYSICAL PROPERTIES OF CHLORIN P₆ BOUND TO COATED GOLD NANORODS.....	133
7.1 Introduction	133
7.2 Experimental Details	135
7.3 Results	136
7.4 Discussion	141
7.5 Conclusion.....	143
CHAPTER 8.....	145
8 CONCLUSION.....	145
REFERENCES	149

Synopsis

There is considerable current research interest in the use of biocompatible dielectric and metallic nanoparticles (NPs) for applications like biomedical imaging, diagnosis and therapy. NPs can be loaded with the dyes/drugs or genes and also functionalized for targeting specific cells/ cellular sites thus improving the diagnostic and therapeutic efficiency. Organically modified silica nanoparticles (SiNP) have been used as carrier of hydrophobic dyes/drugs and genetic materials in cells and animal models [1, 2]. These NPs are amphiphilic in nature having a hydrophobic core, and their surface is charged depending upon the silica precursors, used to synthesize them. Therefore, there is a possibility of electrostatic binding with oppositely charged molecules at the NP surface. While SiNP (size~30 nm) are transparent in the visible region metal NPs show localized surface plasmon resonance (LSPR) ranging from UV to NIR region (depending on the metal type, size, shape, structure, composition and also the dielectric constant of the environment). The strong SP fields enhance their extinction coefficients by 5-6 orders of magnitude (per NP) as compared to strongly absorbing/fluorescing organic dye molecules [3]. These NPs can therefore be used as contrast agents with the added advantage that in contrast to fluorescent probes these do not get bleached under long exposure. Since LSPR is sensitive to the surrounding environment, these NPs have also been used for sensing applications. As gold is inert, its NPs are being actively explored for imaging and therapeutic applications. Among the different shapes of gold NPs, gold nanorods show highest extinction coefficient. Their longitudinal surface plasmon (L-SP) band can be tuned from visible to NIR region, by a change in their aspect ratio. These are therefore

also being studied for photothermal effects. However, rods are commonly synthesized in the template of a surfactant, cetyltrimethylammonium bromide (CTAB), which has been shown to be potentially toxic. Therefore, these need to be coated with biocompatible polymers to minimize this toxicity. These polymers are generally charged and therefore offer the possibility of electrostatic interaction with the oppositely charged dyes/drugs. It should be noted that binding of a dye/drug to NPs may lead to some changes in its photophysical and photochemical properties and thus may affect its functionality. We have therefore, investigated the changes in the photophysical properties of dyes as a consequence of binding to the NP surface. The results of our investigations on several dyes of biomedical significance are presented in this thesis.

Interaction of SiNP with two sets of dyes was investigated. The first set included dyes, such as 8-anilino-1-naphthalenesulfonate (ANS), 6-p-toluidino-2-naphthalenesulphonate (TNS) and Merocyanine 540 (MC540), which are negatively charged polarity sensitive dyes. These dyes undergo structural changes in their excited states in polar medium due to electron re-distribution and dominantly decay non-radiatively. As a consequence, these are weakly fluorescent in aqueous medium. Studies on the interaction of these dyes with SiNPs, having positive charge on their surface, form the first part of the thesis. Significant shifts in the absorption and emission peak positions and enhancement in their fluorescence intensity was observed on binding of these dyes with SiNPs. This was attributed to the suppression of the excited state charge transfer process in case of ANS and TNS. In case of MC540, which is also a photodynamically active dye, the excited state photoisomerism process is suppressed due to binding to SiNP. This resulted in enhanced phototoxicity of the dye-NP complex against cancer cells in-vitro.

Another set of dyes studied were porphyrin type photosensitizers Chlorin p_6 (Cp_6) and purpurin 18 (PP18). Both are interesting photosensitizers because these have significant absorption in the longer wavelength (650-900 nm) where tissue absorb and

scatter weakly and provide high singlet oxygen yield. Cp_6 is amphiphilic and negatively charged at physiological pH due to the presence of three carboxylic acid groups. Electrostatic binding of this drug to SiNP leads to an increase in its photostability and is the probable cause for higher phototoxicity against cancer cells. Although PP18 absorbs strongly than Cp_6 in the therapeutic window, its use as a drug for photodynamic therapy (PDT) is limited by the fact that it is hydrophobic and therefore needs carrier to get solubilized in aqueous medium. However, in aqueous medium this gets converted to Cp_6 due to hydrolysis of its anhydride ring. Suitability of SiNP as carriers of PP18 in aqueous media was investigated by studying its time dependent conversion to Cp_6 . This forms the second part of the thesis.

In the last part of the thesis, results on studies on the effect of large localized fields generated due to longitudinal surface plasmon resonance (L-SP) of polymer coated gold nanorods on the absorption and emission properties of molecules attached on their surface are presented. For these studies the L-SP peak of the gold nanorods was tuned to resonance or off-resonance with respect to the absorption maximum of Methylene Blue (MB) and Nile Blue (NB). L-SP peak tuning showed significant change in the spectroscopic properties of MB and NB due to coupling between L-SP and molecular absorption. On the other hand, the spectroscopic properties of Cp_6 , which does not have an absorption maximum near the L-SP were observed to depend upon the chemical nature and thickness of the polymeric coatings over the gold nanorod.

The organization of the thesis is as follows:

Chapter 1: In this chapter a brief introduction on importance of nanoparticles in biomedical applications is given. The interest in silica NPs, especially ORMOSIL NPs and their use for drug encapsulation and delivery is reviewed. Possible effect of electrostatic interaction with NP on the photophysical properties of fluorophores/photosensitizers is discussed. Work carried out by different groups on the

size, shape and composition dependent surface plasmon resonance properties of gold nanostructures is reviewed. Biomedical applications of gold nanorods and the possible effect of their LSPR on the photophysical properties of fluorophores/photosensitizers attached to them are discussed.

Chapter 2: In this chapter details of the preparation procedure of the ORMOSIL NPs and gold nanorods and subsequently their characterization are given. NPs were prepared in the micellar core of surfactants following the wet chemical methods available in the literature. These were characterized for their size and polydispersity by transmission electron microscopy imaging as well as light scattering methods. The surface charge and coatings were characterized by Zeta potential measurements and Fourier transform infra-red spectroscopy respectively. Dye-NP interaction was studied by both steady state absorption and fluorescence spectroscopy and time resolved emission spectroscopy. Fluorescence correlation spectroscopy was also done to study the binding of dye to SiNP in serum media. Brief principles of these techniques along with the instrument details are discussed in this chapter.

Chapter 3: Results of the studies on the interaction of ANS and TNS and MC540 with SiNP-V (NP, prepared with silica precursor vinyl-triethoxysilane (VTES)) and SiNP-VA (NP, prepared with silica precursor VTES and 3-aminopropyl-triethoxysilane (APTS)) in aqueous media are presented in this chapter. ANS and TNS are very weakly fluorescent in aqueous medium at physiological pH. In the presence of SiNP-VA, a significant enhancement of the fluorescence yield of the dyes was observed. This has been attributed to the suppression of the charge transfer process from aniline group (for ANS) and p-toluidino group (for TNS) to the sulphonate group after binding to the positively charged amino groups at the SiNP surface due to electrostatic interaction. In comparison to protein environment, however, the fluorescence of the two dyes was observed to be significantly decreased in the NP environment. A comparison of radiative

and non-radiative decay rates indicated that this quenching was primarily static in nature however, time resolved fluorescence anisotropy decay measurements showed that the quenching mechanism was probe dependent in the nanoparticle environment. Our absorption/emission studies on MC540 showed that the fluorescence and photostability of the dye significantly increases when bound to SiNP-VA. This is attributed to suppression in the excited state photoisomerism process (around its central double bond in aqueous medium) due to binding. The efficacy of this dye-nanoparticle complex was also tested on cancer cells where it showed higher light induced toxicity as compared to the free dye. Details of the study are described in this chapter.

Chapter 4: In this chapter we describe studies on the pH dependent aggregation behavior of Cp_6 in the presence of SiNP-VA suspended in aqueous medium. The absorption and fluorescence properties of the dye in the presence of SiNP-VA indicated that the electrostatic binding of dye with SiNP results in significant change in the acid-base equilibrium of Cp_6 . Subsequently, phototoxicity, on cancer cell lines, due to Cp_6 -SiNP complex and free Cp_6 was compared which showed a significant increase in the phototoxicity due to the Cp_6 -SiNP complex. Details of the study are described in this chapter.

Chapter 5: In this chapter four different NPs have been studied as delivery vehicle for hydrophobic PP18. Since PP18 has high absorption coefficient at longer wavelengths (650-720 nm) it may be more suitable for PDT applications as compared to its hydrolytic product Cp_6 provided a suitable delivery vehicle is established. We have spectroscopically studied and compared the conversion of PP18 to Cp_6 as a function of time over the period of 24 hrs in NPs: SiNP-V, SiNP-VA, polymeric NP (prepared using polymer PLGA) and liposomes (prepared using phosphatidylcholine). Our results indicate that the conversion is least in SiNP-V and highest in liposome. The details of the study are described in the chapter.

Chapter 6: In this chapter, the effect of L-SP electric field of gold nanorods on the absorption and emission properties of two positively charged dyes MB and NB has been studied as a function of detuning the L-SP band from the absorption maxima of the dyes. Binding between dyes and nanorods were established by electrostatic interaction by making the nanorods negatively charged after coating them with polymer polystyrene sulphonate (PSS). Both the absorption and emission properties of the dyes conjugated to the rods were found to get modified due to the SP field coupling as well as the aggregation of the dyes on the NP surface. The details of the study are described in the chapter.

Chapter 7: In this chapter, the results of the effect of different coating materials (surfactant CTAB and polymers) and L-SP of gold nanorods on the photophysical properties of Cp_6 electrostatically bound to these coated rods are presented. For this the CTAB coated rods were first coated with PSS to make their surface negatively charged and then coated with positively charged polymers PDDAC & PAH. While the spectroscopic properties of the Cp_6 were observed to depend upon the nature of the coatings, no significant effect due to LSPR peak position, with respect to the Cp_6 'Q band' absorption peak, was observed. The radiative decay rate was found to be different and decreased in all the three coated rods and was attributed to the difference in the chemical nature of coatings. However, the nonradiative decay rate was found to increase in the case of CTAB coated rods while no change was observed in the case of PAH and PDDAC coated rods. This was attributed to distance dependent energy transfer between the drug and nanorod, which decreased as the coating thickness increased. In addition the photobleaching rate of Cp_6 conjugated to these rods was also found to be significantly decreased and coating dependent. These results suggest that the coatings on the rods should be appropriately done depending on the applications. Details of these studies will be described in the chapter.

Chapter 8 presents the conclusions with a summary of the results and a brief discussion on possible future work.

References:

1. R. Kumar, I. Roy, Tymish, Y. Ohulchanskyy, L. A. Vathy, E. J. Bergey, M. Sajjad and P. N. Prasad, “In vivo biodistribution and clearance studies using multimodal ORMOSIL nanoparticles”, *ACS Nano* **4**, 699 (2010).
2. I. Roy, “ORMOSIL nanoparticles. Nanomedicine approach for drug/gene delivery to the brain”, Book chapter 5, *Nanotechnology in health care*, Ed. by S. K. Sahoo, Pan Stanford publishing 201–214 (2012).
3. E. C. Dreaden, A. M. Alkilany, X. Huang, C. J. Murphy and M. A. El-Sayed, “The golden age: gold nanoparticles for biomedicine”, *Chem. Soc. Rev.* **41**, 2740 (2012).

List of Publications

Journals Articles

(Included in the thesis)

1. 'Conversion of Purpurin 18 to Chlorin p_6 in the presence of liposome, silica and polymeric nanoparticles: A spectroscopic study',
B. Jain, A. Uppal, K. Das, A. Dube and P. K. Gupta.
J. Mol. Struct. **1060**, 24–29 (2014).
2. 'Evaluation of photodynamic efficacy of Chlorin p_6 bound to amine modified silica nanoparticles in Colon and Oral cancer cell lines',
A. Uppal, **B. Jain**, M. K. Swami, H. S. Patel, A. Dube, P. K. Gupta and K. Das,
In press, *BioNanoScience*.
3. 'Photophysical properties of Chlorin p_6 bound to coated gold nanorods'.
B. Jain, A. Uppal, P. K. Gupta and K. Das.
J. Mol. Struct. **1032**, 23–28 (2013).
4. 'Spectroscopic investigations on the binding of Methylene Blue and Nile Blue to negatively charged gold nanorods.'
R. Shrivastava, **B. Jain** and K. Das.
J. Mol. Struct. **1020**, 56–62 (2012).
5. 'Interaction of ANS and TNS with organically modified silica nanoparticles in aqueous media.'
B. Jain, A. Uppal, P. K. Gupta and K. Das.
Adv. Sci. Lett. **3**, 225-230 (2010).
6. 'Light induced toxicity of Merocyanine 540–silica nanoparticle complex.'
K. Das, A. Uppal, **B. Jain**, B. Bose and P. K. Gupta.
J. Nanosci. Nanotech. **9**, 1-4 (2009).
7. 'Spectroscopic investigations on the binding of the photosensitizer Chlorin p_6 with amine modified silica nanoparticles in aqueous media'.
B. Jain, A. Uppal, P. K. Gupta and K. Das.
Photochem. Photobiol. **85**, 927-933 (2009).

(Not included in the thesis)

1. 'Photodynamic action of Rose Bengal silica nanoparticle complex on breast and oral cancer cell lines'.
A. Uppal, **B. Jain**, P. K. Gupta and K. Das.
Photochem. Photobiol. **87**, 1146-51 (2011).
2. 'NIR femtosecond Laser induced hyper-Rayleigh scattering and luminescence from silver nanoprisms.'
B. Jain, A. K. Srivastava, A. Uppal, P. K. Gupta and K. Das.
J. Nanosci. Nanotech. **10**, 5826-5830 (2010).

Conference Presentations / Publications:

1. 'Spectroscopic investigations on the binding of dyes to negatively charged gold nanorods.'
R. Shrivastava, **B. Jain** and K. Das,
Proceedings of DAE-BRNS National Laser Symposium, held at Chennai (2012).
2. 'Evaluation of photodynamic efficacy of Chlorin p_6 bound to amine modified silica nanoparticles in Colon and Oral cancer cell lines.'
A. Uppal, **B. Jain**, A. Dube, K. Das and P. K. Gupta.
Proceedings of DAE-BRNS National Laser Symposium, held at Indore (2010).
3. 'Interaction of organically modified silica nanoparticles with molecules of biomedical relevance.'
B. Jain, A. Uppal, K. Das, B. Bose and P. K. Gupta.
Indo-US Workshop on Science and Technology at the Nano-interface, held at Bhubanesware (2008).
4. 'Light induced toxicity of merocyanine 540-silica nanoparticle complex.'
K. Das, A. Uppal, **B. Jain**, B. Bose and P. K. Gupta.
ICONSAT-2008, held at Chennai (2008).
5. 'Photophysical studies on 8-anilino-1-naphthalene sulfonic acid (ANS) bound to silica nanoparticles'.
B. Jain, A. Uppal, P. K. Gupta and K. Das.
Trombay symposium on Radiation and Photochemistry, held at Pune (2008).

List of Figures

Figure 1.1 <i>Plasmon resonance in a metallic NP excited by a light wave.</i>	26
Figure 1.2 <i>Jablonski diagram illustrating electronic excitation processes</i>	33
Figure 2.1 <i>The schematic diagram of combined microemulsion/sol-gel process for producing SiNPs.</i>	41
Figure 2.2 <i>TEM pictures of SiNPs and their typical electron diffraction pattern</i>	45
Figure 2.3 <i>Size distribution of SiNPs showing mean size ~30 nm</i>	45
Figure 2.4 <i>TEM Pictures of gold nanorods and their SAED</i>	46
Figure 2.5 <i>Size distribution of AuNRs showing rods with aspect ratios</i>	46
Figure 2.6 <i>The mean size and distribution of SiNP-VA as measured by DLS.</i>	47
Figure 2.7 <i>Optical heterodyne used for zeta potential measurement.</i>	49
Figure 2.8 <i>FTIR spectra of different components of ORMOSIL NP.</i>	52
Figure 2.9 <i>FTIR spectra of gold rods, coated with A)CTAB, B)PSS, C)PAH and D)PDDAC along with the respective polymers</i>	53
Figure 2.10 <i>Block diagram representing the concept of time correlated single photon counting.</i>	55
Figure 3.1 <i>Chemical structures of aniline naphthalene sulphonates used in the study</i>	60
Figure 3.2 <i>Photoisomerization of MC540 around the central double bond</i>	61
Figure 3.3 <i>pH titration curves: Variation of zeta potential of SiNP-VA and SiNP-V with pH.</i>	63
Figure 3.4 <i>Fluorescence emissio and lifetimes of ANS (a) and TNS (b) in presence of BSA, SiNP-V, SiNP-VA and water..</i>	65

Figure 3.5 <i>pH titration curves: Variation of fluorescence with pH of ANS (a) and TNS (b) in presence of SiNP-V and SiNP-VA.</i>	67
Figure 3.6 <i>Fluorescence emission and lifetimes of ANS (a) and TNS (b) in isopropanol, and isopropanol containing VTES and APTS.</i>	69
Figure 3.7 <i>Fluorescence anisotropy decay curves along with fitted curves of ANS and TNS in presence of BSA and SiNP-VA.</i>	70
Figure 3.8 <i>Absorption, emission and fluorescence decay curves of MC540 in aqueous medium and in presence of ~940 $\mu\text{g}/\text{mL}$ SiNP.</i>	72
Figure 3.9 <i>Relative integrated emission intensity and average lifetimes of MC540 in presence of varying amounts of SiNP added..</i>	73
Figure 3.10 <i>Photobleaching of MC540 in aqueous medium in the absence and in the presence of ~940 $\mu\text{g}/\text{mL}$ SiNP.</i>	74
Figure 4.1 <i>Different ionic structures of Cp_6 possible in the pH range of 3-8.</i>	79
Figure 4.2 <i>Absorption & emission spectra of Cp_6 in the presence of 940 $\mu\text{g}/\text{mL}$ SiNP at different pH.</i>	83
Figure 4.3 <i>Fluorescence titration of Cp_6 with increasing amounts of SiNP at pH 8.</i>	85
Figure 4.4 <i>Fluorescence titration of Cp_6 with increasing amounts of SiNP at pH 5</i>	86
Figure 4.5 <i>Fluorescence titration of Cp_6 with increasing amounts of SiNP at pH 3.0.</i> ...	87
Figure 4.6 <i>Autocorrelation traces and their fits of 10 μM Cp_6 in various environments.</i>	90
Figure 4.7 <i>Cellular uptake of Cp_6 as relative fluorescence intensity in intact cells and after extraction in SDS:NaOH solution for Colo-205 and Nt8e cells..</i>	91
Figure 4.8 <i>Fluorescence microphotographs of Colo-205 cells and Nt8e cells showing intracellular localization of Cp_6 and Cp_6-SiNP.</i>	92

Figure 4.9 Changes in percent cell survival following photosensitizer treatment in dark and after exposure to light for Colo-205 and Nt8e cells..	93
Figure 4.10 Photobleaching of 10 μ M Cp ₆ under irradiation at 660 \pm 20 nm	94
Figure 5.1 Chemical structure of PP18 and Cp ₆ and the conversion of PP18 to Cp ₆ , due to its hydrolysis in the presence of water.	103
Figure 5.2 Absorbance and fluorescence spectra of PP18 in acetone, buffer and serum at pH 7.4.	105
Figure 5.3 The absorption and fluorescence spectra of PP18 in SiNP-VA, SiNP-V, PLGA NP and liposome suspended in neat buffer at pH 7.4.	107
Figure 5.4 The absorption and fluorescence spectra of PP18 in SiNP-VA, SiNP-V, PLGA NP and liposome suspended in buffer at pH 7.4 in presence of 10% serum.	109
Figure 5.5 Fluorescence intensity at 670 nm, in all four NPs suspended in buffer at pH 7.4, as a function of time in the absence (a) and in the presence of 10% serum (b).	110
Figure 5.6 Normalized fluorescence intensity, at 712 nm in all four NPs suspended in buffer at pH 7.4, as a function of time, in the absence (a) and in the presence of 10% serum (b).	110
Figure 5.7 Time dependent absorption spectra of PP18 in SiNP-VA, SiNP-V, PLGA NP and liposome at pH 7.4.	113
Figure 5.8 Time dependent fluorescence spectra of PP18 in SiNP-VA, SiNP-V, PLGA NP and liposome at pH 7.4.	114
Figure 5.9 Time dependent absorption spectra of PP18 in SiNP-VA, SiNP-V, PLGA NP and liposome suspended in 10% serum at pH 7.4.	115
Figure 5.10 Time dependent fluorescence spectra of PP18 in SiNP-VA, SiNP-V, PLGA NP and liposome suspended in 10% serum at pH 7.4.	116
Figure 6.1 Chemical structures of the MB and NB and the polymer PSS	119

Figure 6.2 Normalized absorption spectra of AuNRs along with the absorption spectra of MB and NB.....	120
Figure 6.3 Changes in the absorbance spectrum of PSS coated AuNR upon addition of MB. Left: Tuned condition; right: detuned condition.	121
Figure 6.4 Changes in the absorbance spectrum of PSS coated AuNR upon addition of NB. Left: Tuned condition; right: detuned condition.....	122
Figure 6.5 Absorption spectra of MB and NB in the presence of varying amount of PSS.	123
Figure 6.6 Changes in the absorption peak positions upon increasing amount of dye. .	124
Figure 6.7 Relative changes in the fluorescence quantum yield and lifetime of the two dyes in the presence of varying amount of PSS coated AuNRs.....	125
Figure 6.8 Changes in the fluorescence lifetimes of the two dyes in the presence of various amounts of AuNRs.....	126
Figure 6.9 Relative changes in the k_r and k_{nr} of the two dyes in the presence of varying amount of PSS coated AuNRs. Left: tuned and right: detuned condition.	127
Figure 6.10 Fluorescence spectra of MB and NB in the presence of varying amount of PSS. B: No PSS; C: 0.1 nM PSS; D: 1 nM PSS; E: 10 nM PSS; F: 100 nM PSS; G: 1 μ M PSS and H: 10 μ M PSS.....	127
Figure 6.11 Fluorescence decay traces of MB and NB in the presence of varying amount of PSS.	128
Figure 7.1 Chemical structure of Cp_6 and repeating unit of the two polymers PAH and PDDAC.	135
Figure 7.2 Absorbance spectra of CTAB, PAH and PDDAC coated AuNRs at physiological pH.....	136

Figure 7.3 *The observed zeta potentials of the coated AuNRs with L-SPR ~ 660 nm and ~800 nm and their complexes with Cp₆.* 137

Figure 7.4 *Absorption and fluorescence spectra of Cp₆ in presence of different coated AuNR at physiological pH. The inset at bottom panel shows the corresponding fluorescence decay of the drug..* 138

Figure 7.5 *Radiative and nonradiative decay rates of the free Cp₆ and Cp₆ in the presence of coated AuNRs.* 139

Figure 7.6 *Percentage photobleaching of Cp₆ and its complexes with different coated AuNRs* 140

List of Tables

Table 3.1 <i>Fluorescence parameters of ANS and TNS in different environments.....</i>	66
Table 3.2 <i>Anisotropy parameters of ANS and TNS in different environments.....</i>	70
Table 3.3 <i>Absorption & fluorescence parameters for MC540 in different environments.</i>	73
Table 3.4 <i>Light induced toxicity of MC540, SiNP and MC540-SiNP complex against MCF-7 cells</i>	75
Table 4.1 <i>Absorption & emission parameters of Cp₆ at different pH in the presence and absence of SiNP</i>	84
Table 4.2 <i>Relative integrated emission intensity and average lifetimes of Cp₆ with various amount of SiNP at pH 8.0, 5.0 and 3.0</i>	89
Table 6.1 <i>Fluorescence parameters of MB and NB in the presence of various amounts of PSS coated AuNRs</i>	129
Table 7.1 <i>Size, zeta potential and SPR band position of different coated AuNRs</i>	137
Table 7.2 <i>Photophysical and photobleaching parameters of Cp₆ bound to different coated AuNRs at physiological pH.....</i>	140

CHAPTER 1

INTRODUCTION

In this chapter we first provide a brief introduction to nanoparticles and their use for biomedical applications. Organically modified silica nanoparticles and gold nanorods that have been used for the work described in the thesis are discussed in more detail. The basic excited state processes of fluorophores and how these processes (absorption and fluorescence) can get affected in the presence of nanoparticles are also discussed. This is followed by the experimental methodology and a brief outline of the thesis.

1.1 Introduction and historical background

‘Nano’, derived from Greek ‘nanos’, meaning dwarf, is a much talked about word of present times. However, it is pertinent to note that the use of nanotechnology has been pursued since centuries back. For instance: various Ayurvedic medications had been using nanoparticles (NPs) in different formulations such as in ‘bhasmas’, as smokes of some medicinal herbs, and are known in Indian sub continent since seventh century AD to treat various ailments [1, 2]. Also, over a thousand of years ago artists created beautiful glass works using colloidal gold and silver particles, for example creating red and yellow colours in the stained glass windows of medieval churches [3] etc. However, the science behind these technologies was not known. According to the literature, the vision towards nanoscience and nanotechnology was first given in a talk entitled “There’s Plenty of Room at the Bottom” by physicist Sir Richard Feynman at an American physical society

meeting at the California institute of technology, on December 29, 1959 which stimulated people for the first time to pay attention to the question of fabricating materials and devices at atomic/molecular scale [4].

The term ‘nanotechnology’ was first defined by Professor Norio Taniguchi in 1974 in a paper as ‘Nano-technology, mainly consists of the processing of, separation, consolidation and deformation of materials by one atom or by one molecule’ [5]. This needed to investigate the nanomaterials with respect to size, size distribution, shape and structure evolution and manipulate them. Although, the first transmission electron microscope (TEM) had been built in 1931, with the development of the scanning tunnelling microscope (STM), the atomic force microscope (AFM) etc. in 1980s the age of modern nanotechnology began. In 1981 K. Eric Drexler developed and popularized the concept of nanotechnology and founded the field of molecular nanotechnology [6]. His book ‘Engines of Creation: The Coming Era of Nanotechnology’ is considered to be the first book on the topic of nanotechnology. The observations made by him set a benchmark in the relationship between biology and nanotechnology which visualizes several cellular organelles working at nanoscales as devices and machines. He regarded cell biology as source of inspiration to synthesize model nanodevices with artificial materials for nanomedicine [7]. In the early 1980s the birth of cluster science led to the discovery of fullerenes (in 1986) and carbon nanotubes a few years later. Contemporary to this, the synthesis and properties of semiconductor nanocrystals and metal oxide nanoparticles were studied. During the past three decades an exponential growth of activities have been witnessed worldwide in developing nanoparticles with various materials, following top-down or bottom-up approaches, in order to understand the new science as well as hope for their potential applications in multidisciplinary areas due to their especial properties.

1.2 Properties of nanoparticles

NPs, due to their small size, get especial properties which are very different from bulk. Reduction in size causes modification of characteristics of the materials along with the emergence of phenomenon such as quantum size confinement in semiconductors, localized surface plasmon resonance in metals, superparamagnetism in magnetic materials, etc. Large surface to volume ratio, due to nm size, leads to prominence of interfacial effects: increased reactivity, catalytic properties, lubricant properties, surface hardness of the coated surfaces, sensitivity to environment, etc. Surface charge properties and small size also lead to stable particle suspensions. Therefore, by controlling the size, shape, composition and surface properties, NPs with enhanced and novel, physical, chemical and biological properties can be obtained. Presently, NPs are being synthesized using various types of organic, inorganic, polymeric materials as well as their combinations, which are finding applications in various areas of science and technology including biomedical field.

1.3 Biomedical Applications

Nanotechnology has shown a considerable promise to generate, manipulate and deploy nanoparticles so as to provide new possibilities for advanced bio-analytical tools and both ex-vivo and in-vivo applications [8, 9, 10]. Gold nanoparticle based immunoassay for pregnancy test is the well known ex-vivo diagnostic application which is being routinely used and kits are commercially available. Because of their small size, NPs can reach even the micro capillaries easily through blood and can therefore be useful for in-vivo diagnostic as well as drug delivery applications [11]. Also, these can be designed so as to solubilise certain dyes/drugs, which are of limited use due to their poor solubility in aqueous medium, and to minimize their high toxicity to the vital organs (such as liver, heart, kidney), in vivo degradation and short circulation times by coating and functionalizing them [12].

For in-vivo application it is important to understand the response of a body to NPs, which depends on various factors including their size. For example, small NPs get easily cleared through renal filtration, whereas NPs of size larger than 20 nm can avoid it which prolongs their circulation time [13]. The circulation time can be further increased by making their surface hydrophilic or coating them with molecules such as polyethylene glycol (PEG) in order to avoid detection by immune system(i.e., reticuloendothelial system, or RES). The process of enhanced permeability and retention (EPR) effect, due to the leaky tumour blood vasculature and poor lymphatic drainage, leads to their retention, for example, in the tumour tissue, to a higher extent as compared to the normal tissue (passive targeting) [14]. In addition, these can be functionalized easily with ligands against tumour markers or antibody against antigen for site specific targeting, where these markers are over expressed (active targeting). This can avoid the side effects of the drugs, which are carried by these NPs, making their use more effective, thereby minimizing the quantity used and hence the cost. A variety of nanoparticles such as : gold, silica, quantum dots, magnetic NPs, liposome, dendrimers, polymeric NPs and many more, are being synthesized and investigated for their potential applications in biomedical imaging, diagnosis as well as therapy which includes drug delivery [13, 15].

Conventionally, biomedical research and clinical diagnostic applications based on optical imaging mostly use organic dyes as the fluorescence markers. However, these have certain drawbacks, such as, these require lasers at different excitation wavelengths, their fluorescence gets bleached under long exposure time and also there is lack of discrimination when multiple dyes are used. NP based diagnostics and imaging is being currently explored to overcome these drawbacks. For example, there is a major advancement to use fluorescent NPs such as quantum dots (QDs) for imaging. Stable, sharp and size tunable fluorescence and wide absorption band of QDs enable them as ideal fluorophores for cell imaging and diagnostics [16]. However, toxicity due to QDs is an issue, arising due to leakage of heavy atoms, which limits their use for in vivo

applications [17]. Other NPs systems, such as dye doped silica and gold NPs, are also being actively explored for imaging and diagnostics [18, 19, 20].

For drug delivery applications, a range of organic systems (e.g., micelles, liposome, polymeric NPs, dendrimers, etc.) have been investigated [21]. For example, liposome and albumin-based delivery of drugs such as doxorubicin and paclitaxel have already been approved and functionalized liposome and polymer based drug delivery system is in phase I trial [22, 23, 24]. Although, these organic systems are biocompatible and biodegradable, their limitations include poor thermal and biochemical stability, rapid elimination due to their small size (in case of micelles and dendrimers) and opsonisation (adsorption by blood protein markers on the surface of nanocarriers and their elimination by immune system). Oxide based NPs such as silica, alumina, titania etc., have been shown to be biocompatible, stable and “stealthy” (i.e., avoid detection by immune system due to their hydrophilic surface) and therefore, show a great promise in many medical and pharmaceutical applications [25, 26]. Different porous silica based nanostructures including mesoporous and organically modified silica (ORMOSIL) nanoparticles are being actively explored to encapsulate, conjugate or entrap dyes/drugs in their porous matrix and are being investigated for imaging as well as drug delivery applications [27, 28].

While silica NPs are transparent, metal NPs such as silver, gold, copper show localized surface plasmon resonance (LSPR) in the visible to NIR region [18, 29], which lead to large enhancement (5-6 orders of magnitude as compared to organic dyes) of extinction coefficients (scattering + absorption coefficients) and large surface electric field at the metal NP sharp edges [30]. LSPR strongly depends on the metal type (: silver, gold, copper etc.), size, shape and composition of the NP, dielectric constant of the environment and the nanoparticles-surface effects. Any changes at the surface, e.g. covering the surface with some material, strongly influence the resonance properties. These properties make these particles exclusive agents for applications such as sensing

(due to plasmon peak shift caused by the change in surface refractive index), surface enhanced Raman scattering (SERS) of the adsorbed molecule (due to enhanced surface electric field at NP sharp edges), imaging (due to their large scattering coefficients) as well as for photothermal therapy (using their large absorption coefficients) [18, 19]. Among metal NPs, gold NPs have been reported to be inert and non-toxic.

Due to their versatile physical and chemical properties and biocompatibility, amorphous silica and gold nanostructures are being extensively explored for biomedical diagnostic and therapeutic applications [18, 20].

1.4 Silica NP and their applications:

Silica (SiO_2) is one of the most commonly encountered oxide materials in our life. It can exist in amorphous (vitreous silica) or in crystalline form and is transparent over the whole visible region and beyond (~200-2000 nm). Fused silica, the high purity amorphous form, is a non-toxic compound and is already being used as food additive and as carrier material in pharmaceutical tablets. Various amorphous silica based nanostructures including colloidal, mesoporous and ORMOSIL are being used and explored for their promising potential as drug/dye carrier [31]. Further advantages of silica nanoparticles, as mentioned earlier, are their inherent hydrophilicity due to the presence of charged groups (silanol) at their surfaces. This decreases their clearance by the immune system, increasing their circulation time in blood and insensitivity to microbial attack as compared to the organic NPs such as liposome, polymeric NP, etc.

These nanostructures can be conveniently synthesized by sol-gel methods by employing a variety of commercially available silica precursors. The physical characteristics including the density, pore size and structure of the silica matrix can be tailored by controlling the sol-gel reaction kinetics [32]. Two methods: Stober and micro-emulsion are typically followed for sol-gel based silica NP synthesis [33]. Stober method is based on hydrolysis and subsequent polymerization condensation of the silica

precursors such as tetraethyl etoxysilane, in the presence of ammonium hydroxide as catalyst at ambient temperature, to produce electrostatically stabilized NPs in which dye/drug molecules can be either encapsulated or covalently attached [34]. Although, this method can generate NPs of tens to hundreds of nm in size, the particle size may not be uniform and also modifications of the particle surface are not easy.

Using modified Stober's method i.e., microemulsion based hydrolysis-condensation method, silica nanoparticles (SiNPs) with controllable size and pore size have been prepared [32]. This method enables the production of nanoparticles with relatively more homogeneous size and drug/dye distribution which is important for using them in biological systems. For example, photostable and targetable SiNP were developed by controlled hydrolysis of tetraethyl orthosilicate (TEOS) using microemulsion method. These dye doped SiNPs showed good photostability with respect to bare dye or dye doped in latex based fluorescent particles and were effectively used for imaging leukaemia cells [35]. Mesoporous silica NPs (MSN) have been prepared with different tetra alkoxy ortho silicates as silica precursors to give NPs with variable and controllable pore size (~ 2-30 nm) using surfactant such as cetyltrimethylammonium bromide (CTAB) and other polymers under controlled reaction conditions, such as pH, temperature etc. These have been used to encapsulate drugs/dyes/macro molecules such as enzymes, genetic materials, etc, depending on the pore size and morphology and showed controlled release of the encapsulated molecules (such as cancer drugs) [36]. For example, in a study hollow MSN carrying fluorescein isothiocyanate (FITC, which served as a model drug) were shown to release the drug in a controlled fashion [37]. In this study, FITC encapsulated in silica nanocapsules was shown to be released over the period of a week, when soaked in an inorganic medium whereas a burst release within few hours was observed when these NPs were soaked in an organic solution indicating controlled release. Similarly, another study showed the release of anticancer drug, doxorubicin, over a period of 20 days in a constant rate [31]. Furthermore, MSN were able to enhance the

delivery of the hydrophobic anticancer drug paclitaxel to pancreatic cancer cells and allowed a targeted delivery of a chemotherapeutic agent methotrexate (MTX). In this study, while free MTX caused apoptosis in cancer as well as in healthy cells, MTX bound to MSN, in contrast, induced cell death only in cancer cells but not in normal tissue [38, 39]. These studies show the promise MSN offer as carriers, as well as for controlled drug delivery for in vivo applications, just like polymeric NP with the advantage that these do not get degraded with the external environment and are biocompatible. In addition, a variety of organically modified silica precursors available in market, provide an opportunity to make silica NPs with desired functional groups such as thiol/hydroxyl/carboxyl/amino, which can be further attached them with targeting molecules. These NPs do not show swelling or porosity changes with alteration in pH or environment which may be very important with regard to the path of delivery, for example oral application [40, 41]. These have also shown enhanced blood stability along with sustained release of anti-tumor agents and therefore, show good potential for cancer treatment [42, 43]. ORMOSIL nanoparticles, prepared using organically modified silica precursors, show amphiphilic characteristics. While these have hydrophobic porous core, they also show rich surfaces chemistry. Therefore, these particles provide an ideal platform for fabrication of multimodal imaging probes and at the same time can be used for drug encapsulation/conjugation for delivery, gene therapy or photodynamic therapy [20].

1.4.1 Organically modified silica (ORMOSIL) nanoparticles

ORMOSIL NPs are the silica NPs prepared using organically modified silica precursors, having both organic and inorganic properties (hybrid type), as starting materials. In these, trifunctional alkoxy silanes, $R'Si(OR)_3$ are the most common precursors to introduce organic groups, where the organic moiety (R') is attached through a stable Si-C bond. A variety of such silanes are commercially available. The advantage of these NPs is that

their surface could be further modified for their biocompatibility and tragetability and the NPs may slowly fragment through biochemical decomposition of the Si-C bond, which could help the removal of these particles from the body [44]. The presence of organic group also imparts flexibility, to some degree, to the otherwise rigid silica matrix, which is expected to enhance the stability of these particles in the aqueous systems against settling down [45].

Various trifunctional alkoxy silanes precursors with different organic moieties have been used to prepare a variety ORMOSIL NPs by different research groups for their studies. For example, ORMOSIL NPs using n-octyl triethoxy silane as silica precursor were prepared following both micellar and reverse micellar approach to generate spherical, nearly monodisperse NPs with diameters below 100 nm. These NPs were used to study and compare leaching of hydrophobic or hydrophilic molecules (entrapped in their hydrophobic or hydrophilic regions). In comparison to micelles, prepared using Triton X-100, the leach was found to be extremely slow indicating controlled release [44].

ORMOSIL NPs using organically modified siloxanes, vinyltriethoxysilane (VTES) and aminopropyltriethoxysilane (APTS) were prepared in the micellar core of surfactant Aerosol OT to result in amphiphilic NPs [45]. These NPs had porous hydrophobic core whereas their surface had the negatively charged silanol groups as well as the positively charged aminopropyl groups. Folic acid functionalized ORMOSIL NP, doped with hydrophobic two photon fluorescence dye, was used to target folate receptor over expressing Hela cells. ORMOSIL NPs were also used as gene carriers [46]. Kneuer et al showed that plasmids bound to amine-modified silica nanoparticles were completely protected from enzymatic digestion in human epithelial cancer cells [43]. Furthermore, Paras N Prasad's group at the university at Buffalo showed that ORMOSIL could be effectively used to introduce genes into neuronal cells in vivo. The same group along with other groups showed the properties of silica nanoparticles as oral drug carrier [47, 48].

ORMOSIL NP were conjugated with the well-known positron emission tomographic (PET) imaging probe Iodine-124 and NIR fluorophore DY776 in a study by Rajiva Kumar et al. These NPs could allow bioimaging independent of tissue-depth, as well as accurate quantification of accumulation of nanoparticles in various major organs *in vivo*. The biodistribution of these NPs by NIR optical and radiolabelling studies suggested accumulation of the NPs in the major RES organs in mice. The clearance studies of the injected nanoparticles indicated that almost 100% of the nanoparticles were effectively cleared out of the animal via the hepatobiliary excretion, without any sign of organ toxicity. These studies showed the use and safety of these ORMOSIL nanoparticles for diagnostic and therapeutic applications. Their results also demonstrated the use of these ORMOSIL nanoparticles as promising carriers for safe *in vivo* applications [28].

Recently ORMOSIL doped with dye IR-820 were used for imaging of mice brain by J. Qain et al. These NP were used to target the subcutaneously xenografted tumour of mouse for long time observations. They also used ORMOSIL NP encapsulated with photophrin IX, a PDT drug, for two photon excited cytotoxicity towards tumour cells [49, 50]. Interestingly, ORMOSIL NPs were used as carrier of hydrophobic photosensitizer such 2-divinyl-2-(1-hexyloxyethyl) pyropheophorbide entrapped in their core [51]. The idea was that although these particles do not release the entrapped drugs, their porous matrix is permeable to the molecular as well as singlet oxygen which is required to achieve the photodynamic therapeutic action (Photodynamic therapy (PDT) is a process where the photosensitizer preferentially accumulates in the tumour tissue and when excited with appropriate light, generates reactive oxygen species which are cytotoxic). Significant damage to tumour cells impregnated with these NPs upon irradiation with light of wavelength 650 nm was shown. All these results show that ORMOSIL NPs are versatile carriers of dyes/drugs for imaging as well as therapeutic applications.

1.5 Metal NPs

Noble metal nanoparticles show localized surface plasmon (LSP). These are charge density oscillations (due to the presence of conduction band electrons) confined to metal NPs and nanostructures. Excitation of LSP in the presence of the electromagnetic field at frequency where resonance occurs, leads to coherent charge density oscillations which manifest into strong light scattering, intense absorption bands and enhancement of local electric fields. Particularly in metals such as silver and gold, the 'd' electrons are free to travel through the material. As the NP size is much smaller than the wavelength of light, it can set up standing resonance condition resulting in displacement of this sea of conduction band electrons with respect to the positively charged ions that form the metallic lattice as shown in Fig.1.1.

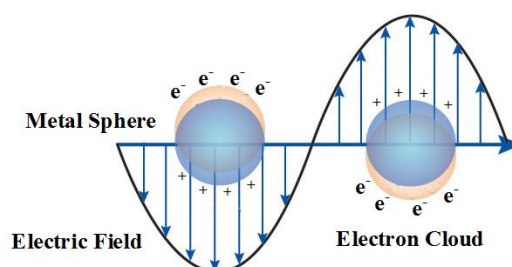


Figure 1.1 Plasmon resonance in a metallic NP excited by a light wave. Recreated from ref.52

The resulting electric dipole on the particle produces a restoring force, which determines the finite eigen frequency of the surface polarization. Amplitude of oscillation reaches maximum i.e., resonance takes place when this frequency matches with the applied field frequency, and the condition is called localized surface plasmon resonance. The resonance condition is determined from absorption and scattering spectroscopy. The position, the shape and the amplitude of the surface plasmon band strongly depends on factors: dielectric constant of the NP and its surrounding medium, on their size and size distribution, shape and the composition. Also, the electronic interaction between the

stabilizing ligands and the NP which alters the electron density of the NP alters the position of the SPR [53]. Hence, NP can be considered as a harmonic oscillator, which is driven by a light wave and damped by some losses such as ohmic loss (which leads to production of heat) and radiative (scattering) loss. For small spherical particles the scattering, extinction and absorption cross-sections are given in Rayleigh limit as follows [54]:

$$C_{scat} = \frac{3}{2\Pi} \left[\frac{\omega}{c} \right]^4 \varepsilon_{diel}^2 V^2 \frac{(\varepsilon_r - \varepsilon_{diel})^2 + (\varepsilon_i)^2}{(\varepsilon_r + 2\varepsilon_{diel})^2 + (\varepsilon_i)^2} \quad \dots\dots\dots 1)$$

$$C_{ext} = 9 \left[\frac{\omega}{c} \right] (\varepsilon_{diel})^{\frac{3}{2}} V \frac{(\varepsilon_i)}{(\varepsilon_r + 2\varepsilon_{diel})^2 + (\varepsilon_i)^2} \quad \dots\dots\dots 2)$$

$$C_{ext} = C_{abs} + C_{scatt} \quad \dots\dots\dots 3)$$

Here ε_r and ε_i are the real and imaginary parts of the dielectric constant of the metal and ε_{diel} is the dielectric constant of the environment around, ω and c are the light frequency and velocity and V is the volume of the NP. C_{ext} is the summation of the absorption and scattering cross-section, related to extinction coefficient as [55]:

$$\epsilon \text{ (M}^{-1}\text{cm}^{-1}\text{)} = 10^{-3} N_0 C_{ext} \text{ (cm}^2\text{)} / 2.303.$$

In equation 1 and 2, denominator is minimum, i.e., resonance occurs, for $\varepsilon_r + 2\varepsilon_{diel} = 0$. In case of noble metals this happens in the visible region, as real part of dielectric constant is negative and the imaginary part is ~ 0 . SPR position is determined by this real part of the dielectric constant of the metal while the imaginary part determines the bandwidth. These equations also show that while the scattering cross-section depends quadratically on the volume, the extinction cross-section depends only linearly. Therefore, for very small particles (~ 10 nm) the extinction is dominated by absorption and it is very hard to see any

scattered light whereas as the size increases (~80 nm) scattering starts dominating over absorption. This suggests that smaller NPs can be used for absorption based applications such as biosensing, photothermal therapy of cancer, etc. whereas larger size metal NPs can be utilized for biological imaging and labeling [56]. Different metal nanospheres, for example, Ag (diameter=20 nm), Au (12 nm), Cu (12 nm) exhibit plasmon absorption bands with maxima at 410, 520, and 564 nm respectively while platinum, palladium have weak and broad band in the UV region [57].

1.5.1 Gold NPs

Gold is considered as the most inert among metals. Nanoparticles of gold show properties which make them suitable for use in numerous biological applications. For example spherical gold NPs have been used *in vivo*, since 1950s, as adjuvant in radiotherapies [58]. Although gold NP of size ~ 2 nm show high catalytic activity and are reported to be toxic [59], larger size gold NP are reported to be biocompatible [53]. These show strong optical extinction peak which can be varied by controlling particle morphology and their surface chemistry allow for easy attachment of the functional groups required for targeting. The current interest in nanotechnology has led to the development of various shapes of gold NPs which include spheres, core-shell, cubes, stars, cages, rods, etc., for biological applications such as imaging, sensing/diagnostics (which are based on change in refractive index, aggregation of NPs, SERS, scattering, two photon luminescence, etc.), tracking, drug delivery, photothermal therapy, etc. [60].

For achieving efficient contrast in imaging/diagnostic and for photo thermal therapeutic applications, it is important to choose nanoparticles of right size and shape. Recently El Sayeed's group [61], calculated and compared absorption and scattering efficiencies and optical resonance wavelengths of gold nanospheres, silica-gold core-shell NPs, and gold nanorods of different sizes using Mie theory and discrete dipole approximation. A systematic quantitative study of the various trends presented by them

showed that by increasing the size of gold nanospheres from 20 to 80 nm, the magnitude of extinction as well as the relative contribution of scattering to the extinction rapidly increases. While nanosphere of size 40 nm showed an absorption cross-section 5 orders higher than conventional absorbing dyes, the magnitude of light scattering by 80 nm gold nanospheres is 5 orders higher than the light emission from strongly fluorescing dyes per particle. The variation in the plasmon peak of nanospheres was from 520 to 550 nm. This is far from the therapeutic window (~650-900 nm), which limits their use for in vivo applications (due to large tissue scattering). In case of gold nanoshells, the optical cross-sections were shown to be comparable to and even higher than the nanospheres. By increasing the ratio of the core-to shell radius, the optical resonance wavelength could be increased upto the near-infrared region, which makes them useful for in vivo applications such as photoacoustic imaging and photothermal therapy [62, 63]. However, controlling the core to shell thickness ratio is practically difficult.

Gold nanorods (AuNR) can be synthesized with aspect ratios (ratio of length to width), which can be conveniently tuned to shift their extinction peak to near infra-red (NIR) spectral region, therapeutic window, allowing deeper penetration of photons in biological tissue. Also, in NIR frequency, AuNR have an order of magnitude higher absorption and scattering coefficients than the nanoshells and nanospheres. Rods also show narrower linewidths due to reduced radiative damping effects leading to higher photothermal conversion efficiency [64]. Therefore, these are being actively investigated for contrast based imaging and PTT [65].

1.5.2 Gold nanorods and Photothermal processes

As the shape of gold NP changes from sphere to rod, the SPR splits into two bands [66]. Oscillation of electrons along the longer axis generates a stronger band in the NIR region (referred to as longitudinal surface plasmon, L-SP), whereas a weak band in the visible ~520 nm along the shorter axis, is similar to nanospheres (referred to as transverse surface

plasmon, T-SP). This transverse band position is almost insensitive to the changes in the rod size whereas the longitudinal band largely shifts from visible to NIR region by increasing the aspect ratio.

While the radiative i.e., enhanced light scattering properties of gold NPs are used for imaging, the absorbed light can be converted into non-radiative processes [67]. Theoretical studies have shown that this is due to the fast phase loss of the coherently excited electrons on femtosecond time scales due to electron-electron collisions leading hot electrons with temperatures $\sim 1000\text{K}$ [55]. These electrons pass the energy to the phonons by electron-phonon interactions on the order of 0.5-1ps, which results in the rise in temp of the lattice \sim few tens of degrees. Subsequently, three processes can occur a) the lattice cools down passing heat to the surrounding medium by phonon-phonon relaxation within $\sim 100\text{ps}$. This can be utilized for sufficient heating of the adsorbed/attached cells using light with wavelength overlapping to the SPR of the NP, b) The lattice heat can lead to particle melting, c) or particle fragmentation depending upon the rate of heating and cooling [68,69]. For applications such as cancer cure, process 'a' has to be dominated which can be realized using continuous wave lasers, whereas the other two processes can be used for drug delivery applications [70]. Among the other structures, gold nanorods convert the electromagnetic radiation efficiently into heat and hence considered to be promising tools in applications such as in vivo photoacoustic imaging [71] tissue soldering [72] drug delivery [73] and photothermal cancer therapy [74].

Several methods had been adopted for the preparation of gold nanorods. In early 1990's rods were prepared by electrochemical reduction of gold into nanoporous aluminium oxide membranes. Although this gave relatively monodisperse structures, the yield was low and the diameter was $>100\text{ nm}$ which showed the optical response dominated by multipolar plasmon resonance modes. Later electrochemical oxidation of gold electrode in the presence of cationic surfactant cetyl trimethylammonium bromide

(CTAB) under ultrasonication was demonstrated to synthesize rods with ~10 nm diameter. These rods exhibited transverse and longitudinal plasmon modes and for the first time verified the gold rod optical theory, proposed by Gans for the scattering and absorption. C. J. Murphy and M. A. El-Sayed groups later demonstrated a colloidal growth method to produce monodisperse gold nanorods with high yield based on seeded growth [18]. In this method ~1.5 nm diameter single crystal seed particles are first produced by reduction of chloroauric acid by borohydride in the presence of CTAB. Aliquot of this seed is then put in the growth medium, which contains Au (I) growth solution, prepared from the mild reduction of chloroauric acid by ascorbate, CTAB and AgNO₃. Using this method, gold nanorods of diameter 10-20 nm and length up to 300 nm had been prepared with relatively high yield. By controlling the growth parameters such as ratio of seed to growth medium, concentration of silver ions, etc. the nanorods of desired and precisely controlled aspect ratio can be obtained. [75,76, 77, 78].

This last method is the most common method of preparation of gold nanorods (AuNR) where the gold salt is chemically reduced in the rod-shaped micellar template formed at high concentration of CTAB [18, 76]. CTAB is the structure-directing agent that is used to control gold nanorod shape, and it appears to form a tightly bound cationic bilayer on gold nanoparticles, with the cationic trimethylammonium headgroup exposed to the solvent [79]. However, the high concentration of CTAB employed in AuNR synthesis has raised concerns regarding their toxicity [80]. Efforts have been made to remove the extra CTAB and overcoat the CTAB coated rods with other materials that lead to better biocompatibility and stability of the AuNRs [79]. Different biocompatible polymers have been used for layer by layer coating the Rods [81]. As CTAB coated rods are positively charged these can be easily coated with negatively charged polymers such as polystyrene sulphonate (PSS) which can be further coated with positively charged biocompatible polymers such as poly ally amine hydrochloride (PAH), poly diallyl dimethyl ammonium chloride (PDDAC) etc.

For both diagnostic and therapeutic applications either the NPs themselves can be used or these can be conjugated with dyes/drugs to cause these applications. The conjugation of these dyes/drug molecules with the NPs may be covalent, hydrophobic or electrostatic. However, due to conjugation their properties may change. How the photophysics of these molecules change due to conjugation and whether it affects their biological activity is interesting to study. Dye NPs interaction can be conveniently studied by optical absorption and fluorescence spectroscopy. For this it is important to understand the excited state processes involved upon the excitation of fluorophores.

1.6 Excited state processes

In the presence of electromagnetic field, a dye may absorb depending on its dipole strength. During this excitation, three main processes can be involved: 1) absorption of light energy ($\sim 10^{-15}$ s, associated with an electron transfer to an excited state), 2) this is followed by radiationless decay, either within or from the higher vibrational levels, of the excited states. In biological systems, this vibrational relaxation occurs on a picoseconds time scale and only those chemical processes, with rate constants higher than 10^{12}s^{-1} , compete with vibrational relaxation. Subsequent to excitation, vibrational relaxation is usually complete before electronic relaxation, and 3) fluorescence, i.e., emission with frequency smaller than the excitation frequency. The difference between the wavelength required for excitation and the wavelength of the emitted light is known as the Stokes' shift which corresponds to the radiationless energy loss within the excited state. A representative method for illustrating these electronic processes is the Jablonski diagram.

As shown in Fig.1.2 a molecule initially is in the singlet ground state S_0 . Upon absorption of radiation it goes to excited singlet states S_n , wherefrom through, vibronic relaxation of excited singlet S_1 states it reaches to first excited singlet ground state. From here the molecule can radiatively decay by two basic pathways. Decay from S_1 to S_0 by emission of residual energy as photons may occur called fluorescence. This process

occurs in the states of the same multiplicity and, in terms of quantum mechanics, this is spin allowed process.

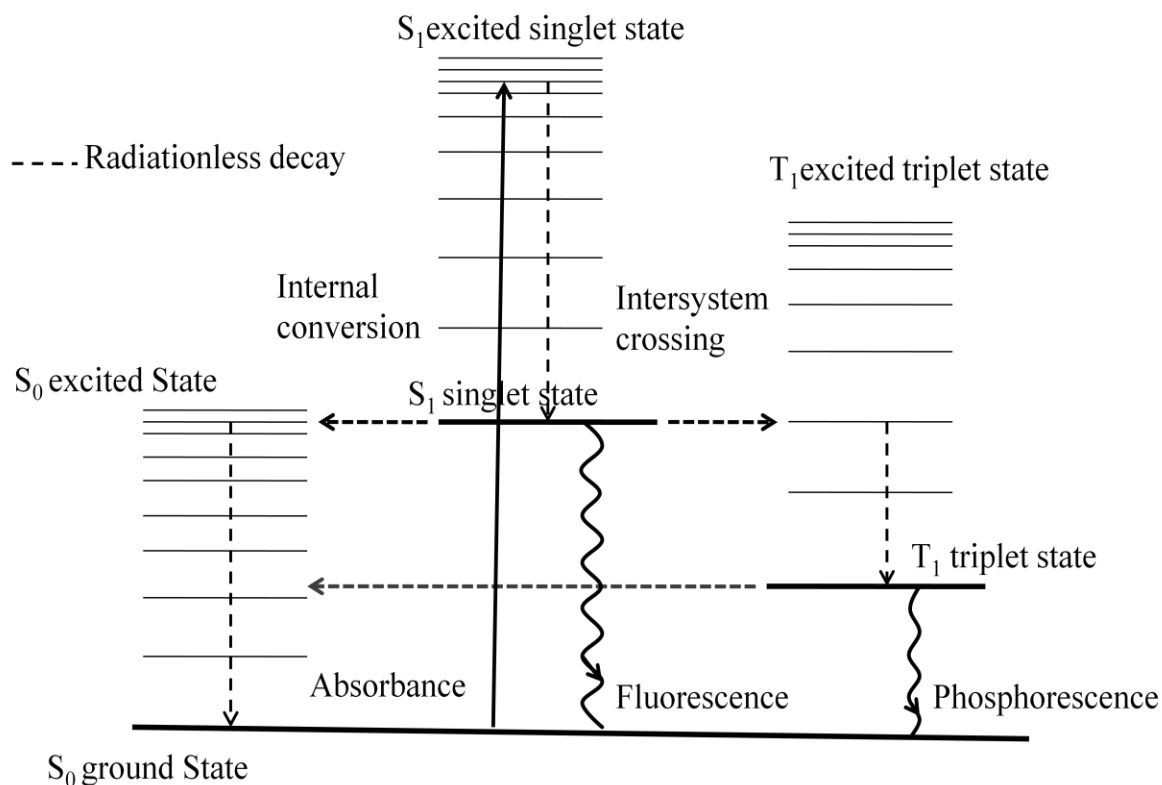


Figure 1.2 Jablonski diagram illustrating electronic excitation processes

The intensity of fluorescence from the excited molecule, although depends on the magnitude of radiative decay rate (k_r), is strongly dependent upon the internal competing processes. The other radiative decay path way, phosphorescence, involves intersystem crossing from S_1 to a triplet state T_1 . This is due to spin-orbit coupling leading to an efficient crossing between states of different multiplicity. As it is a spin forbidden process it has much longer lifetimes as compared to fluorescence. The other nonradiative processes competing with fluorescence include internal conversion to the ground state, charge transfer, energy transfer, the photochemical reactions, photoisomerism, etc. For symmetry allowed transition, radiative decay rate, $k_r \sim 10^9 \text{ s}^{-1}$. In the absence of any other depopulation process, the radiative decay time is $1/k_r \sim 10^{-9} \text{ s}$. This is termed as natural or

mean radiative lifetime, τ_R . In practice, because of the other non-radiative competing processes, as mentioned above, the measured decay time (for complex polyatomic molecules) is less than the mean radiative lifetime. Therefore, the quantum yield of fluorescence is given as follows:

$$\text{Quantum yield, } Q = \frac{k_r}{k_r + k_{nr}} \text{ -----4}$$

$$\text{Life time, } \tau = \frac{1}{k_r + k_{nr}} \text{ -----5}$$

Here k_{nr} is the non-radiative rate.

When light is incident on fluorophores attached to the metallic surface, the electric field associated with the fluorophores may get affected because of the induced electric field caused by the generation of surface plasmon. This effect has the ability to either increase or decrease the effective electric field on the fluorophores [82]. In the presence of metallic NPs, the fluorophores may undergo one of three processes: 1.) energy transfer to the metal that results in fluorescence quenching, 2.) an increase in the intrinsic radiative decay rate of the fluorophores, or 3.) amplification of the incident electric field by the metal, thereby causing an increase in the intensity of the emission [82].

The excited state properties of many organic dyes used for biomedical applications are sensitive to environment properties such as polarity, viscosity, pH, etc. For example 8-anilino-1-naphthalenesulfonate (ANS), 6-p-toluidino-2-naphthalenesulphonate (TNS) are polarity sensitive dyes. In polar medium their excited state decays by charge transfer from donor (anilino and toluidino) groups to the acceptor (sulphonate) group followed by a twist around the donor. This is the dominant non-radiative decay process which leads to significantly low emission quantum yield in polar medium such as water [83]. However, in hydrophobic environment the probability of this process may be significantly suppressed, for example in proteins, where these dyes can

get entrapped in their hydrophobic pockets, leading to an order of magnitude increase in the quantum yield [84]. Similarly some dyes undergo excited state photoisomerism which may also be polarity/viscosity sensitive. For example merocyanine 540, is a well known membrane binding dye (It is also used for PDT) [85]. In polar medium such as water, it exists as mixture of monomer and dimer [86]. While the monomer is weakly fluorescent, the dimer is non-fluorescent [87]. This weak fluorescence is due to the photoisomerization process accounting for the main non-radiative decay pathway for MC540 in the excited state [88]. Binding to membranes, such as liposome, has shown significant enhancement in its emission quantum yield [89]. Several cyanine and fluorescein dyes have been used as pH sensitive dyes, which show emission intensity switching or wavelength shift depending on the ionic strength of the environment [90]. Chlorophyll-a derivative, such as Chlorin p_6 (an amphiphilic photosensitizer) shows pH dependent aggregation [91]. It has three negatively charged carboxylic acid groups at physiological pH. With the increase in the protonation of the environment, it shows a significant decrease in its absorption and fluorescence properties, due to the neutralization of the carboxylic acid groups.

Interaction of dyes with NPs may be either due to electrostatic interaction or hydrophobic interaction or both if the NP itself is amphiphilic in nature. Electrostatic interaction may change the electronic distribution around the donor and acceptor groups of the dye or in the case of hydrophobic interaction, the dye may preferentially get entrapped in the hydrophobic region of the NP thereby restricting its motion in the excited state. Amphiphilic dye may interact in both ways. This interaction may change the excited state properties of these dyes. When dye molecules interact with NPs, depending upon the optical, physical and chemical properties of the nanoparticle, the absorption and fluorescence properties of the conjugated dye may change, which may also affect their efficacy. In case of metal NPs, the interaction between surface plasmon and molecules adsorbed on the surface may greatly affect the excited state properties of molecules and

give rise to interesting phenomenon such as plasmon enhanced fluorescence, fluorescence quenching, surface-enhanced Raman scattering, energy or electron transfer, enhancement of nonlinear optical signals and spin relaxation [92, 93]. The interaction may lead to strong or weak coupling between the wavefunction of the molecules and the plasmon modes which may or may not get perturbed. In addition to fundamental interest, these interactions have potential applications for development of optical devices with functions such as switching, energy transfer and sensing [94]. Also, the adsorption of photosensitizers to plasmonic NPs may enhance the phototoxicity due to a combination of photothermal effect due to plasmonic absorption as well as photodynamic effect due to molecular absorption [95].

1.7 Experimental plan

As discussed in section 1.4, the published reports on ORMOSIL NPs show them as versatile carriers for hydrophobic dyes/photosensitizers (in the hydrophobic core of NP) from both diagnostic as well as therapeutic point of view. However, ORMOSIL NPs prepared with VTES and APTS silica precursors, have amino propyl groups on their surface. As the pK_a of amino group is ~ 9.2 , these amino groups are positively charged at physiological pH and therefore, there is a possibility of electrostatic binding of negatively charged molecules with these amine modified ORMOSIL NP at this pH. As part of the thesis we studied how the photophysics of molecules change when they bind with ORMOSIL NP and how this change affects their functionality.

To investigate the nature of interaction, we have chosen dyes like ANS, TNS and MC540, which are negatively charged polarity sensitive dyes. According to literature, in polar medium, the excited state of ANS and TNS decay non radiatively due to twisted intramolecular charge transfer, whereas MC540 undergo photoisomerism in its excited state, which is the major non-radiative decay channel. Due to these prominent non-radiative decay processes, their fluorescence quantum yield is very poor in aqueous

medium. It has been shown in the literature that binding with proteins, surfactants, membranes and liposome increases their quantum yield. We were therefore interested to study their interaction with ORMOSIL NPs. As MC540 is also a photodynamically active dye, we tested the effect of this dye conjugated with SiNP on the phototoxicity on cancer cell lines.

We also studied the interaction between porphyrin type photosensitizers Cp_6 and PP18 and these SiNPs. Both are interesting photosensitizers because these have significant absorption in the longer wavelength (650-900 nm) where tissue absorb and scatter weakly. Cp_6 is amphiphilic and negatively charged at physiological pH due to the presence of three carboxylic acid groups. Earlier studies have shown that Cp_6 shows pH dependent aggregation behaviour below physiological pH. Also the uptake and efficacy of Cp_6 in cancer cell lines have been shown to be pH dependent. We were therefore interested to study the pH dependent aggregation behaviour of Cp_6 in the presence of SiNP suspended in aqueous medium. The phototoxicity of Cp_6 -SiNP complex on cancer cell lines was also studied. While Cp_6 is amphiphilic, PP18 is hydrophobic and therefore needs a suitable carrier for delivery. The interest to use PP18 for PDT applications is due to its higher extinction coefficient at longer wavelength as compared to Cp_6 , which is desired for deep tissue penetration of light. However, in aqueous medium PP18 converts to Cp_6 due to the hydrolysis of its anhydride ring. We investigated the suitability of SiNPs as carriers of hydrophobic PP18 in aqueous media by monitoring its time dependent conversion to Cp_6 in SiNPs and compared with liposome and polymeric NPs.

As discussed in section 1.5, among the plasmonic NPs gold NPs are biocompatible. Among the different gold nanostructures (spheres, core shell and rods) gold nanorods show an order of magnitude higher extinction coefficient. The more interesting part in gold nanorods is that their L-SP can be easily tuned from visible to NIR by controlling their aspect ratio. We were interested to investigate the effect surface plasmon electric field on the optical (absorption and emission) properties of the dyes

attached to them. To observe the effect of L-SP we used gold nanorods whose L-SP peak position was tuned to and off the absorption maximum of two dyes, MB and NB. We also investigated the spectroscopic properties of a photosensitizer Cp_6 conjugated to gold nanorods. This was motivated by a recent paper Kuo et al., where they have suggested that a combination of photodynamic therapy (PDT) and photothermal therapy (PTT) can be more effective than either PDT or hyperthermia alone and can be easily realised by conjugating NIR absorbing photosensitizers with NIR absorbing AuNRs [95]. This made us interested to study the effect of L-SPR on the photophysical properties of Cp_6 electrostatically conjugated to gold nanorods. As discussed in section 1.5, the CTAB coated gold nanorods are positively charged. However, due to issues regarding the toxicity of CTAB [96] these rods were coated with biocompatible polymer PSS. PSS is a negatively charged polymer and Cp_6 is also negatively charged at physiological pH. For electrostatic binding between Cp_6 and the rods, these rods were again coated with positively charged biocompatible polymers PAH and PDDAC. We investigated interaction of Cp_6 with these coated AuNR of two different aspect ratios, with their L-SP tuned to and away from the Q-band absorption peak of Cp_6 . The effect of L-SP position as well as the nature of coatings on the photophysics of Cp_6 was studied.

1.8 Outline of the thesis

In chapter 2 the methodologies used for the preparation of different NPs, different techniques used for NP characterization and spectroscopic studies along with their basic principles are briefly given. In chapter 3 the photophysical studies on interaction of ANS, TNS and MC540 with ORMOSIL NPs are presented while in chapter 4 we present the spectroscopic investigations on the binding of the photosensitizer Cp_6 with amine modified silica nanoparticles in aqueous media along with the evaluation of photodynamic efficacy of Cp_6 -SiNP complex in colon and oral cancer cell lines. A spectroscopic study on conversion of PP18 to Cp_6 in the presence of liposome, silica and

polymeric nanoparticles is given in chapter 5. Spectroscopic investigations on the binding of Methylene blue and Nile blue to gold nanorods are presented in chapter 6 whereas photophysical properties of Cp_6 bound to gold nanorods are described in chapter 7. Chapter 8 gives the conclusion of the thesis and suggestions for the future research work.

CHAPTER 2

EXPERIMENTAL DETAILS

In this chapter we provide details of the methods used for preparation of different NPs (ORMOSIL NP [45, 97], gold nanorods [77, 98], polymeric NPs [99] and liposomes [100, 101]) used for the studies described in the thesis. The methods used to characterize these and to study their interaction with dyes are also detailed. Finally we describe the methodology used for determination of cellular toxicity due to dye-NP conjugates [102] and to calculate the molarity of the NPs.

For all the preparations and experiments, water from a Millipore Milli-Q system was used.

2.1 Synthesis of NPs

2.1.1 ORMOSIL NP (SiNP-V, SiNP-VA)

The ORMOSIL NPs were synthesized using microemulsion based sol-gel method, also called modified Stober's method [45]. For this the chemicals: silica precursors vinyl-triethoxysilane (VTES), 3-aminopropyl-triethoxysilane (APTS), surfactant dioctyl sodium sulfosuccinate (aerosol OT (AOT)), 1-Butanol (spectroscopic grade) were purchased from Sigma and used as received. The schematic diagram depicting combined microemulsion/sol-gel process for producing SiNPs is shown in Fig. 2.1. Two types of ORMOSIL NP, one with silica precursor vinyl-triethoxysilane (VTES) and other with both VTES and 3-aminopropyl-triethoxysilane (APTS) were synthesized.

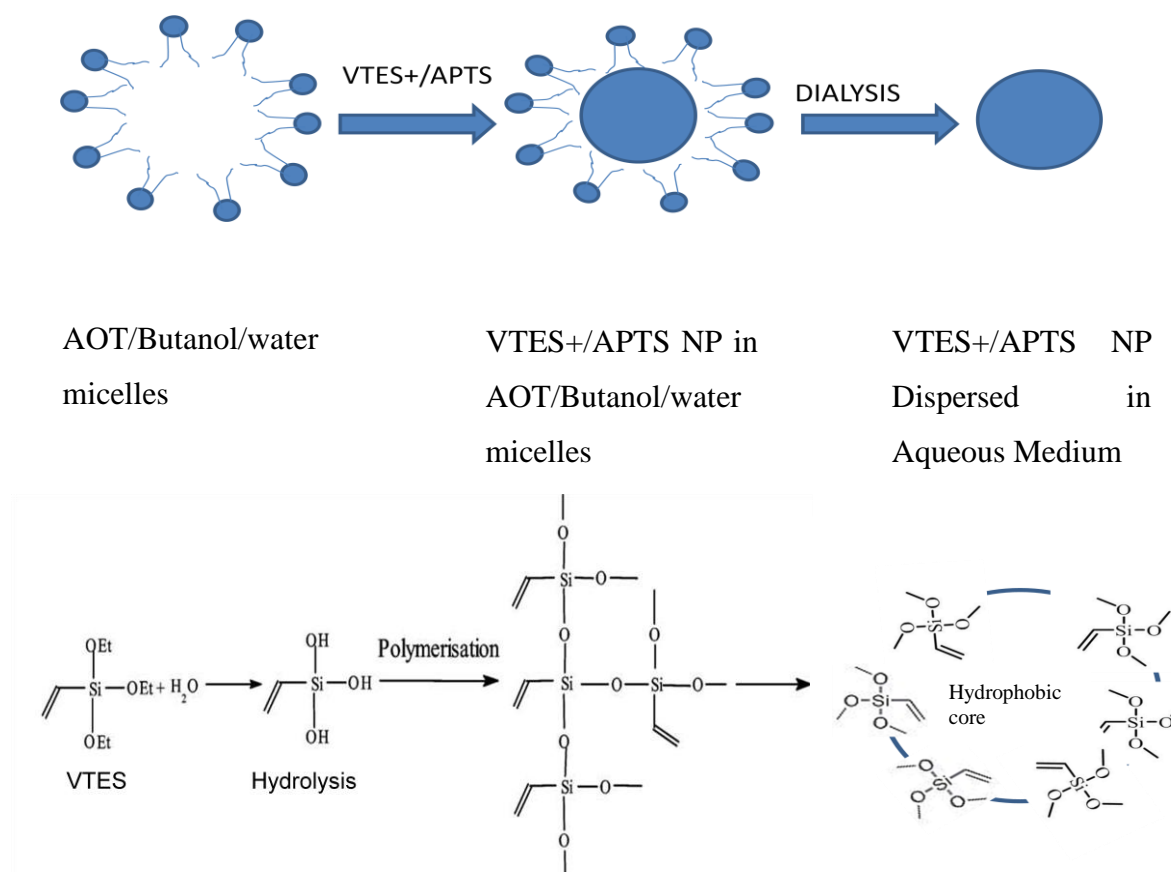


Figure 2.1 The schematic diagram of combined microemulsion/sol-gel process for producing SiNPs. Recreated from ref. [51, 97]

Amine modified SiNPs (SiNP-VA) were synthesized in the non polar core of anionic surfactant AOT (Mol. Wt. 444.56, cmc~1mM)/1-Butanol/water micellar system using VTES and APTS following the method as described in reference 45. In this method, first the micelles were prepared by dissolving 0.44g AOT and 800 μ l of 1-butanol (used as co-surfactant) in 20ml of water under vigorous magnetic stirring for ~ 1 h. VTES (200 μ l) was added to this micellar system. The resulting solution was stirred until it became visibly transparent. After ~30minutes, APTS (20 μ L) was added to the solution, which was further stirred for about 20 h. The entire reaction was carried out at room temperature. At the end of the process, a bluish white translucency, indicating the formation of nanoparticles, was observed. NPs with only VTES silica precursor (SiNP-V)

were prepared following the same procedure. However in place of APTS, 20 μ L of aqueous ammonia (30 %) was added as the reducing agent. The SiNPs were purified from AOT and butanol by dialyzing (using a membrane having a molecular cut-off 10 kDa) against neutral water for a period of ~96 hours such that the SiNP colloidal suspension did not show the standing froth due to the presence of AOT after dialysis. These SiNPs were kept at 10 degree centigrade till use and were found to be stable for more than a year.

2.1.2 Gold Nanorods

CTAB-coated AuNRs having different L-SPR were synthesized, by Dr. A.Uppal and Dr. R.Shrivastava, following the seed mediated growth procedure [77, 98]. The chemicals used : $\text{HAuCl}_4 \cdot 3\text{H}_2\text{O}$, CTAB, l-ascorbic acid, NaBH_4 , AgNO_3 , polymers polystyrene sulphonate (PSS), poly allylamine hydrochloride (PAH) and poly diallyl dimethyl ammonium chloride (PDDAC) were purchased from Sigma-Aldrich and were used as received.

First, CTAB capped seeds were prepared by chemical reduction of HAuCl_4 with sodium borohydride. For this 5 ml of 0.2 M CTAB was mixed with 5 ml of 5 mM HAuCl_4 . Then 0.6 ml of ice cold 0.01 M NaBH_4 was added while stirring for 2 minutes. The seed solution was kept at room temperature and used within 2-5 hours. For synthesis of AuNRs having L-SP around ~660 nm, the growth solution containing 10 ml of 0.2 M CTAB, 10 ml of 1 mM HAuCl_4 , 120 μ l of 0.01M AgNO_3 and 144 μ l of 0.1 M ascorbic acid was prepared. After that, 24 μ l of seed solution was added to the growth solution to initiate the growth of the AuNRs. For AuNRs having L-SP around ~800 nm the growth solution was prepared by mixing 8 ml of 2 mM HAuCl_4 , 12.6 ml water, 19 ml of 0.2 M CTAB, 160 μ l of 0.015 M AgNO_3 and 256 μ l of 0.1 M ascorbic acid. After that 175 μ l of seed solution was added to initiate the growth of the AuNRs.

Coating of AuNRs with polymers PSS, PAH and PDDAC:

As CTAB coated rods were positively charged, these were first coated with negatively charged polymer PSS and then coated with positively charged polymers PAH or PDDAC. For this AuNR solution was centrifuged at 10,000 rpm for 30 minutes and then the sediment was re-suspended in Millipore water to remove the extra CTAB. This procedure was repeated once more and then the rods were suspended in 1 mM sodium chloride solution containing 2 mg/mL PSS. The nanorod solution was stirred for 2-3 hours and then centrifuged at 12,000 rpm. The attachment of PSS onto the AuNR surface was confirmed by checking the zeta potential of the AuNRs (as described in section 2.2.3). The sediment was then re-suspended into a 3 mg/ml PDDAC or PAH solution in 1mM sodium chloride, stirred for 2-3 hours and then centrifuged twice at 12,000 rpm for 10 minutes each to remove extra polymer. Finally, the sediment was re-suspended in Millipore water until use at room temperature.

2.1.3 Polymeric ((poly(lactic-co-glycolic) acid (PLGA)) NP

Nano-PLGA formulations were prepared by nano-precipitation technique with minor modifications by Dr. A.Uppal [99]. The chemicals: PLGA (poly(lactic-co-glycolic) acid) and PVA (Poly-vinyl alcohol) and HPLC grade acetone were purchased from Sigma. For particle synthesis 90 mg of PLGA was dissolved in 10 ml of HPLC grade acetone over a period of 3 h to get a uniform PLGA solution. This solution was drop wise added to 20 ml of aqueous solution containing 1.5% of PVA over a period of 10 min on a magnetic stir plate operated at 800 rpm. Within a few minutes, precipitation of nanoparticles was observed. This suspension was stirred at room temperature for 24 h to evaporate the acetone solvent completely. Larger aggregates and free PLGA/PVA polymers were removed by centrifugation at 5,000 rpm for 10 min. Then centrifuged at 18,000 rpm for 1 h and washed the sediment with water. These NPs were stable for more than six months at 10 degree centigrade.

2.1.4 Liposomes

Phosphatidylcholine (PC) was purchased from Sigma. Smaller unilamellar liposome of size ~30 nm, were prepared by injecting a 100ul ethanolic solution of phosphatidylcholine (PC, 20mg/ml) into 1.0 ml water/buffer at the required pH following the method as described in ref. [100]. Liposomes were prepared on the same day of the experiment.

Large unilamellar PC liposomes of size ~1 μ m were prepared using the method as described in ref. [101]. In this method a stock solution, containing 15.2mg PC dissolved in 10 ml chloroform, was first prepared. To a clean and dry 50 ml round bottom flask 1ml of this stock solution and 200 μ l methanol was added. To this 7ml of distilled water/buffer was carefully added by the sides so that the two phases remain separate. Slowly the flask was attached to a rotary evaporator, at ~40 rpm under reduced pressure for ~two minutes, to evaporate the methanol (the flask was kept at temperature ~40 degree centigrade). After evaporation an opalescent fluid was obtained in the flask. To this added 3ml of distilled water/buffer. Thus ~1micrometer diameter liposomes were prepared with 0.2mM lipid. These were stable for more than a week when stored at 10 degree centigrade.

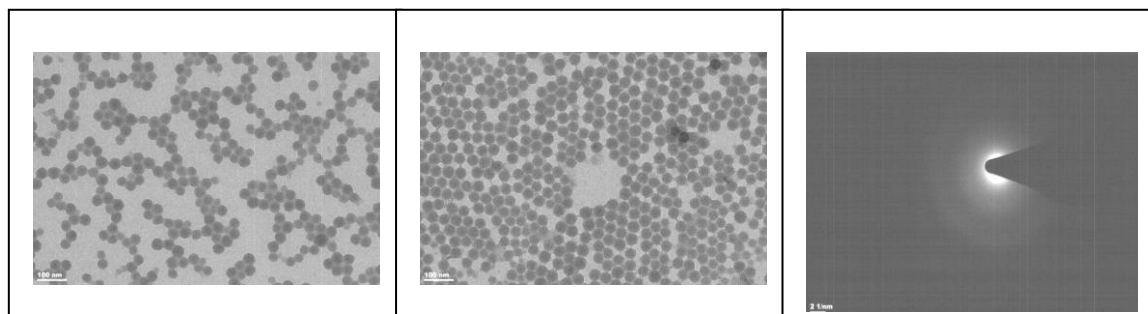
2.2 Characterization of NPs

The morphology and structural properties of NPs were monitored by TEM imaging and their hydrodynamic radii were measured by light scattering methods such as dynamic light scattering and fluorescence correlation spectroscopy. To study the interaction of NPs with dyes, NPs were characterized for their surface charge, coatings as well as the functional groups, which were carried out by measuring their zeta potential and by studying their vibrational spectra by FTIR spectroscopy. The details are given below:

2.2.1 Transmission Electron Microscopy

The TEM imaging of SiNPs and gold nanorods was done using model CM200 from Phillips, operating at 200kV with 2.5 \AA point-to-point resolution. Samples for TEM were

prepared by dipping the carbon coated copper grid in the nanoparticles solution and evaporating in the dark. This process was repeated a few times to get sufficient number of nanoparticles in the field of view. The TEM images of SiNPs and gold nanorods, of two different aspect ratios, are shown in Fig. 2.2 and Fig. 2.4 respectively.



SiNP-VA , Size~30±5 nm

SiNP-V, Size~30±2 nm

SAED

Figure 2.2 TEM pictures of SiNPs and their typical electron diffraction pattern

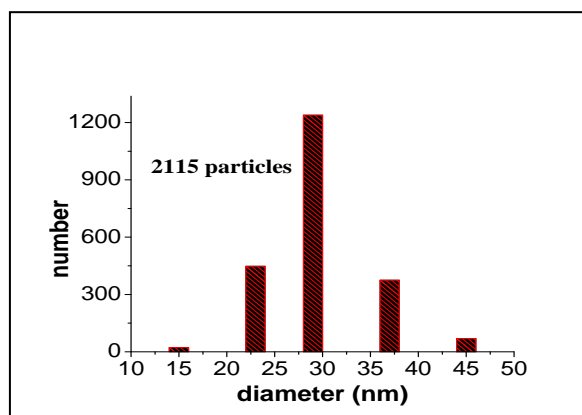
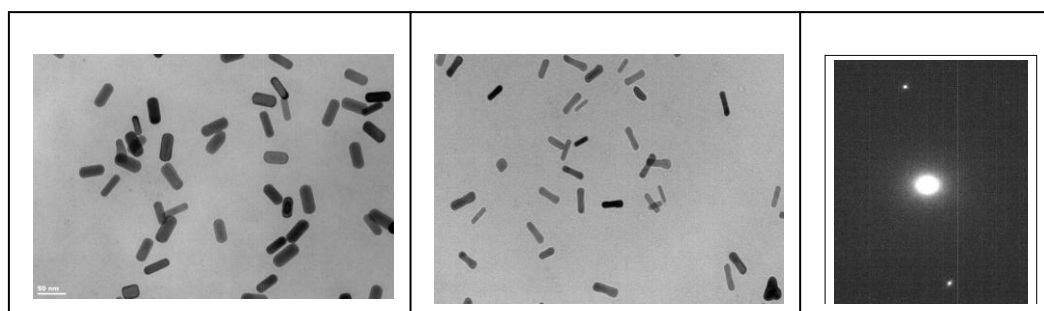


Figure 2.3 Size distribution of SiNPs showing mean size ~30 nm

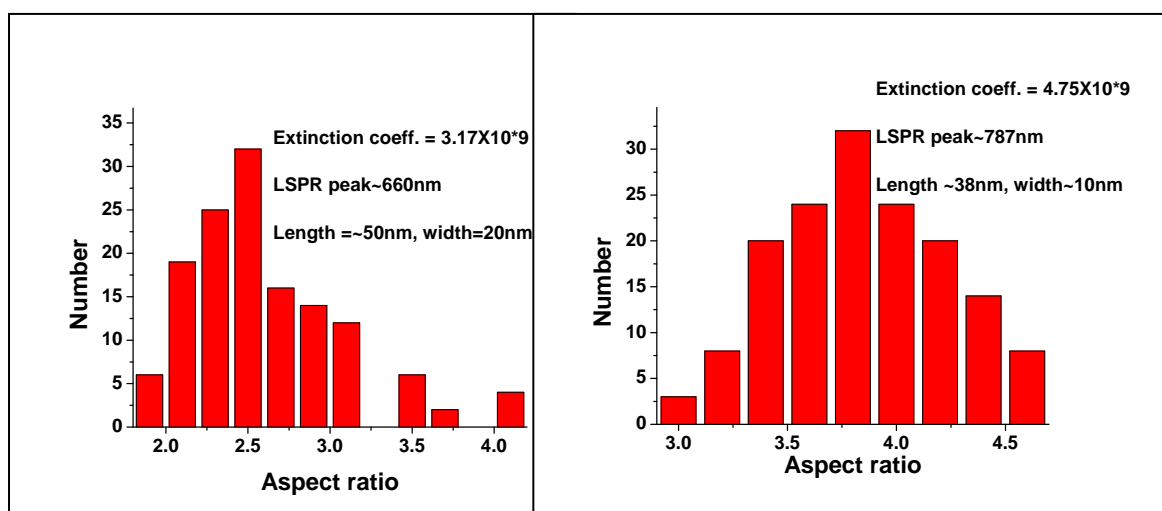
Selected area electron diffraction (SAED) pattern indicating their amorphous and crystalline nature is also shown in the figures. SAED pattern in Fig.2.2 shows a series of rings indicating the amorphous nature of SiNPs whereas a pattern of dots, in the Fig.2.4, indicate that the gold nanorods are single crystal. The analysis of the size distribution of SiNPs and gold nanorods is shown in Fig. 2.3 and Fig. 2.5 respectively. For this more than 1000 particles of each category were analyzed to get good statistics.



AR 2.5, length~50 nm

AR 3.8, length~38 nm

SAED

Figure 2.4 TEM Pictures of gold nanorods and their SAED**Figure 2.5** Size distribution of AuNRs showing rods with aspect ratios, left (2.5) and right (3.8)

The extinction coefficients of the prepared gold nanorods, was estimated using the methodology described in ref. [103], where they have shown a linear variation of extinction coefficient with respect to the aspect ratio as well as the L-SP resonance peak. The aspect ratio of our rods was obtained from TEM image analysis as shown in Fig. 2.4 and 2.5 and the L-SP maxima position was obtained from their extinction spectra using the UV-visible spectrophotometer. For the experiments conducted using these nanorods, the molar ratio of the differently coated rods and the dye molecules were kept same.

2.2.2 Hydrodynamic radius measurement

Dynamic light scattering:

The diffusion time of the particles in the probe volume is proportional to their hydrodynamic radii (When a charged particle is suspended in a liquid, counter ions are attracted at higher concentration closer to its surface forming a thin layer. This forms an electrical double layer. The particle and this double layer of ions adsorbed on to its surface move together as the kinetic unit or hydrodynamic unit as the particle diffuses through the solvent. The radius of these particles is called hydrodynamic radius). The hydrodynamic radius of the non-fluorescent particles suspended in aqueous medium can be easily measured by dynamic light scattering (DLS) methods.

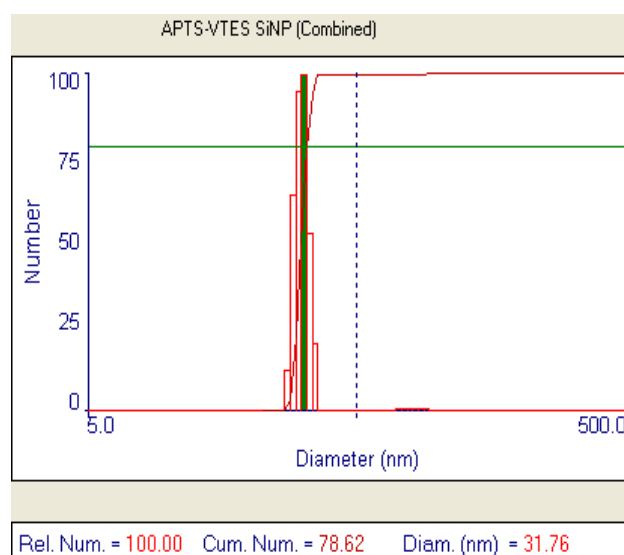


Figure 2.6 Showing the mean size (~ 31.76 nm) and distribution of SiNP-VA as measured by DLS. The polydispersity is $\sim 16\%$.

We measured it using particle size analyzer 90Plus, from Brookhaven. It can measure the size of particles in the range from ~ 1 nm to $6 \mu\text{m}$. It uses a 35 mW diode laser as the light source and the scattered signal is collected at 90° . The sample volume required is $\sim 3\text{ml}$. For correct measurements, the particles are diluted in a suitable solvent to single scattering regime. With this system an average diameter of the particles and

along with the distribution width (polydispersity) is obtained. Fig. 2.6 shows the size of SiNP as measured using 90Plus instrument. It is pertinent to note that the hydrodynamic size is slightly higher than that shown by TEM imaging. This is because of the counter ion layers attached to the charged particles which move together with the particle in the suspension as the hydrodynamic unit.

Fluorescence Correlation Spectroscopy:

Fluorescence correlation spectroscopy (FCS) is similar to DLS spectroscopy where the hydrodynamic radius of the particles is measured by monitoring their fluorescence. While both FCS and DLS use a small sample volume to noninvasively probe the concentration fluctuations, it is the enhanced sensitivity of fluorescence to conformational, environmental, and chemical changes in a system that allows FCS to be more useful in these scenarios than tracking scattered light [104, 105].

The FCS experiments were performed on a FCS spectrometer built around an Olympus IX71 inverted microscope. The excitation laser (SDL 532LN002T, 15 mW, 532 nm, Frequency doubled Nd: YVO₄, Shanghai Dream Laser, Shanghai, China) was coupled through the rear port of the microscope. The collimated laser light is passed through a dichroic filter, and focused on the sample with an Olympus 60x water immersion objective (N.A. = 1.2). The fluorescence emission from sample was collected using the same objective and reflected from the dichroic filter and passed through a long pass filter to eliminate the excitation light before detection using a single photon counting APD (SPCM-AQRH-13-FC, Perkin Elmer, Canada). The autocorrelation function of detected fluorescence intensity fluctuation was calculated using FLEX99OEM-12D correlator card.

2.2.3 Zeta potential measurements

Zeta potential is a measure of the stability of colloidal particles and is measured from the electrophoretic mobility of the kinetic unit under an applied field. The electrophoretic

mobility is defined as the electrophoretic velocity divided by the strength of the electric field which depends on the applied voltage and the electrode geometry.

$$V = \mu_e E$$

Where V is the velocity, μ_e is the mobility and E is the applied electric field. From the measured velocity the mobility and zeta potential are calculated typically (under certain approximations) as follows:

$$\mu_e = (2e\zeta)/(3\eta), \text{ where } \zeta \text{ is the zeta potential, } \eta \text{ is the viscosity.}$$

To measure zeta potential, electric field is applied to the nanoparticle dispersion in a liquid. As these are charged particles, they will move to the respective oppositely charged electrodes. The direction of their movement indicates the kind of charge on them and the velocity with which they move is proportional to the magnitude of the charge. In the present thesis, the system used for measurement of Zeta potential is 'ZetaPlus' from Brookhaven Instruments Corporation. It can measure zeta potential of nanoparticles from -150 to 150mV, size range from 10 nm to 30 μm with accuracy $\pm 2\%$.

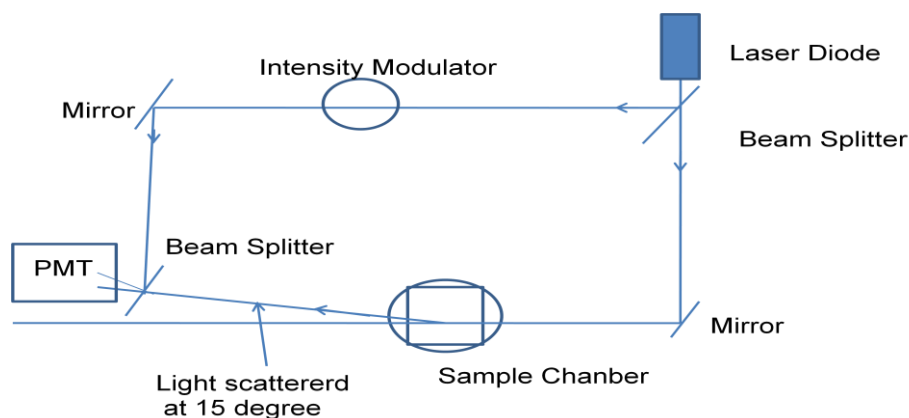


Figure 2.7 Optical heterodyne used for zeta potential measurement.

In the Zeta plus system, a laser beam is passed through the sample placed in a cell which has two electrodes to provide the electric field as shown in Fig.2.7. As the particles are moving in the electric field, light which is scattered by the particles is Doppler shifted.

This shift $\sim 100\text{Hz}$ is measured by making use of the principle of optical heterodyning. In this a portion of the beam is split off and then recombined with the scattered beam after it is modulated at 250 Hz. In the absence of field, the power of the signal from the detector would have sharp peak at 250 Hz. When field is applied, there is a shift in the frequency due to the Doppler velocity. If the resultant frequency is less than 250Hz the particles are negatively charged and vice versa. From this Doppler frequency shift, which is proportional to electrophoretic velocity, mobility can be measured. Zeta potential depends upon charge and solution condition such as pH in water, electrolyte concentration etc. and therefore these are needed to be specified. The square of zeta potential is proportional to force of repulsion between two charged particles. As a general experience for zeta potential $> +25\text{mV}$ and $< -25\text{mV}$, the repulsion is considered to be sufficient and the dispersion is likely to be stable. Without steric hindrance, to keep particles apart, as the zeta potential approaches zero, dispersion is likely to be unstable. The Zeta potential values of NPs are given in respective chapters.

2.2.4 FTIR spectroscopy

Fourier transform infra-red (FTIR) spectrometer provides information of various vibrational transitions. The principle of FTIR spectrometer is different from that of normal dispersive spectrometer which separates the optical frequencies spatially. FTIR spectrometer modulates different frequencies of the light and uses Fourier Transform to separate them. The heart of the FTIR spectrometer is a Michelson interferometer, which in simplest form consists of a fixed mirror, a moving mirror and a beam splitter. The light from the infrared source, a glowbar, enters the interferometer and is divided into two equal beams by a beam splitter. One beam is reflected towards a fixed mirror, which reflects it back towards the beam splitter. The other beam is transmitted towards the moving mirror, which also reflects it back towards the beam splitter. The moving mirror introduces a continuously changing path difference between the two beams. As the

moving mirror is scanned, the two returned beams interfere with different phases. This creates intensity variations. At a given path difference, the interference is constructive for some frequencies and destructive for others. As the optical path difference is continuously changing, the various frequencies present in the beam are modulated at different times as the mirror is moved. After leaving the interferometer, the modulated light passes through the sample.

If the sample contains non symmetrical molecules, these will absorb IR at specific frequencies. The remaining light then reaches the detector which converts it into an electrical signal. The plot of the interference intensity, called an interferogram, as the function of the position of the mirror is related to the intensity of light as a function of frequency by mathematical relation called Fourier transform. Performing a Fourier transform, with the help of computer program, on the interferogram yields a raw spectrum, which is a graph of the light intensity at the detector versus the optical frequency. This type of the spectrum contains information about the sample as well as the whole instrument response which include the source, all the optical components, ambient air, as well as contamination in the optical path. To extract the sample information from this raw data, a reference spectrum is acquired under the same ambient condition without the sample. The data acquisition software uses the reference and the raw data to normalize the sample spectrum with the instrument response. The FTIR spectrometer used to characterize the NPs was FT-IR, FTLA 2000 MB 104, from ABB Bomem. The spectra were taken at resolution of 1 cm^{-1} . To get good signal to noise ratio ~ 40 scans per sample were taken (depending upon the sample).

FTIR spectra of SiNP-V, SiNP-VA, along with the silica precursors VTES and APTS and the surfactant AOT are shown in Fig. 2.8. In the spectra of SiNP-V and SiNP-VA, the absence of the dominant peak of asymmetrical sulphonate stretch peaks of AOT at 1248 cm^{-1} indicates the removal of surfactant AOT from the SiNP aqueous suspension after dialysis. The strong peaks at $\sim 1043 \text{ cm}^{-1}$ and $\sim 1130 \text{ cm}^{-1}$ are assigned to Si-O-Si

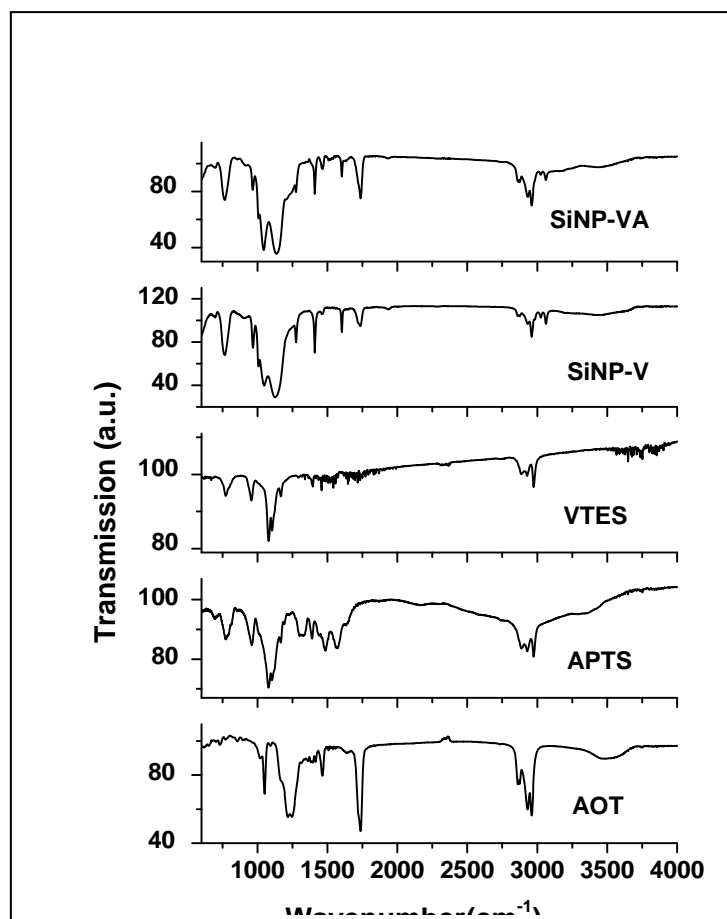


Figure 2.8 FTIR spectra of different components of ORMOSIL NP.

stretch, which indicates polymerization and are absent in the APTS and VTES whereas the peaks at 1104 and 1081 cm^{-1} , are assigned to Si–O–C in VTES and APTS, which are absent in the nanoparticles [97]. The hump at the $\sim 3400\text{ cm}^{-1}$ and 1640 cm^{-1} in both APTS and SiNP-VA denotes the presence of weak amine N-H stretch and bend band respectively.

The coatings on the gold nanorods were also confirmed by FTIR spectroscopy. In Fig.2.9, the FTIR spectra of coated gold rods along with the corresponding coating materials: CTAB, PSS, PAH and PDDAC are shown in graphs A, B, C and D respectively. The presence of characteristic IR peaks of the polymers (black) on the coated rods (in red), with few cm^{-1} shifts, confirms the coating. Graph A shows the

spectra of CTAB coated rods where the peaks at $\sim 2915\text{ cm}^{-1}$ and $\sim 2850\text{ cm}^{-1}$ correspond to CH asymmetric and symmetric stretching respectively.

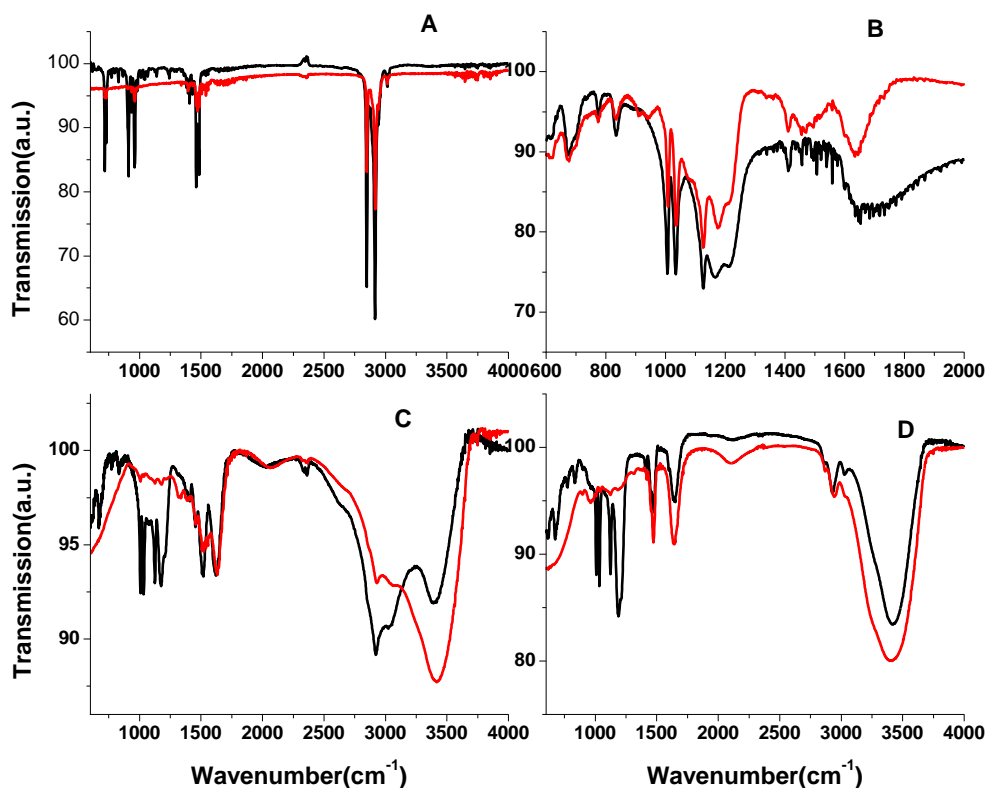


Figure 2.9 FTIR spectra of four coated gold rods (in red), coated with A)CTAB, B)PSS, C)PAH and D)PDDAC along with the respective polymers (black)

In case of PSS coated rods, graph B, the presence of sulphonate S=O asymmetric stretch at $\sim 1215\text{ cm}^{-1}$ and $\sim 1175\text{ cm}^{-1}$ and symmetric stretch frequencies at 1035 cm^{-1} confirm PSS coating. In graph C, the PAH coating on the rods is confirmed by the presence of the NH absorption at $\sim 3400\text{ cm}^{-1}$, the C-C stretch at 1460 cm^{-1} and NH_2 scissoring at $\sim 1622\text{ cm}^{-1}$. Similarly, in graph D, the presence of NH absorption at $\sim 3400\text{ cm}^{-1}$, ethylene at 1630 cm^{-1} and CH_3 bend at 1471 cm^{-1} in PDDAC coated rods as well as in polymer confirm coating.

2.3 UV-visible spectroscopy

2.3.1 Absorption spectroscopy

The steady state absorption spectra were measured using a UV–VIS absorption spectrometer model Cintra 20 (GBC Scientific Equipments Ltd.). It is a dual beam direct ratio recording system having Czerny-Turner style monochromators with holographic grating and variable slit widths and the detector is a photomultiplier tube. Automatic lamp peaking and wavelength calibration is done on power up. The excitation sources are 35 W tungsten–halogen lamp and 30 W deuterium lamp which change automatically at selected wavelength. Wavelength range is 190-900 nm with spectral band pass from 0.2 nm to 5 nm variable in steps of 0.1 nm with wavelength accuracy ± 0.2 nm. Photometric linearity is better than 1% up to absorbance 3. In our studies, all the measurements were done at the resolution of 1 nm.

2.3.2 Emission spectroscopy

The steady state emission measurements were carried out using Spex Fluorolog 2 fluorimeter. It has a 450 W Xenon lamp as the excitation source. The excitation light is passed through a 20 cm monochromator and is focused on the sample placed in the sample chamber at spot size ~ 2 mm by 6 mm. For most of the samples, the emission was collected at 90 degree (& at 15 degree, front face, for optically dense samples). The emitted fluorescence after passing through a double monochromator (each 20cm focal length) was collected by PMT (Hamamatsu R955) which is sensitive from 250 to 850 nm. With each slit as 1mm, the system resolution was 4 nm. All the measurements were done at this resolution.

2.3.3 Fluorescence lifetime measurement

The time resolved fluorescence measurements were done using time correlated single photon counting (TCSPC) system. This method of fluorescence decay time measurement is based on the concept that after an excitation event, the temporal probability distribution

of emission of a single photon yields the actual intensity against time distribution of all the emitted photons. In the experiment this probability distribution is constructed by sampling a single photon emission, following a large number of excitation events.

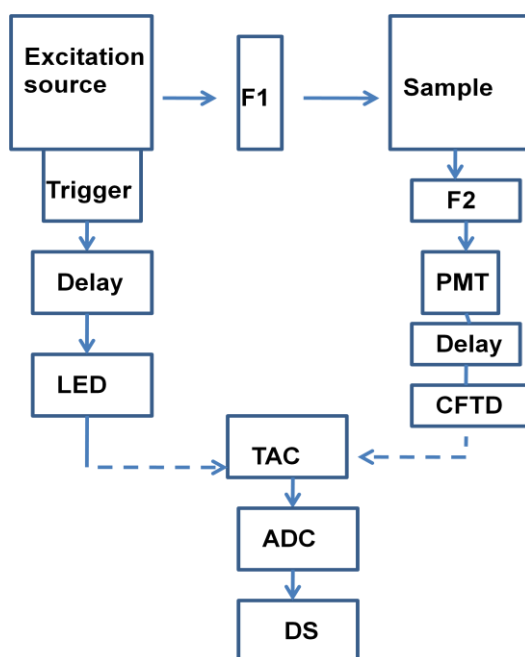


Figure 2.10 Block diagram representing the concept of time correlated single photon counting. Here Excitation source is a pulsed light source, F1 and F2 are the filters/monochromators, PMT is a fast photomultiplier tube, 'Delay' are the delay lines to adjust the start and stop pulse times. LED is the leading edge timing discriminator, CFTD is the constant fraction timing discriminator, TAC is time to amplitude convertor, DS is the data storage device (computer). Recreated from ref. [106].

Fig.2.10 shows the block diagram of a TCSPC set-up. Here a trigger pulse generates an electrical pulse at a time which is exactly correlated with the time of generation of the pulse of the excitation source (a fast optical pulse). This pulse is routed through a discriminator to the start input of the time to amplitude convertor, (TAC) which initiates charging of a capacitor. In the mean time the optical pulse excites the sample, which subsequently fluoresces. The intensity of the fluorescence at the photomultiplier tube is so adjusted that at the most one photon is detected for each exciting event. The electrical signal generated due to this photon stops the charging ramp in the TAC, and

gives out a pulse, the amplitude of which is proportional to the charge in the capacitor and hence to the time difference between START and STOP pulses.

The TAC output pulse is given a numerical value, depending upon its amplitude, in the analogue-to-digital converter and a count is stored in the data storage device against an address corresponding to that number. This excitation and storage process is repeated until the histogram of the number of counts against address number in the storage device represents the decay curve of the sample to a required precision. For deconvolution the temporal profile of the exciting pulse is also collected in the similar way by replacing the sample by light scatterer [106].

The emission lifetimes of the fluorophores were recorded by using a TCSPC module Lifespec-RED from Edinburgh Instruments. The excitation source was either a 40 ps Pico-Quant laser diode (LDH-P-C-400) at 406 nm (operated at 2.5 MHz repetition rate, average power <1 mW) or the second harmonic output of the tunable femto second laser (Coherent Verdi pumped by Mira) having pulses of ~100 fs duration. Coherent model 9200 pulse picker was used to select pulses at 3.8 MHz repetition rate. The fluorescence was collected at 90 degree. Proper high pass and low pass filters were used to avoid the excitation pulse scattered photons to enter the collection lens. The detector was a thermoelectric cooled Hamamatsu photomultiplier tube (H7422) or microchannel plate PMT (R3809U-50). The instrument response function (IRF) along with PMT was ~200ps whereas with MCP PMT was ~50ps. The fluorescence decays were deconvoluted from the IRF using the iterative software based on global least squares analysis algorithm provided by the manufacturer. The goodness of the fit was judged by the reduced chi-square values and visual inspection of the plots of weighted residuals. For time resolved anisotropy calculations the anisotropy was first constructed from the parallel and perpendicular polarized traces and then deconvoluted from the IRF using the above mentioned algorithm.

2.4 MTT Assay, to determine the cell survival

This is a quantitative colorimetric assay proposed by Mosmann in 1983, for determining mammalian cell survival and cell proliferation [102]. The assay is dependent on the reduction of the tetrazolium salt MTT (3-(4,5-dimethylthiazol-2-yl)-2,5-diphenyltetrazolium bromide) by the mitochondrial dehydrogenase generated from viable cells which leads to the formation of a blue formazan product. The assay measures cell respiration and the amount of formazan produced is proportional to the number of living cells present in culture. In our experiments, 100 μ l of medium containing MTT (10 μ l, 5 mg/ml) was added to each well containing the cells, in the 96 well standard microplate, after the treatment followed by incubation for 4 h. The culture medium was then removed and the formazan crystals formed were dissolved in isopropanol-HCl (0.4 N) solvent mixture. The optical density of the dissolved formazan was measured at 570 nm using a microplate reader (Power Wave 340, Biotech instruments, USA).

2.5 Molarity calculation of the NPs

To maintain the desired dye to NP ratio in the experiments, the molarity of ORMOSIL NPs and gold nanorods was calculated as follows:

For calculating the molarity of ORMOSIL NPs, first the average size of SiNP was measured by either TEM or by light scattering methods which was \sim 30 nm. The dry weight of 1ml colloid was obtained as \sim 5 mg. The density of SiNP was taken as \sim 1.9 g/cc. For the volume of 1NP = $\frac{4}{3} \pi r^3$, keeping $r = 15$ nm, the average mass of 1 NP was obtained as $26,847 \times 10^{-21}$ gm. Hence, the molarity of the prepared SiNP was obtained \sim 300 nM. The molarity of gold nanorods was calculated by first knowing their aspect ratio. This was done by measuring dimensions (length and width) of a sufficient number (\sim 1000) of rods (of each type) so as to generate the histogram as shown in Fig.2.5. Rest of the details are discussed in section 2.2.1.

2.6 Conclusion

The NPs were synthesized, following wet chemical methods and characterized using TEM, light-scattering methods, Zeta potential measurements and FTIR spectroscopy for their size, surface properties and stability. These were stored as colloidal suspensions and used for the studies described in the following chapters.

CHAPTER 3

PHOTOPHYSICAL STUDIES ON THE INTERACTION OF ANS, TNS & MC540 WITH ORMOSIL NANOPARTICLES

In this chapter we describe the results of our studies carried out on interaction of ORMOSIL NPs (SiNPs) with negatively charged fluorophores 8-Anilino-1-naphthalenesulfonate (ANS), 6-p-toluidino-2-naphthalenesulphonate (TNS) and Merocyanine 540 (MC540). The effect of binding, of these dyes with SiNPs, on their excited state processes is discussed. We also compare the photophysics of MC540 with its complex with SiNP-VA and liposome. The photostability studies of the MC540-NP complex and its light induced toxicity in cancer cells are also presented.

3.1 Introduction

Negatively charged fluorophores like ANS, TNS and MC540, whose excited state processes are dominated by a significant change in structure due to processes such as

Work discussed in this chapter resulted in the following publication:

1. 'Interaction of ANS and TNS with organically modified silica nanoparticles in aqueous media' B. Jain, A. Uppal, P. K. Gupta, K. Das, *Advanced Science Letters*, Vol. 3, pp. 225-230 (2010).
2. 'Light induced toxicity of merocyanine-540-silica nanoparticle complex,' K. Das, A. Uppal, B. Jain, B. Bose, and P. K. Gupta, *Journal of Nanoscience and Nanotechnology*, Vol. 9, pp. 1-4 (2009).

electron transfer or photoisomerism, can get affected on binding with SiNPs due to electrostatic interaction. The fluorescence of ANS and TNS is known to be markedly sensitive to the environment polarity and viscosity [107, 83, 84, 108, 87]. While, these are almost nonfluorescent in a polar medium like water, non-polar/viscous environments cause the fluorescence to be increased by several orders of magnitude. This has been attributed to twisted intramolecular charge transfer (TICT) from the anilino group (for ANS) or p-toluidino group (for TNS) to the sulphonate group. The chemical structures of ANS and TNS are shown in Fig. 3.1. In polar solvents, this nonradiative TICT process is very efficient leading to weak fluorescence. In nonpolar medium the TICT process is suppressed which leads to the enhancement of fluorescence. The intensity, quantum yield and lifetime of ANS fluorescence depends on the geometry of the phenyl ring twist about the bond connecting it to the naphthalene moiety [109]. These dyes have been extensively utilized for the characterization of protein binding sites. D. Matulis et al showed that ANS binds stronger to BSA than inorganic anions [110]. Enhanced binding to protein has been partially ascribed to the large anilinonaphthalene organic moiety of ANS as well as the ion pair formation. Binding to proteins thus comes from both its nonpolar anilinonaphthalene and the negatively charged sulfonate groups (Fig. 3.1).

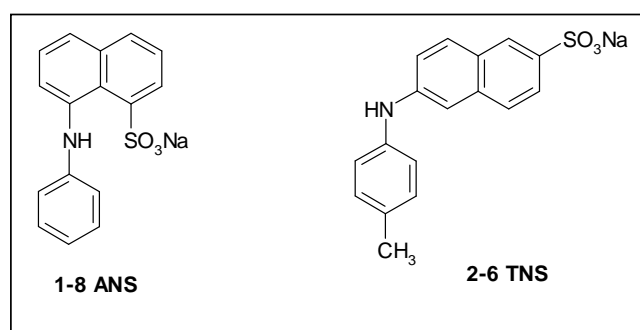


Figure 3.1 Chemical structures of aniline naphthalene sulphonates used in this study

MC540 is a lipophilic, cyanine dye which readily binds to membranes, macromolecules and organized assemblies [88, 111, 112, 113] and has been used for

photodynamic inactivation of enveloped viruses in blood products and leukaemia cells [114, 115]. Its optical properties are reported to be very sensitive to environmental polarity, viscosity etc. [87] and therefore it has been used in variety of applications such as trans membrane potential monitoring in biological samples [116], investigating lipid packing in membranes [117, 118], etc.

In aqueous solution MC540 exists as a mixture of monomers and dimers. While the monomeric form of the dye is weakly fluorescent, its dimeric form is nonfluorescent [86, 119]. The relatively low singlet oxygen quantum yield of the dye is ascribed to the efficient excited state photoisomerization around the central double bond (Fig. 3.2).

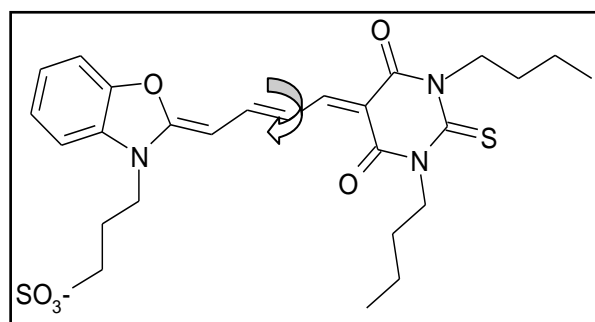


Figure 3.2 Photoisomerization of MC540 around the central double bond

This photoisomerization process accounts for the main non-radiative decay pathway for MC540 in the excited state [88]. In addition, the dye is also observed to be readily photodegradable in aqueous solution which might result from the generation of the radical species involved during the photoisomerism process. Therefore, a reduction in the photoisomerization rate by appropriate binding that hinders intramolecular motion may enhance the singlet oxygen yield and photostability of the dye. Indeed it has been observed that the singlet oxygen quantum yield of the drug bound to liposomes is ~ 20 times greater than the free drug [120]. Another simple approach to achieve a reduction in the photoisomerization rate of the drug will be to restrict its intramolecular motion by electrostatically binding the drug with positively charged nanoparticles. In this

chapter we have first used ANS and TNS to photophysically characterize the SiNP-V and SiNP-VA and then studied the photophysics of these probes in the SiNP environments and protein and investigated the role of 3-amino-propyl group in the binding process. We also studied the interaction of MC540 with SiNP-VA suspended in aqueous environment and compared its photophysics with that of only dye and dye complexed with liposome (model membrane). This was followed by photostability studies of dye-NP complex and its light induced toxicity in cancer cells.

3.2 Experimental Methodology

For photophysical studies:

Details of the nanoparticles SiNP-V and SiNP-VA and liposomes used for our studies are given in chapter 2. Bovine serum albumin (BSA), ANS, TNS and MC540 were purchased from Sigma and used as received. The experimental set used for Zeta potential measurements, and steady state absorption and emission measurements are detailed in chapter 2. Emission lifetimes and anisotropies were recorded by excitation at the second harmonic of Ti-sapphire femtosecond laser operating at wavelength 740 nm (to excite ANS and TNS at 370 nm) and 900 nm (to excite MC540 at 450 nm) and using TCSPC (details are in chapter 2 and ref.121). For all experiments performed the concentration of ANS, TNS and MC540 were fixed at 10 μ M and 1 μ M respectively. The concentrations of BSA and SiNP were used as 15 μ M and \sim 1.0 mg/mL respectively.

For Cellular studies:

Phototoxicity studies were done using MCF cells purchased from national centre for cell sciences, Pune, India. Experimental samples were prepared by Dr. Abha Uppal, details are given in reference 122. For irradiation, cells in monolayer were kept in phosphate buffer saline (PBS) containing 5 mM glucose. A 450 to 650 nm bandpass filter was used

to select the wavelength of irradiation from the broadband output of a xenon lamp source. Samples were kept at a distance of 30 cm from the light source and the power incident at the sample was measured by an OPHIR power meter (3A sensor head). Following irradiation at different light dose, the media were replaced with fresh growth medium at pH 7.4. After 24 h, MTT assay was performed to determine the cell survival following the method described by Mosman [102] (details are described in chapter 2). Each irradiation experiment was repeated thrice and for each of these experiments a corresponding control experiment in which cells, devoid of drug and SiNP-VA, exposed to similar light dose was also carried out.

3.3 Results and Discussion

The effect of pH on the zeta potential of the SiNP's is shown in Fig. 3.3.

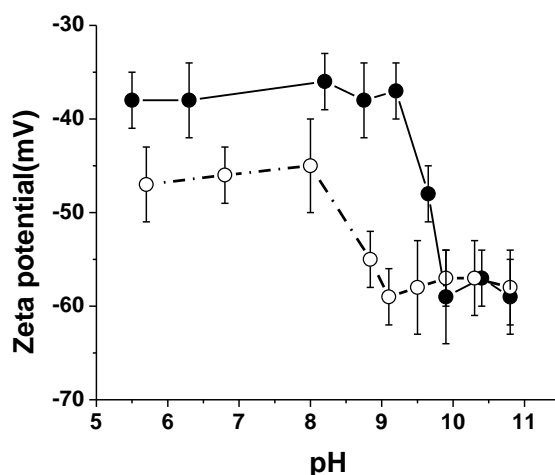


Figure 3.3 *pH titration curves: Variation of zeta potential of SiNP-VA (solid) and SiNP-V (hollow) with pH.*

As shown in the figure, the zeta potential of SiNPs decreases as the pH is changed from ~5.5 to ~11.0. For SiNP-V the zeta potential starts to decrease after pH 8.0 and stabilizes to a value of ~ -58.0 mV above pH 9.0. This change can be attributed to the acid-base equilibrium of the silanol groups present at the surface. It has been earlier reported that

for macroscopic silicon dioxide-water interface the surface silanol groups have two pK_a values one at 4.5 and the other at 8.5 [123]. For SiNP-VA the zeta potential however starts to decrease after pH 9.2 and reaches a minimum of ~ -58.0 mV at pH ~ 10.0 and stabilizes after that. The observed difference in the trend of zeta potential vs. pH curves may be attributed to the presence of combined acid-base equilibrium of the surface silanol and 3-amino propyl groups present in SiNP-VA. At neutral pH, the zeta potential for SiNP-V is observed to be around -45.0 ± 3.0 mV while that for SiNP-VA is observed to be around -36.0 ± 3.0 mV (Fig. 3.3). This difference in the zeta potential may be attributed to the presence of the 3-amino propyl groups at the surface in SiNP-VA. At pH 7.0 the amine groups, present at the surface, are expected to be positively charged as the pK_a value of the 3-aminopropyl group of APTS is ~ 9 [124]. This positive charge neutralizes to some extent the negative charges caused by the presence of surface silanol (Si-O⁻) groups and increases the zeta potential for SiNP-VA (making it more positive) compared to SiNP-V.

3.3.1 Spectroscopic studies of ANS and TNS with SiNP-V and SiNP-VA

The fluorescence properties of ANS and TNS in the presence of ~ 1.0 mg/mL SiNP-V and SiNP-VA in aqueous medium at neutral pH are shown in Fig. 3.4 and the corresponding fluorescence parameters are provided in Table 3.1. For comparison, the fluorescence of these probes in neutral water and in the presence of $15\mu\text{M}$ BSA are also provided in Fig. 3.4. The emission intensity and lifetime of the probes follow the order: water < SiNP-V < SiNP-VA < BSA. As noted earlier, the fluorescence of both ANS and TNS are dependent on the polarity of the surrounding environment [107, 83, 84,108]. In the highly polar medium, water, the fluorescence properties of both probes are weak due to efficient nonradiative TICT process. Compared to water, a marginal enhancement in fluorescence was observed in the presence of SiNP-V and a significant enhancement was observed in the presence of SiNP-VA indicative of an interaction between the probes and SiNP-VA.

Although the interior of both nanoparticles are reported to be hydrophobic [51, 124], the fluorescence properties of the probes in the presence of these nanoparticles suggest that surface property of the nanoparticle plays an important role in the probe-nanoparticle interaction.

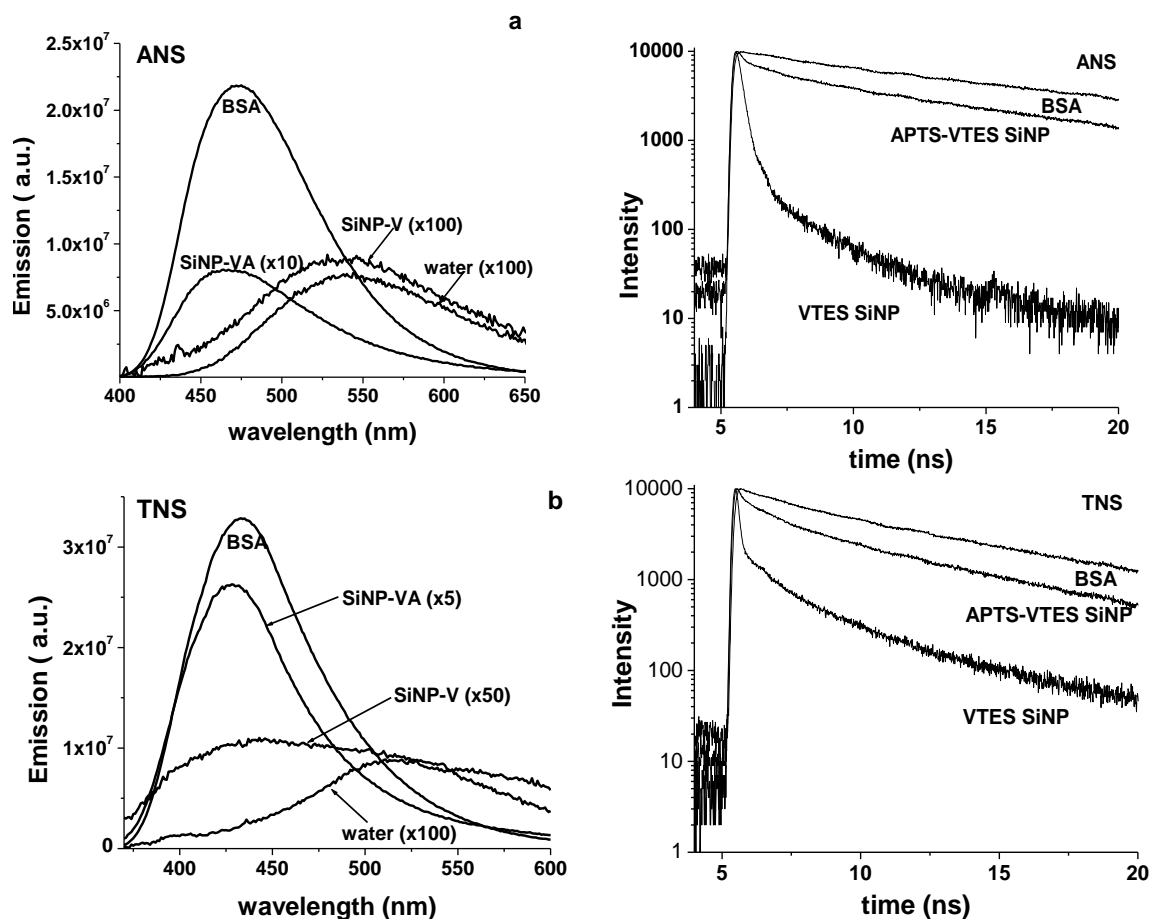


Figure 3.4 Fluorescence ($\lambda_{ex} = 370$ nm) emission (left) and lifetimes (right) of ANS (a) and TNS (b) in presence of BSA, SiNP-V, SiNP-VA and water. Some spectra are magnified for comparison.

Significant interaction between the negatively charged probes and SiNP-VA having a positive zeta potential value as compared to SiNP-V is indicative of an electrostatic interaction mechanism operative in the case of SiNP-VA. This may be attributed to electrostatic binding between the negatively charged ANS & TNS with positively charged 3-amino propyl groups present in SiNP-VA. Since the pK_a of the 3-amino propyl group is reported to be ~ 9.0 , the presence of electrostatic interaction mechanism can be tested by

Table 3.1 Fluorescence parameters of ANS and TNS in different environments

System	Em. Max. (nm)	QY	Lifetime (ns)								k_{nr} ($\times 10^{-9}$ s)	k_r ($\times 10^{-9}$ s)
			χ^2	τ_1	a_1	τ_2	a_2	τ_3	a_3	τ_{av}		
10 μM ANS in												
Water	540	0.004 ^a	0.20 ^a								5.0	0.015
BSA	472	0.580	1.25	--	--	9.00	0.28	15.0	0.72	13.3	0.03	0.044
SiNP-VA	465	0.020	1.15	--	--	2.30	0.13	11.00	0.87	9.9	0.10	0.002
SiNP-V	535	0.004	1.00	0.20	0.79	1.25	0.10	4.30	0.11	0.8	1.25	0.005
Isopropanol	470	0.480	1.00	--	--	--	--	7.40	100	7.4	0.07	0.065
Isopropanol + 2.36 (M) VTES	472	0.400	1.10	--	--	--	--	6.40	100	6.4	0.09	0.063
Isopropanol + 2.14 (M) APTS	476	0.234	1.10	--	--	1.40	0.21	4.30	0.79	3.7	0.21	0.063
10 μM TNS in												
Water	515	0.001 ^a	0.06 ^a								16.65	0.02
BSA	433	0.256	1.13	--	--	2.00	0.11	8.20	0.89	7.5	0.10	0.034
SiNP-VA	427	0.020	1.10	--	--	1.50	0.23	6.90	0.78	5.7	0.17	0.004
SiNP-V	445	0.003	1.10	0.20	0.36	1.40	0.28	5.60	0.36	2.5	0.40	0.001
Isopropanol	418	0.414	1.10	--	--	--	--	5.60	100	5.6	0.10	0.074
Isopropanol + 2.36 (M) VTES	425	0.410	1.10	--	--	--	--	4.80	100	4.8	0.12	0.085
Isopropanol + 2.14 (M) APTS	427	0.087	1.10	--	--	1.30	0.79	2.40	0.21	1.5	0.61	0.058

^a Data taken from reference 84 and 125.

varying the pH of the medium. Consistent with the fact that neutralization of amino groups should result in a decrease in the electrostatic binding and hence fluorescence, the integrated emission intensity of the probes was observed to decrease after pH \sim 9.0 as shown in Fig. 3.5, a & b.

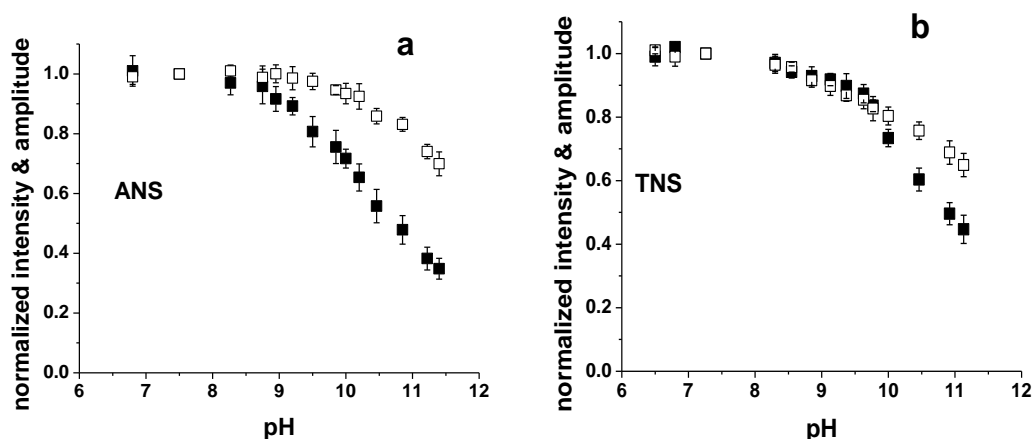


Figure 3.5 pH titration curves: Variation of fluorescence ($\lambda_{ex} = 370$ nm) with pH of ANS (a) and TNS (b) in presence of SiNP-V (solid) and SiNP-VA (hollow). The black squares represent the normalized changes in integrated emission intensity and the hollow squares represent the normalized changes in the amplitudes of the long lifetime component obtained from a global fit. Please see text for more details.

The fraction of probe molecules bound to SiNP-VA can also be estimated from the amplitude of the long lifetime component. However, since the decays were found to be wavelength dependent, the amplitude of the long lifetime component were obtained by collecting the decay traces over the ‘whole band’ at different pH, and then by performing a global fit of the decay traces. The changes in the number of bound probes with pH estimated in this way were also observed to be consistent with changes observed for integrated emission intensity (hollow squares in Fig. 3.5).

It is thus clear that electrostatic interaction plays an important role in the binding process. When we compared fluorescence properties of the probes bound to BSA and SiNP-VA some interesting observations were revealed (Fig. 3.4 & Table 3.1). The

emission maxima of the probes were observed to be distinctly blue shifted when they were bound to SiNP-VA indicating that in this case the probes were experiencing a less polar environment than BSA. This implies that the other emission properties like emission intensity and lifetime should be at least equal if not greater than that observed in the presence of BSA. Fluorescence decay of the probes bound to either BSA or SiNP-VA could be satisfactorily fitted with a double exponential. Compared to BSA when the probes are bound to SiNP-VA the average lifetimes of the probes were observed to be marginally smaller (~1.3 times each) while the quantum yield of emission was observed to be significantly smaller (~29 and ~13 times for ANS and TNS respectively). These results show that compared to protein the binding with SiNP-VA affects the nonradiative rates marginally but decreases the radiative rates significantly (20 and 11 times for ANS and TNS respectively). This is indicative of a quenching mechanism present in SiNP-VA.

For understanding this aspect better, fluorescence of ANS & TNS in isopropanol and with VTES and APTS was studied. As shown in Fig. 3.6, the strong fluorescence of ANS & TNS in isopropanol is quenched by both VTES and APTS and the nature of quenching is both static and dynamic (corresponding data presented in Table 3.1). The quenching by APTS is more severe than VTES. This may be attributed to the amine groups present in APTS, which are well known quenchers of fluorescence. This result suggests that fluorescence of these probes, when bound to SiNP, may get quenched.

Although a comparison of the radiative and nonradiative decay rates of the probes bound to SiNP-VA indicated that quenching is primarily static in nature, we further investigated this aspect by studying the fluorescence anisotropy decay of the probes when bound to SiNP-VA and compared that with BSA. The anisotropy decays are provided in Fig. 3.7 and the corresponding parameters are provided in Table 3.2. The data can be fitted satisfactorily to a bi-exponential decay model represented by:

$$r(t) = r_0 [a_1 \exp(-t/\tau_1) + a_2 \exp(-t/\tau_2)]$$

where r_0 is the initial anisotropy and τ_1 and τ_2 are the time constants for the decay of r_0 is

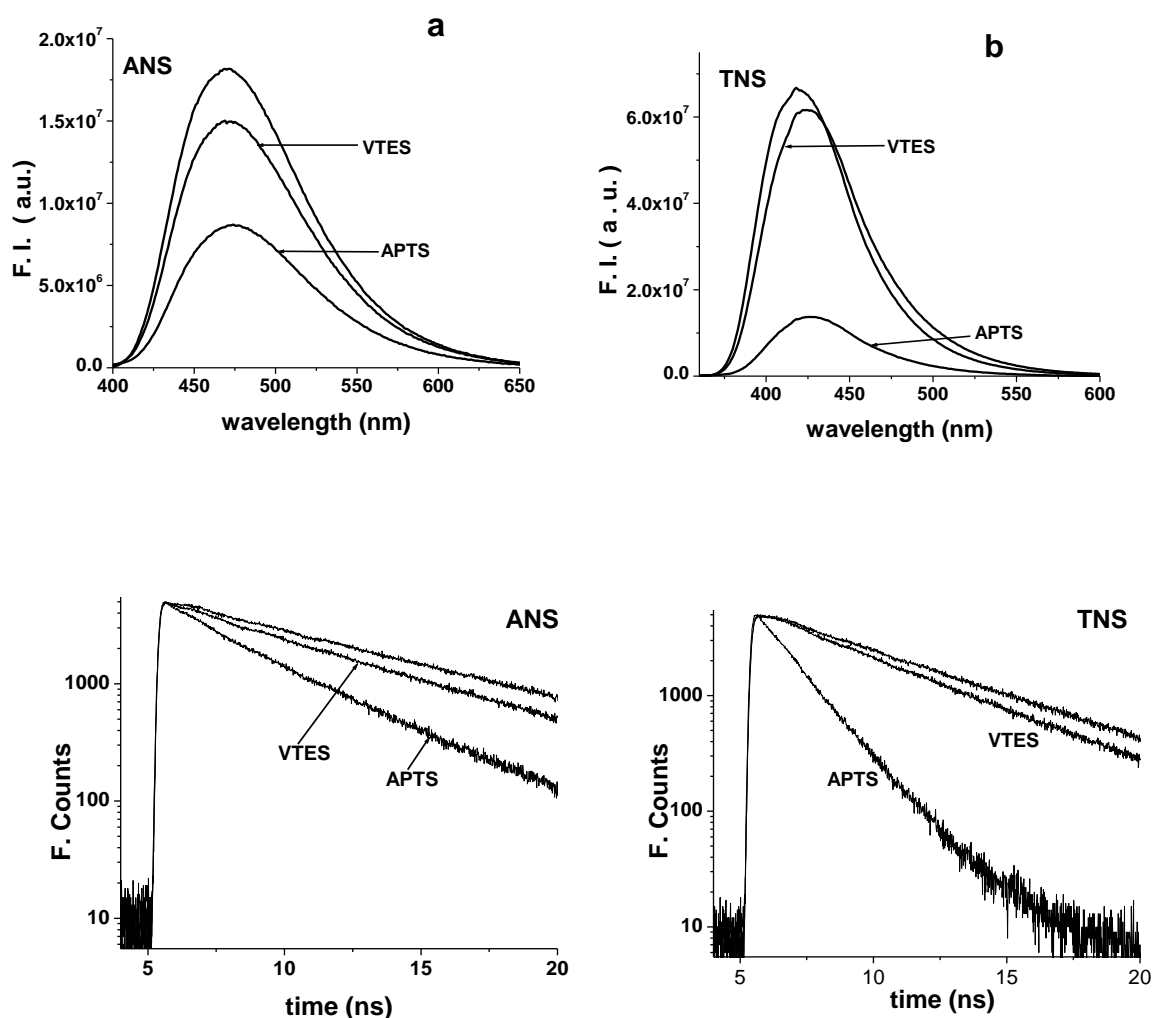


Figure 3.6 Fluorescence ($\lambda_{ex} = 370$ nm) emission (top) and lifetimes (bottom) of ANS (a) and TNS (b) in isopropanol, and isopropanol containing 2.36 (M) VTES and 2.14 (M) APTS.

the initial anisotropy and τ_1 and τ_2 are the time constants for the decay of r_0 having pre-exponential factors of a_1 and a_2 respectively. The component τ_1 represents the overall factors responsible for faster dephasing of anisotropy including local motion and quenching of the fluorescence of the probe. The slower component τ_2 represents the overall motion of the probe-BSA or probe-SiNP complex.

For protein bound probe, the overall motion is characterized by a time constant of 40-50 ns as observed earlier [109]. For probe bound to SiNP-VA (whose size is much larger than BSA) we note that the experimental time window is not sufficient enough to

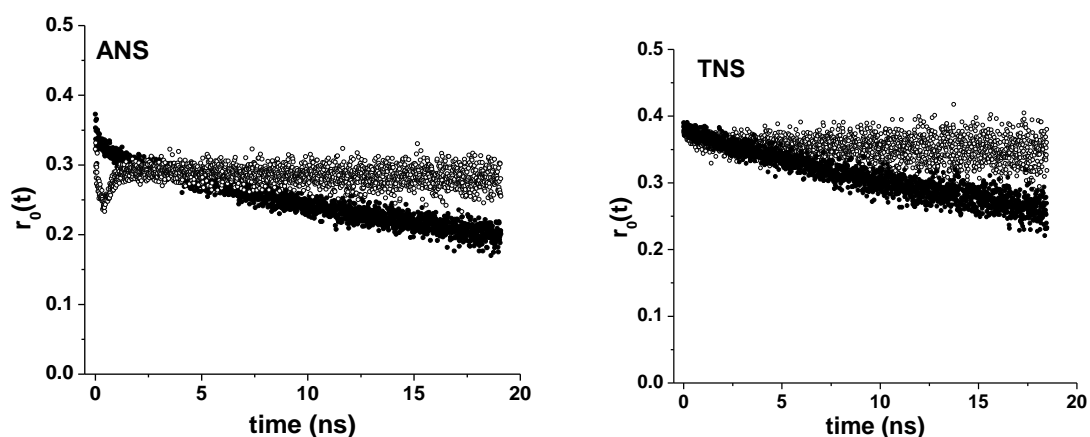


Figure 3.7 Fluorescence ($\lambda_{ex} = 370$ nm) anisotropy decay curves along with fitted curves of ANS (left) and TNS (right) in presence of BSA and SiNP-VA. The fitted anisotropy parameters are given in Table 3.2.

give a correct estimate of the overall motion of the nanoparticle. The initial fluorescence anisotropy decay of ANS bound to either BSA or SiNP-VA shows distinctly a fast component. For SiNP-VA, $r(t)$ initially shows a dip and then rise. This type of anisotropy decay has been previously observed for fluorophores having very fast and slow rotational motions of the excited dipole [126, 127].

Table 3.2 Anisotropy parameters of ANS and TNS in different environments

System	a_1^a	τ_1 (ns)	τ_2 (ns)	r_0
10 μM ANS in				
SiNP-VA	0.30	0.20	∞^b	0.39
BSA	0.15	1.5	40.0	0.33
10 μM TNS in				
SiNP-VA	0.07	1.0	∞^b	0.38
BSA	0.30	5.0	50.0	0.38

^a Pre-exponential factor

^b The time window is not sufficiently long enough to measure this time constant and hence it is shown as infinity.

For SiNP-VA bound ANS the faster component comes out to be ~ 200 ps accounting for 30% of anisotropy decay whereas for BSA bound ANS this is 1.5 ns accounting for 15% of anisotropy decay. We note here that due to the limited time resolution (~ 200 ps) of our

setup the estimation of the faster component of ANS bound to SiNP-VA is only approximate, nevertheless its presence shows significant dynamic fluorescence quenching of ANS when compared to that in BSA.

In contrast the anisotropy decay of TNS in these two systems clearly does not show the presence of a fast component (Table 3.2). A biexponential fitting of the anisotropy decay of TNS bound to SiNP-VA shows no significant fast component whereas when it is bound to BSA it shows the presence of a 5 ns component with a 30% weight, which is indicative of the local motion of the protein bound probe. Thus, for TNS bound to the nanoparticle anisotropy experiments suggests that only static quenching mechanism is operative.

The significantly higher decrease in quantum yield and hence the radiative rate as well as observation of a faster anisotropy dephasing time in ANS compared to TNS in SiNP-VA suggests that in addition to quenching induced by APTS and/or VTES the structure of the probes might also be responsible. The non-radiative TICT process, which involves twisting between the donor and the rest of the molecule, is expected to be affected differently for ANS and TNS when they are bound to the 3-amino propyl groups present at the surface of SiNP-VA. For ANS, the donor and acceptor are on the same side of the naphthalene moiety but for TNS they are on the opposite side (Fig. 3.1). The presence and absence of a faster anisotropy dephasing time for ANS and TNS respectively suggests that in addition to the quenching by APTS and/or VTES, the TICT process might be operative in a greater extent in ANS compared to TNS.

3.3.2 Spectroscopic studies of MC540 with SiNP-VA

The absorption, emission and fluorescence lifetimes of MC540 in aqueous medium in the presence and absence of SiNP are shown in Fig. 3.8. In aqueous medium the absorption band of the dye is broad with two peaks centered at 505 and 536 nm. The emission peak of the free dye is at 570 nm having a quantum yield of 0.03 and lifetime of ~100 ps.

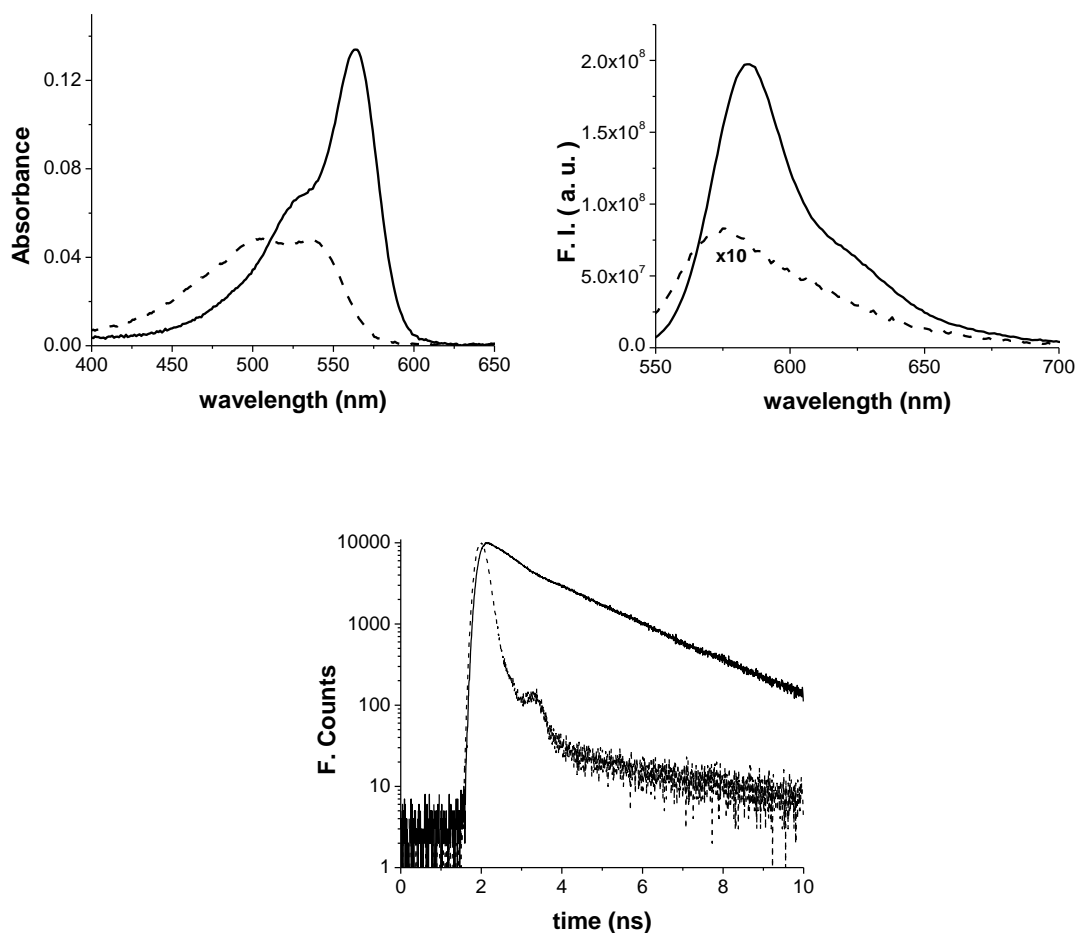


Figure 3.8 Absorption (top left), emission (top right, $\lambda_{ex} = 530 \text{ nm}$) and fluorescence decay curves (bottom, $\lambda_{ex} = 450 \text{ nm}$) of MC540 in aqueous medium (dotted curve) and in presence of $\sim 940 \mu\text{g/mL}$ SiNP (solid curve)

In the presence of SiNP the absorption of the dye gets considerably modified with a peak at 563 nm and a shoulder on the blue side (Fig. 3.8). Further, the emission is red shifted to 583 nm, with intensity increasing by ~ 18 times and the lifetime increasing to 1.5 ns (15 times increase).

These results suggest that there is a strong interaction between the dye and SiNP. This interaction is probably due to electrostatic binding between the oppositely charged species. To get more insight about this binding we have performed a fluorescence titration (intensity & lifetime) of the dye with increasing SiNP concentration, the results of which are described in Fig. 3.9.

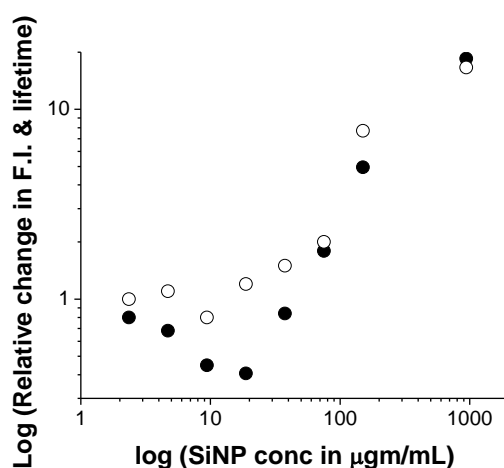


Figure 3.9 Relative integrated emission intensity (solid) and average lifetimes (hollow) of MC540 in presence of varying amounts of SiNP added. The values plotted are normalized to that of the dye in water. The X and Y axes are plotted in a logarithmic scale for clarity.

As shown in the Fig.3.9, the fluorescence intensity of MC540 decreases with increasing concentration of SiNP till a concentration of $\sim 19 \mu\text{g}/\text{mL}$ and increases beyond this concentration. In contrast, the lifetimes with increasing SiNP concentration remains roughly constant ($\sim 0.1 \text{ ns}$, which falls within the instrument response function of the lifetime system) till a SiNP concentration of $\sim 19 \mu\text{g}/\text{mL}$ and increases progressively thereafter. The absorption and emission parameters of the dye in aqueous medium, in the presence of SiNP and in the presence of liposomes (for comparison) are presented in Table 3.3.

Table 3.3 Absorption & fluorescence parameters for MC540 in different environments

System	Absorption (nm)	Emission				
		Peak (nm)	Quantum yield	Average lifetime (ns)	k_r ($\times 10^{-9} \text{ s}^{-1}$)	k_{nr} ($\times 10^{-9} \text{ s}^{-1}$)
MC540/H ₂ O	505/536	570	0.03	0.10	0.30	9.70
Liposome	565	583	0.49	1.6	0.31	0.32
SiNP	563	583	0.53	1.5	0.31	0.28

It can be seen that the fluorescence enhancement of the dye are due to the reduction in the nonradiative rates and are comparable in the presence of SiNP and liposomes. These results suggest a reduction in the photoisomerization rate of MC540 in presence of SiNP that is likely to result due to the restriction on the intramolecular motion of the dye bound at the SiNP surface.

3.3.3 Light induced photostability and phototoxicity of MC540 and its SiNP complex

The photostability of the free dye and dye-SiNP complex in aqueous medium was studied under visible light irradiation for three different light doses by monitoring the change in the absorption spectra and is described in Fig. 3.10.

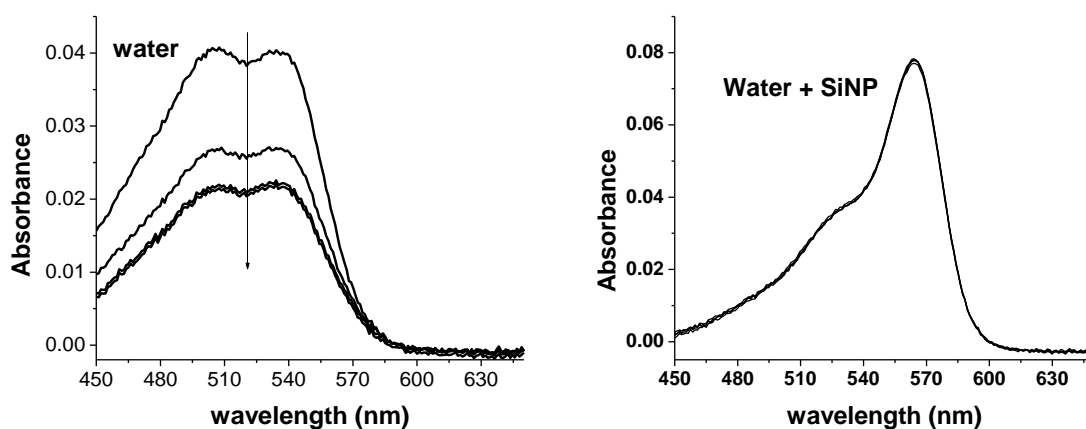


Figure 3.10 Photobleaching of MC540 in aqueous medium in the absence (left) and in the presence of $\sim 940 \mu\text{g}/\text{mL}$ SiNP (bottom). The irradiation conditions are described in the materials & methods section. The arrow in the top panel represents increasing light dose of 0, 1.8, 3.6 and $5.4 \text{ kJ}/\text{m}^2$

At a light dose of $1.8 \text{ kJ}/\text{m}^2$ there is a significant decrease in the absorbance of the free dye ($\sim 37\%$) in aqueous medium and it seems to saturate to $\sim 45\%$ of initial value as the dose is increased to $5.4 \text{ kJ}/\text{m}^2$. This implies that almost half of the dye population has been photodegraded at a light dose of $5.4 \text{ kJ}/\text{m}^2$. In the presence of SiNP there is no change in the absorption spectra of the dye at these light doses which implies that the

photostability of the dye is significantly improved upon binding with SiNP. This is expected from the results presented in Fig. 3.8 which suggest that the binding lowers the photoisomerization rate of the dye bound to the SiNP surface.

Studies on cellular toxicity were carried out using MCF cells. No statistically significant dark toxicity was observed for the dye (upto 10 μM), SiNP (upto 50 $\mu\text{g}/\text{mL}$) and MC540-SiNP complex having a dye concentration of 1-10 μM and SiNP concentration of 10-50 $\mu\text{g}/\text{mL}$. These cells were irradiated, with a MC540 concentration of 1 μM , SiNP concentration of 20 $\mu\text{g}/\text{mL}$, and MC540-SiNP mixture where dye concentration was kept at 1 μM and SiNP at 20 $\mu\text{g}/\text{mL}$. The results of the percentage cell survivals (with respect to control) under irradiation at different light dose for the free dye, SiNP and dye-SiNP complex are given in Table 3.4.

Table 3.4 Light induced toxicity of MC540, SiNP and MC540-SiNP complex against MCF-7 cells^a

System	Concentration of MC540 & SiNP	Light dose 1.8 kJ/m ²	Light dose 3.6 kJ/m ²	Light dose 5.4 kJ/m ²
Only MCF-7 cells	-	100 %	100 %	100 %
Cells + MC540	1 μM	96 \pm 2	93 \pm 3	89 \pm 2
Cells + SiNP	20 $\mu\text{g}/\text{mL}$	92 \pm 3	85 \pm 3	79 \pm 4
Cells + MC540-SiNP	1 μM MC540 & 20 $\mu\text{g}/\text{mL}$ SiNP	71 \pm 3	62 \pm 4	56 \pm 2

^aThe values shown are the mean and standard deviation of three experiments performed. For each set of experiment the control was taken as MCF-7 cells against which the percentage cell survival was obtained.

For free dye, at 1 μM concentration very modest light dose dependent cell killing is observed. For SiNP a slightly higher toxicity is observed. This difference in cell survival for free dye and SiNP is significant to a p value of < 0.017 for a light dose of 5.4 kJ/m². It is unclear at this point why SiNP by itself leads to light induced toxicity. Results of previous studies on the dark toxicity of SiNP are also a bit ambiguous [128, 129]. Luminescent SiNPs (doped with fluorescent dyes, size 50 nm) did not lead to significant toxicity below a concentration of 0.1 mg/mL on human lung epithelial cells [128]. In

another study, it was observed that exposure to SiNP (15 and 46 nm sizes) resulted in a concentration dependent cytotoxicity in cultured human bronchoalveolar carcinoma-derived cells and it was observed to be closely correlated to increased oxidative stress [129].

It is thus essential to study the light induced toxicity of SiNP in greater detail. For the dye-nanoparticle complex the light dose dependent cell killing was observed to be significantly higher compared to that for free dye and SiNP. This is consistent with the expected increase in singlet oxygen yield due to a reduction in the photoisomerization rate.

3.4 Conclusion

The interaction of ANS and TNS with SiNP-V and SiNP-VA in aqueous media was studied by fluorescence spectroscopy. Our results suggest that the binding of these probes with the nanoparticle is due to electrostatic interaction between the negatively charged probes and positively charged 3-amino propyl group. A comparison of the fluorescence properties of these probes bound to nanoparticle and BSA reveals a significant quenching mechanism operative in the nanoparticle environment. The nature of quenching is observed to be probe dependent. Time resolved fluorescence experiments suggests that for TNS quenching is primarily static in nature whereas for ANS the presence of dynamic quenching is suggested. Photophysical studies on interaction of MC540 with SiNP-VA suggest that MC540 binds to SiNP-VA which results in a reduction in the photoisomerization rate of the dye. The light induced toxicity of the dye-nanoparticle complex (tested with MCF cells) is observed to be higher compared to the free dye which is consistent with earlier observations that a reduction in the photoisomerization rate increases the singlet oxygen quantum yield of the dye.

CHAPTER 4

INTERACTION OF CHLORIN P_6 WITH SiNP-VA: PHOTOPHYSICAL AND PHOBIOLOGICAL STUDIES

In this chapter we present the results our investigations on interaction of Chlorin p_6 (Cp_6) with silica nanoparticles having positively charged amino groups (SiNP-VA). The effect of binding between the drug and SiNP-VA on the acid-base ionization equilibrium of Cp_6 is described in detail by studying its absorption and emission properties in aqueous medium. Results of fluorescence correlation spectroscopy and photostability of Cp_6 and Cp_6 -SiNP-VA complex, in the presence of serum are also provided. Finally, we present a comparative study on cellular uptake, intracellular localization and phototoxicity between free Cp_6 and Cp_6 -SiNP-VA complex in cancer cell lines.

Work discussed in this chapter resulted in the following publication:

1. 'Spectroscopic investigations on the binding of the photosensitizer Chlorin p_6 with amine modified silica nanoparticles in aqueous media' B. Jain, A. Uppal, P. K. Gupta and K. Das, *Photochemistry and Photobiology*, Vol. 85, pp. 927-933 (2009).
2. 'Evaluation of photodynamic efficacy of Chlorin p_6 bound to amine modified silica nanoparticles in Colon and Oral cancer cell lines', A. Uppal, B. Jain, M. K. Swami, H. S. Patel, A. Dube, P. K. Gupta and K. Das, In press, *BioNanoScience*.

4.1 Introduction

Cp_6 is one of the chlorophyll-a derivatives. It is amphiphilic in nature and is negatively charged at physiological pH. Previous in vitro and in vivo studies have shown that Cp_6 possess promising photodynamic properties [130]. Studies carried out in our group on breast and colon carcinoma cells have shown that PDT with Cp_6 primarily cause damage to lysosomes and mitochondria depending on the pH of the extracellular medium [131]. In the hamster cheek pouch model, Cp_6 showed preferential accumulation in small tumors (< 5 mm) resulting in complete tumor necrosis and regression after PDT, however, the accumulation of Cp_6 in relatively larger tumor was poor [132].

Recently, the use of NPs for improving delivery of photosensitizer in tumor has received considerable attention due to the fact that compared to small drug molecules, the retention of large size nanoparticles in tumor tissue is more due to the enhanced permeability and retention effect (EPR) [133]. However, conjugation of photosensitizer to nanoparticles can lead to substantial changes in the photophysical and photochemical properties, which can also modulate its photodynamic efficacy/phototoxicity as it is shown in the case of MC540 (chapter 3). Since SiNP-VA contains 3-amino propyl groups which are positively charged at physiological pH (chapter 3), these can be used to electrostatically bind to this negatively charged photosensitizer, Cp_6 .

Cp_6 has three ionizable carboxylic acid groups. Different ionic structures involving protonation-deprotonation of the three carboxylic acid groups of the molecule as a function of pH are depicted in Fig. 4.1. It is pertinent to note that the sequence of the structures shown is only notional. The pH dependent acid-base equilibrium of Cp_6 has been studied by absorption and fluorescence spectroscopy [91]. It has been observed that at physiological pH the dye exists predominantly as negatively charged (i.e. closer to structure D in Fig. 4.1) and as the pH is progressively lowered, successive protonation of the carboxyl groups (forming structures C to A in Fig. 4.1) results in aggregation of the dye in aqueous medium.

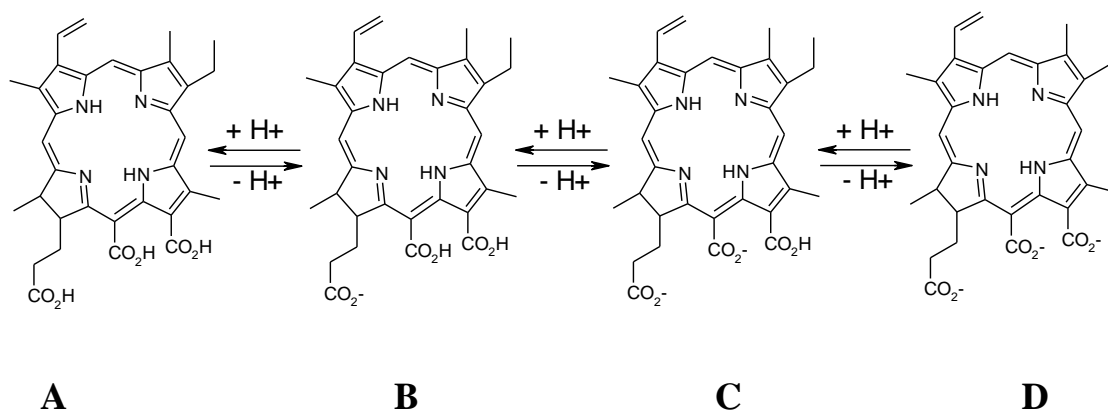


Figure 4.1 Different ionic structures of Cp_6 possible in the pH range of 3-8.

The hydrophobic aggregates have been observed to be nonfluorescent [91]. It has been observed that, by controlling the relative populations of the species A-D, pH plays an important role in the relative binding of the dye with various systems like micelles, liposomes, proteins and biopolymers [91, 134135136137138]. Indeed it was observed that with a decrease in the pH of the incubation medium (from 7.4 to 6.0) the uptake of the dye increased in human colon adenocarcinoma (Colo-205) cells [131]. Further, it has also been observed that the electrostatic binding of the dye with charged surfactants can affect the ionization equilibrium of the dye in aqueous medium [134, 135]. Thus, it is to be expected that electrostatic binding with charged silica nanoparticles (SiNPs) would affect its acid/base ionization equilibrium and thus cellular uptake.

To investigate this aspect, we have studied the acid-base ionization equilibrium of Cp_6 in the presence of SiNP-VA (SiNP) by monitoring the spectroscopic (absorption and fluorescence) properties of the dye. We further investigated the effect of conjugation of Cp_6 with these SiNPs on its cellular uptake, its localization in the cells, photostability and phototoxicity in colon and oral cancer cell lines. We observed that the phototoxicity due to Cp_6 -SiNP complex was higher than free Cp_6 . Possible reasons for this are also addressed.

4.2 Experimental Details

Cp_6 was synthesized in house following the procedure described in reference 5. All the solvents used were spectroscopic grade. SiNP-VA was synthesized as described in chapter 2. The concentration of Cp_6 was fixed at 1 μ M for absorption and emission experiments. The pH of the aqueous medium was varied between 3.0 and 8.0 by adding microliter amounts of 1(N) HCl or NaOH. Experiments were not conducted below pH 3.0 as it resulted in nanoparticle aggregation and not above pH 8.0 to ensure that all the 3-amino propyl groups on the surface of the SiNP-VA (SiNP) remain positively charged to bind the dye. Emission lifetimes of Cp_6 were recorded by excitation at 406 nm using a picosecond diode laser as described in chapter 2 [136].

In order to investigate the relative association of the Cp_6 with serum proteins and SiNP, fluorescence correlation spectroscopy (FCS) experiments were performed in presence of SiNP with varying amounts of serum. The details of the setup are given in chapter 2, section 2.2.2. In all the measurements the SiNP and Cp_6 concentration was kept same (200 μ gm/mL and 10 μ M respectively) and the serum concentration was varied from 2.5-10%. The emission was monitored at 670 nm.

For cellular studies, Colon cancer cells (Colo-205) and human squamous cell (oral) carcinoma cell line Nt8e were obtained from National Centre for Cell Sciences, Pune, India and Advanced Centre for Treatment, Research and Education in Cancer (ACTREC), Mumbai, India respectively. Experimental samples for cellular studies were prepared by Dr. A. Uppal. Briefly, the cells were grown in monolayer at 37°C in humidified incubator (RS Biotech, UK) under 5% CO₂ – 95% air atmosphere. The cells were harvested by trypsinization, re-suspended in culture media and plated in either microplate wells or 35 mm Petri dishes after adjusting the cell number by counting in a haematocytometer.

The cellular uptake of the Cp_6 and Cp_6 -nanoparticle complex was estimated by fluorescence spectroscopy. For this a growth medium containing free Cp_6 or Cp_6 -SiNP

was added to the exponentially growing cells in 35 mm petri dishes and the cells were incubated at 37° C under 5% CO₂ – 95% air atmosphere in dark for 3 hour. Subsequent to incubation, the culture medium containing the photosensitizer or its complex with SiNP was removed and the cell monolayer was washed three times with cold PBS. The cells were harvested by trypsinization, centrifuged at 600 g for 10 minutes and then re-suspended in PBS.

The cellular uptake of the *Cp*₆ was initially measured in the cell suspension and then counter checked in the cell extract also to check for the possible interference of the cellular environment on the fluorescence measurements. For both the measurements, the excitation wavelength was centered at 400 nm (corresponding to the Soret band absorption peak of *Cp*₆) and the fluorescence emission was scanned from 600-750 nm. In case of cell suspension, the relative amount of the *Cp*₆ was estimated from the value of fluorescence intensity at 670 nm (corresponding to the fluorescence maxima of *Cp*₆) after normalization with respect to the cell number. For estimations in the cell extracts, the cell monolayer treated with *Cp*₆ was washed thrice with PBS to remove extracellular *Cp*₆, and then a solution of 0.1 N NaOH and 0.1% SDS was added to lyse the cells. The cell lysate was pipetted several times to give a homogenous solution followed by centrifugation at 600 g for 10 min. The supernatant was mixed with PBS to a final volume of 2.0 ml and used for fluorescence measurements as described above. The cellular uptake of *Cp*₆ was quantified from the relative fluorescence intensity at 670 nm after normalizing with respect to the protein content in the cell extract as measured by Lowry's method [139].

To visualize the intracellular localization of the *Cp*₆, the cells were grown on gelatin coated cover slips and incubated with either free *Cp*₆ or *Cp*₆-SiNP in a growth medium at 37° C in dark for 3 hour. After incubation, the cover slips were washed thrice with cold PBS and then observed under an inverted microscope (Olympus IX70) using fluorescence filter set (excitation 530–560 nm, barrier filter 580 nm). The images were

recorded using a CCD Camera (ProgRes C Fscan) and ProgRes Capture Pro software (Jenoptik, Germany).

For phototoxicity experiments, cells were grown in a 96 well standard microplate and incubated with Cp_6 or Cp_6 -SiNP complex in growth medium for 3 h at 37° C in dark. After incubation, the growth media containing Cp_6 was removed and the monolayer was washed with culture medium containing no serum. Cells were placed in fresh growth medium and then exposed to red light (660 ± 20 nm) using an LC-122A light source (CI TEK, USA) and an optical fiber probe (diameter 1.2 cm, length 1 m) that had an in-built band-pass filter. The optical fiber probe was kept at a height of ~ 14 cm from the microplate to produce an illuminated area of diameter ~ 19 cm. The power density at the level of microplate was ~ 9 mW/cm², as measured by a power sensor 3A-P (Ophir). For homogenous illumination (power variation $<5\%$) of the wells, the microplate was kept in the centre of this area and to ensure that there is no crosstalk between wells, the distance between the two samples was kept at least two rows apart. During irradiation, all the wells were covered with a black paper except the wells to be irradiated. Two separate plates were used for dark control and for light irradiation to avoid light exposure to dark control samples. Phototoxicity was assessed by MTT assay as described in chapter 2, [102]. Percent cell survival in all the samples was calculated with respect to the value obtained in the control sample. All the cell experiments were repeated at least three times and data obtained are presented as average and standard deviation ($n = 3$). The significance of the difference between the treatments was analyzed by student's t test.

To investigate possible photobleaching of the Cp_6 and Cp_6 -nanoparticle complex due to red light irradiation (660 ± 20 nm, 28 mW/cm²), the absorbance spectra of both were recorded at time intervals of one minute over a seven minutes photoirradiation period. The kinetics was followed by monitoring the decrease in the Soret band (400 nm) absorbance of Cp_6 .

4.3 Results

4.3.1 Effect of SiNP on the absorption and emission of Cp_6 from pH 8.0 to 3.0

The absorption and emission properties of Cp_6 are found to dependent on the pH of the aqueous media as shown in Fig. 4.2. As the pH decreases a considerable decrease in the absorption intensities of the Soret and Q band (around 400 and 655 nm respectively at pH 8.0) are observed (Fig. 4.2a). In addition the Q band also shows a blue shift to 642 nm and below pH 5.0, it splits into two bands (640 & 665 nm) with a further decrease in the

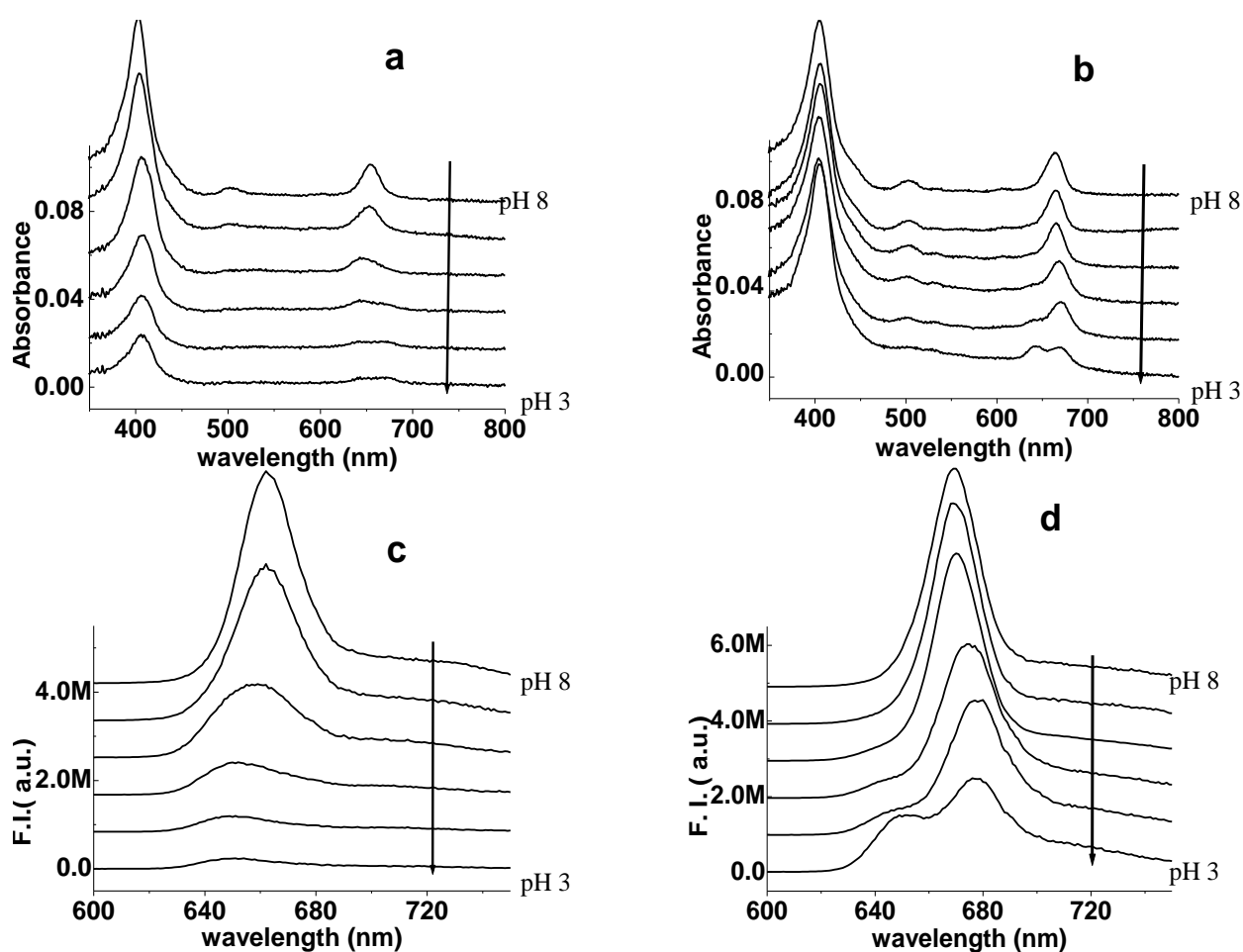


Figure 4.2 Absorption (top b) & emission (bottom d) spectra of Cp_6 in the presence of 940 $\mu\text{g}/\text{mL}$ SiNP at different pH. (The corresponding spectra without SiNP is given in the left side panel a and c) The arrow represents the increase in pH from 3 to 8 in steps of unity. Although the spectra are shown in same Y-axis scale, they are shifted vertically for clarity.

intensity. The emission from the dye (excited at 400 nm) decreases by ~12 times with a progressive blue shift of the band from 662 nm to 650 nm as the pH is lowered from 8.0 to 3.0 (Fig. 4.2c). These observations are consistent with the results of a previous study [91]. In the presence of SiNPs, as described in Fig. 4.2b and d, this pH dependent absorption and emission properties of the dye gets considerably modified. In the absorption spectra, the change in the intensities of the Soret and Q band region is modest, however, a red shift of the latter is observed (from 655 nm to 665 nm). Below pH 5.0, the Q band splits into two bands having maxima at ~670 and ~640 nm respectively. The emission of the dye in the presence of SiNPs is red shifted from 662 nm to 670 nm (at pH 8.0) and decreases to a much lesser extent (~ 1.3 times) as the pH is lowered. In addition it splits into two peaks having maxima at 650 and 678 nm of which the appearance of the latter starts becoming prominent below pH 6.0.

The pH dependent absorption and emission parameters of the dye in the presence and absence of SiNPs are given in Table 4.1 for comparison. In order to gain more insight about how the pH dependent spectroscopic properties of the dye gets modulated in the presence of nanoparticles we have carried out a fluorescence titration of the dye with varying SiNP concentration at pH 8.0, 5.0 and 3.0 was carried out, the results of which are described in the next sections.

Table 4.1 Absorption & emission parameters of Cp_6 at different pH in the presence and absence of SiNP

pH	Absorption maxima (Q-band)		Emission maxima ($\lambda_{ex} = 400$ nm)		Normalized integrated emission intensity ^a	
	No SiNP	SiNP	No SiNP	SiNP	No SiNP	SiNP
8	655	665	662	670	1.00	1.08±0.02
7	652	665	662	670	0.82±0.02	1.09±0.04
6	645	665	660	670	0.51±0.03	1.06±0.04
5	642	668	652	675 ^b	0.23±0.02	0.98±0.03
4	640 & 665	670 & 640	650	678 ^b	0.11±0.03	0.92±0.03
3	640 & 665	668 & 642	650	678 & 650	0.08±0.02	0.84±0.05

^aNormalized with respect to that in water at pH 8.0

^bAlthough two peaks are not prominent, the presence of a shoulder is observed around 650 nm

Fluorescence titration of Cp₆ with SiNP at pH 8.0:

The fluorescence properties of the dye were observed to change significantly with addition of SiNP at pH 8.0 where the tri-anionic form of the dye (species D, Fig. 4.1) is expected to be present. Fig. 4.3 describes the change in the fluorescence properties of the dye with increasing amounts of SiNP added at pH 8.0. Fig. 4.3a shows the fluorescence spectra of the dye for selected SiNP concentrations. Fig. 4.3b shows the normalized integrated emission intensity and average lifetimes of the dye against increasing SiNP concentration. The lifetimes of the dye in the absence and in the presence of maximum amount of SiNP used in this study are also shown in Fig. 4.3a (inset) for comparison. With increasing amounts of SiNP, the fluorescence intensity as well as lifetime of the dye decreases initially and reach to a minimum at a SiNP concentration of 19.0 $\mu\text{g}/\text{mL}$. After that, both fluorescence intensity and lifetime increases steadily with a red shift of the band peak (from 662 nm to 670 nm). Table 4.2 summarizes the emission and lifetime parameters of the dye at various SiNP concentrations at three pHs.

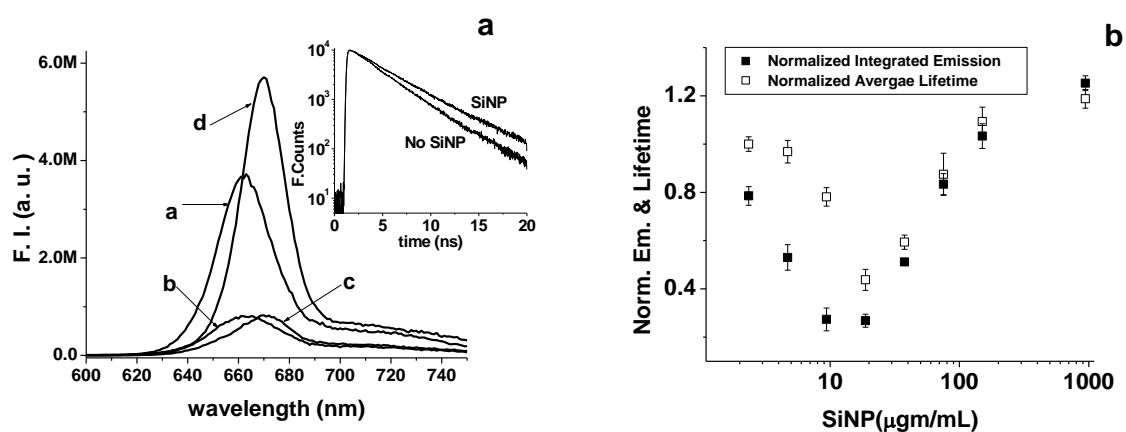


Figure 4.3 (a) Fluorescence titration ($\lambda_{ex} = 400 \text{ nm}$) of Cp₆ with increasing amounts of SiNP at pH 8. a) 0 $\mu\text{g}/\text{mL}$; b) 9.4 $\mu\text{g}/\text{mL}$; c) 18.8 $\mu\text{g}/\text{mL}$ and d) 940 $\mu\text{g}/\text{mL}$ of SiNP. (Inset) Fluorescence decays ($\lambda_{ex} = 406 \text{ nm}$, λ_{em} monitored at $665 \pm 4 \text{ nm}$) of Cp₆ in the presence and absence of 940 $\mu\text{g}/\text{mL}$ of SiNP. (b) Normalized integrated emission and normalized average lifetime of Cp₆ with increasing SiNP. The values are normalized with respect to that of the dye in the absence of SiNP.

Fluorescence titration of Cp_6 with SiNP at pH 5.0.

When the pH of the medium is decreased from 8.0 to 5.0, partial protonation of the carboxyl groups occurred resulting in aggregation of the dye and thereby causing its fluorescence intensity to decrease by ~ 4 times accompanied by a noticeable blue shift of the fluorescence maxima (Table 4.1). Fig. 4.4 describes the effect of the addition of increasing amounts of SiNP on the fluorescence properties of the dye at this pH. Figure 4.4a shows the fluorescence spectra of the dye for selected SiNP concentrations. In Fig. 4.4b, results of fluorescence titration of the dye with SiNP are plotted against the normalized integrated emission intensity and average lifetimes of the dye are shown.

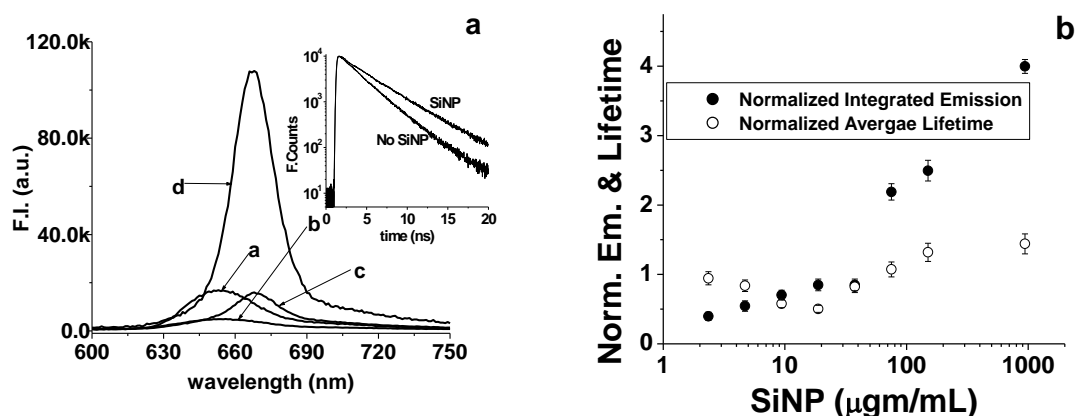


Figure 4.4 (a) Fluorescence titration ($\lambda_{ex} = 400$ nm) of Cp_6 with increasing amounts of SiNP at pH 5.0: a) 0 $\mu\text{g}/\text{mL}$; b) 9.4 $\mu\text{g}/\text{mL}$; c) 18.8 $\mu\text{g}/\text{mL}$ and d) 940 $\mu\text{g}/\text{mL}$ of SiNP. (Inset) Fluorescence decays ($\lambda_{ex} = 406$ nm) of Cp_6 in the presence (monitored at 675 ± 4 nm) and absence (monitored at 650 ± 4 nm) of 940 $\mu\text{g}/\text{mL}$ of SiNP at pH 5.0. (b) Normalized integrated emission and normalized average lifetime of Cp_6 with increasing SiNP at pH 5.0. The values are normalized with respect to that of the dye in the absence of SiNP. The X-axis is represented in the log scale for clarity.

Unlike pH 8.0, the normalized integrated fluorescence intensity does not have a steep minimum over the concentration ranges of SiNP used because the minimum occurs as soon as SiNPs are added (2.35 $\mu\text{g}/\text{mL}$). After that the fluorescence intensity increases steadily with a 23 nm red shift of the band (from 652 nm to 675 nm observed at a SiNP concentration of 37.6 $\mu\text{g}/\text{mL}$). The average lifetime have a minimum around SiNP

concentration of $\sim 19.0 \mu\text{g}/\text{mL}$ and then increases steadily. The emission and lifetime of the dye at various SiNP concentrations at this pH are summarized in Table 4.2.

Fluorescence titration of Cp_6 with SiNP at pH 3.0:

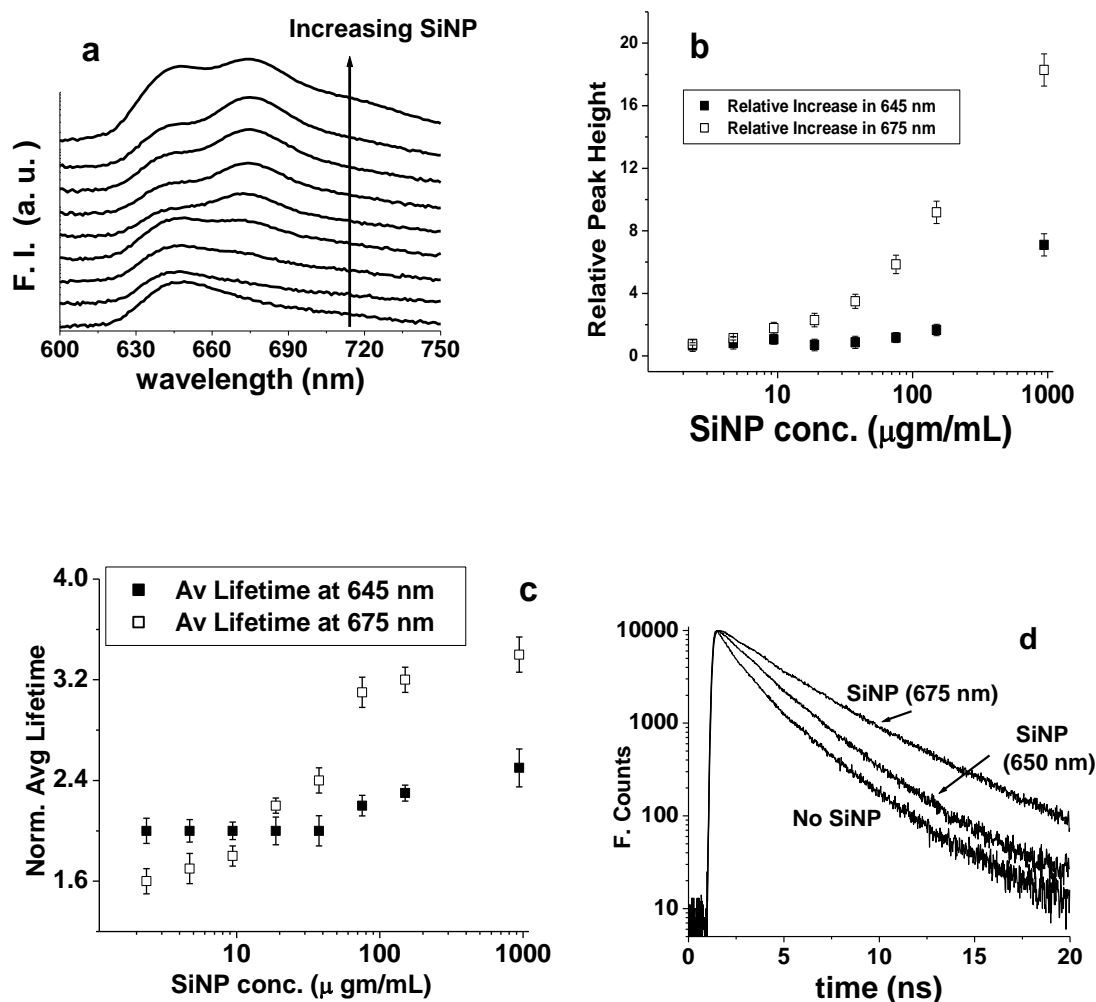


Figure 4.5 (a) Fluorescence titration ($\lambda_{\text{ex}} = 400 \text{ nm}$) of Cp_6 with increasing amounts of SiNP at pH 3.0. The arrows represent increasing SiNP concentration (from 0 to $940 \mu\text{g}/\text{mL}$). The spectra are shifted vertically for clarity. (b) Relative change in the fluorescence intensity ($\lambda_{\text{ex}} = 400 \text{ nm}$) of the dye monitored at 650 and at 675 nm upon addition of SiNP. The values plotted are normalized relative to that in pH 3.0 solution. (c) Relative change in the fluorescence lifetime ($\lambda_{\text{ex}} = 406 \text{ nm}$) of the dye monitored at 650 and at 675 nm upon addition of SiNP. The values plotted are normalized relative to that in pH 3.0 solution. (d) Fluorescence decays ($\lambda_{\text{ex}} = 406 \text{ nm}$) of Cp_6 in the presence (monitored at $678 \pm 4 \text{ nm}$ & $650 \pm 4 \text{ nm}$) and in absence (monitored at $650 \pm 4 \text{ nm}$) of $940 \mu\text{g}/\text{mL}$ of SiNP at pH 3.0.

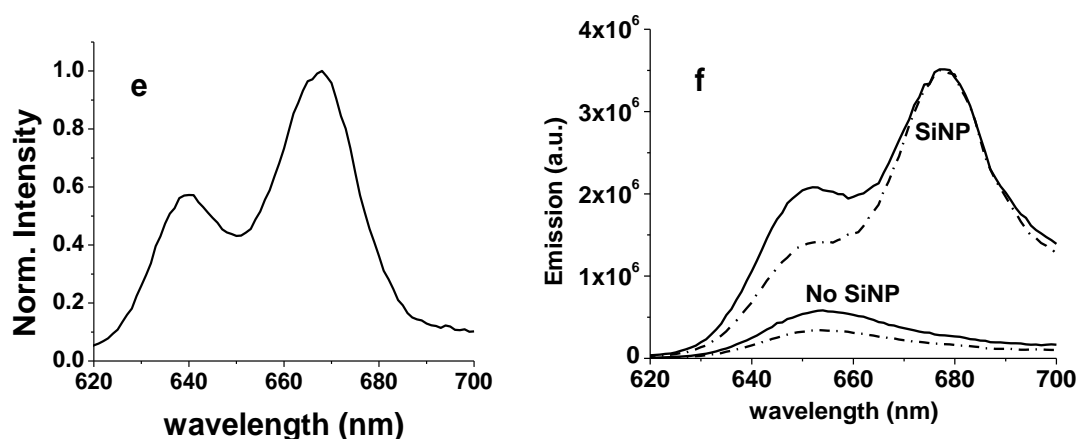


Figure 4.5 (e) Synchronous fluorescence spectra of Cp_6 in the Q -band region in the presence of $940 \mu\text{g}/\text{mL}$ of SiNP at pH 3.0 (offset between excitation & emission = 10 nm). (f) Effect of 0.9 (M) acrylamide on the fluorescence of Cp_6 ($\lambda_{ex} = 400 \text{ nm}$) in the presence and absence of SiNP ($940 \mu\text{g}/\text{mL}$). Dashed lines denote the fluorescence in presence of the quencher.

When the pH of the medium is further decreased to 3.0 causing further protonation of the carboxyl groups, enhanced aggregation accompanied by a significant quenching (~ 12 times) of the dye's fluorescence takes place without SiNPs as shown in Table 4.1. At this pH the fluorescence properties of the dye are observed to change differently with addition of SiNP than that observed at pH 8.0 and 5.0. Fig. 4.5a shows how the fluorescence of the dye changes with increasing amounts of SiNP. The fluorescence of the dye shows dual emission centered at 650 and 678 nm, the intensity of the latter increases progressively with the SiNP. A plot of the peak intensities and lifetimes monitored at 650 and 678 nm is shown in Fig. 4.5b & c. It is clear from these figures that the emission intensities and lifetimes at 650 nm do not change very much (except near the highest SiNP concentration), whereas they change significantly when monitored at 678 nm. The lifetimes of the dye at various SiNP concentrations at this pH are given in Table 4.2. Fig. 4.5d shows the variation in the lifetime of the dye (monitored at 650 and 675 nm) in the presence and absence of maximum amount of SiNP. In order to ascertain the origin of the two emission bands at this pH, a synchronous fluorescence scan of the dye was performed in the presence of maximum amount of SiNP.

Table 4.2 Relative integrated emission intensity and average lifetimes of Cp_6 with various amount of SiNP at pH 8.0, 5.0 and 3.0^a

SiNP ($\mu\text{g}/\text{mL}$)	pH 8.0		pH 5.0		pH 3.0 ^c	
	Integrated emission	^b Average lifetime at 665 nm	Integrated emission	^b Average lifetime at 675 nm	^b Average lifetime at 650 nm	^b Average lifetime at 675 nm
0	1	3.2±0.2	1	2.7±0.3	2.0±0.2	- d-
2.35	0.79±0.04	3.2±0.2	0.40±0.06	2.6±0.2	2.0±0.1	1.6±0.1
4.7	0.53±0.05	3.0±0.1	0.54±0.07	2.3±0.1	2.0±0.3	1.7±0.1
9.4	0.27±0.05	2.2±0.2	0.70±0.07	1.6±0.2	2.0±0.1	1.8±0.2
18.8	0.27±0.03	1.1±0.1	0.85±0.08	1.4±0.1	2.0±0.2	2.2±0.1
37.6	0.51±0.01	1.8±0.3	0.85±0.08	2.2±0.3	2.0±0.1	2.4±0.3
75.2	0.83±0.04	2.9±0.1	2.19±0.11	2.9±0.4	2.2±0.3	3.1±0.2
150.4	1.03±0.05	3.5±0.2	2.50±0.15	3.6±0.2	2.3±0.2	3.2±0.1
940	1.25±0.03	3.9±0.4	4.00±0.10	3.8±0.3	2.5±0.4	3.5±0.1

^aFor each pH, the integrated emission intensities are normalized against the zero SiNP

^bThe lifetimes of the dye in most cases can be fit satisfactorily with two exponentials; however for some cases a three exponential fit is required. All the lifetimes (given in nanoseconds) reported here are average lifetimes. For pH 5.0, in the absence of SiNP, the average lifetime was monitored at 650 nm.

^cFor pH 3.0, only the lifetimes are given. ^dNot measured.

Observation of two peaks at ~645 and ~670 nm in Fig. 4.5e suggests the possibility of two species of the dye being present at this pH in the presence of SiNP. To investigate this aspect further, we studied the effect of a quencher, acrylamide, on the dye's fluorescence in the presence and absence of SiNP. The results are presented in Fig. 4.5f. A 40 % quenching of the dye's fluorescence was observed at an acrylamide concentration of 0.9 M indicating that the dye in aqueous environment is accessible to the quencher. However, in the presence of SiNP, only the fluorescence band centered at 650 nm showed significant quenching implying that the species emitting at this wavelength is accessible to the quencher and therefore is most likely to be the free dye present in the aqueous environment.

In order to check whether Cp_6 remain associated with SiNP in cellular medium, the relative association of the Cp_6 with serum proteins and SiNP was investigated, as

serum forms a major component of cell culture, by performing FCS experiments with varying amounts of serum at pH 7.4.

4.3.2 FCS studies of the free Cp_6 and Cp_6 -SiNP complex

The results of the FCS experiments are shown in Fig. 4.6.

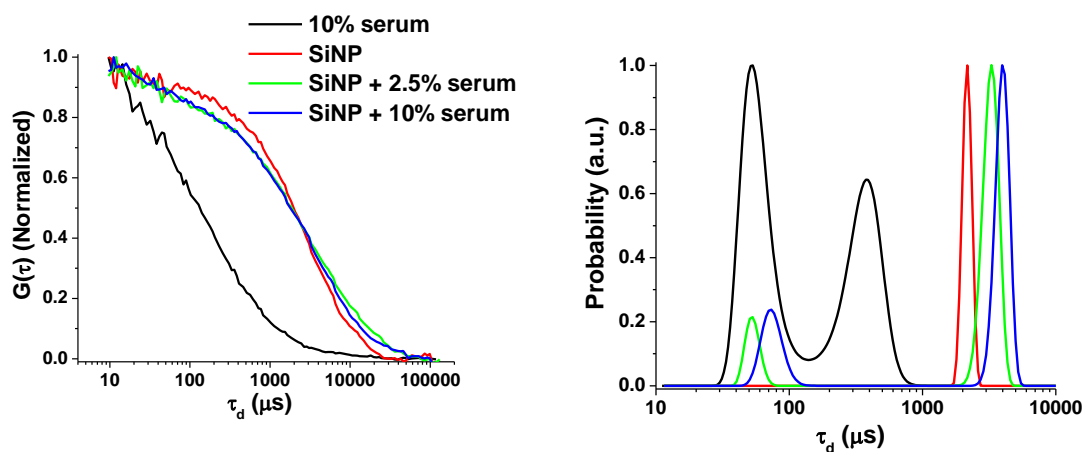


Figure 4.6 Autocorrelation traces (left) and their fits (right) of $10 \mu\text{M}$ Cp_6 in various environments.

The left panel describes the autocorrelation traces of the Cp_6 in presence of only SiNP, only 10% serum and two different mixtures of SiNP and serum where SiNP concentration is kept constant ($200 \mu\text{g}/\text{mL}$) and the serum concentration was kept as 2.5 and 10%. The corresponding fits to the traces are shown in the right panel of Fig. 4.6. Three typical diffusion times are obtained from the fits which may be attributed to the free Cp_6 (40-70 μsec), Cp_6 bound to serum (380 μsec) and Cp_6 bound to SiNP (2000-4000 μsec). The figure shows significantly higher probability of Cp_6 bound to SiNP even in the presence of serum proteins at all the concentrations used in the experiment and even at 10% serum concentration which is similar to that used for the uptake and toxicity experiments.

4.3.3 Intracellular uptake, localization and phototoxicity of free Cp_6 and its SiNP complex

Intracellular uptake: The results of the fluorescence measurements on intracellular uptake of Cp_6 and its SiNP complex in Colo-205 and NT8e cells at two different concentrations (5 and 10 μM of Cp_6 alone and its complex with 100 and 200 $\mu\text{g}/\text{ml}$ SiNP, respectively at pH 7.4) are shown in Fig. 4.7a & b. The Cp_6 fluorescence was measured in intact cells as well as in cell extracts prepared in detergent solution for the estimation of relative amount of free and bound Cp_6 in cells. The incubation time was fixed as 3 h. The results in Fig. 4.7 & b show that at both the concentrations, there are no significant difference in relative amount of free Cp_6 and its SiNP complex in the cells at 3 h incubation.

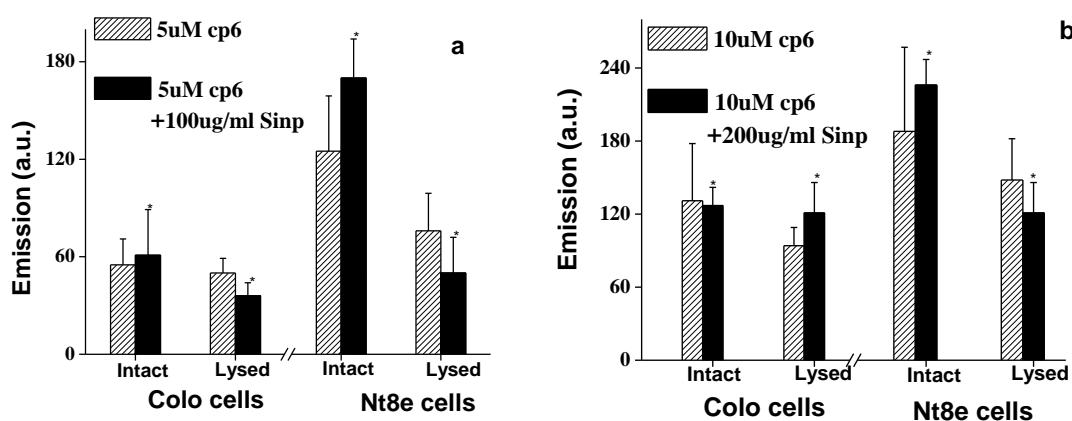


Figure 4.7 Data showing cellular uptake of Cp_6 as relative fluorescence intensity in intact cells and after extraction in SDS:NaOH solution for Colo-205 and Nt8e cells. The cells were incubated with Cp_6 or Cp_6 -SiNP at (a) 5 μM Cp_6 and its complex with SiNP at 100 $\mu\text{g}/\text{ml}$ and (b) 10 μM Cp_6 and its complex with SiNP at 200 $\mu\text{g}/\text{ml}$. Data are average \pm standard deviation of values obtained from three independent experiments. * - Significant ($p < 0.01$).

Intracellular localization : The fluorescence images of the Colo-205 and NT8e cells taken after 3 hour incubation with free Cp_6 and Cp_6 bound to SiNP are shown in Fig. 4.8. In Colo-205 cells the fluorescence from both free (Fig 4.8a) and SiNP bound Cp_6 (Fig

4.8b) can be seen to localize mainly in the cytoplasm. In case of NT8e cells also, the intracellular localization of free Cp_6 and Cp_6 -SiNP complex was similar (Fig 4.8 c & d).

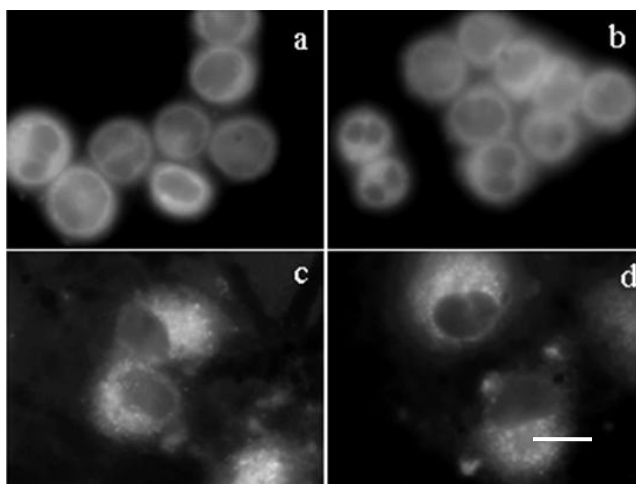


Figure 4.8 Fluorescence microphotographs of Colo-205 cells (a, b) and Nt8e cells (c-d) showing intracellular localization of Cp_6 (a, c) and Cp_6 -SiNP (b, d). Magnification, 100 X, Bar- 25 μ m.

Cytotoxicity: The effect of free Cp_6 and its SiNP complex after 3 h incubation on survival of Colo-205 and NT8e cells, kept in dark and after exposure to red light, is shown in Fig. 4.9a & b. The data are compared with respect to the cell survival of a control sample that received no Cp_6 and no light. It was observed that Cp_6 alone (5 μ M and 10 μ M) in dark led to 10-15% cytotoxicity indicating slight dark toxic effect. In comparison, Cp_6 -SiNP complex alone, at lower concentration (5 μ M Cp_6 and 100 μ g/ml SiNP), almost the same level of dark toxicity was shown (Fig. 4.9a) whereas upon exposure to red light the phototoxicity was found to increase by ~20-25% (Fig. 4.9a). However, no significant difference is observed in phototoxicity induced by Cp_6 -SiNP and free Cp_6 at this lower concentration ($p > 0.05$). At higher concentrations, Cp_6 -SiNP conjugate (10 μ M Cp_6 and 200 μ g/ml SiNP) in dark led to considerable increased cytotoxicity, by ~30-35 % (Fig. 4.9b). This toxicity is mainly due to SiNP since the addition of SiNP alone (200 μ g/ml) also led to enhanced cytotoxicity to the same level in both the cell lines (Fig. 4.9b).

Upon exposure to red light, the cells treated with higher concentrations of Cp_6 -SiNP, showed increase in phototoxicity by ~85% which was nearly double than the increase in phototoxicity (~40%) induced by 10 μM Cp_6 and light. SiNPs alone in the presence of light showed no significant change in cytotoxicity as compared to SiNP in dark suggesting that SiNP did not contribute to the phototoxicity.

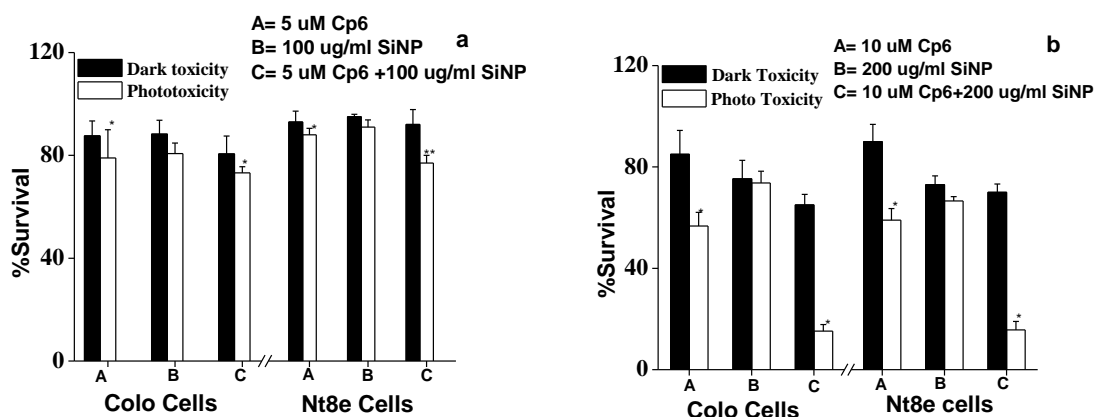


Figure 4.9 Data showing changes in percent cell survival following photosensitizer treatment in dark and after exposure to light for Colo-205 and Nt8e cells. The cells were incubated with Cp_6 or Cp_6 -SiNP at two different concentrations. (a) 5 μM Cp_6 and its complex with SiNP at 100 $\mu g/ml$ and (b) 10 μM Cp_6 and its complex with SiNP at 200 $\mu g/ml$. Data are average \pm standard deviation of values obtained from three independent experiments. * - Significant ($p < 0.01$).

4.3.4 Relative photo-stability of the free Cp_6 and Cp_6 -SiNP complex

The photostability of the Cp_6 and its complex with nanoparticles was monitored by measuring the changes in Soret band absorbance of the free Cp_6 and its SiNP complex after exposure to red light. These experiments were done in aqueous as well as serum (10%) media since the latter environment is more relevant with respect to this work. The plot of change in absorbance (in log scale) of the Cp_6 vs. irradiation time is shown in Fig. 4.10. For all cases a linear decrease in absorbance with increase in irradiation time was observed. In aqueous medium both with and without serum, the photostability of the Cp_6 increased significantly when SiNP were present.

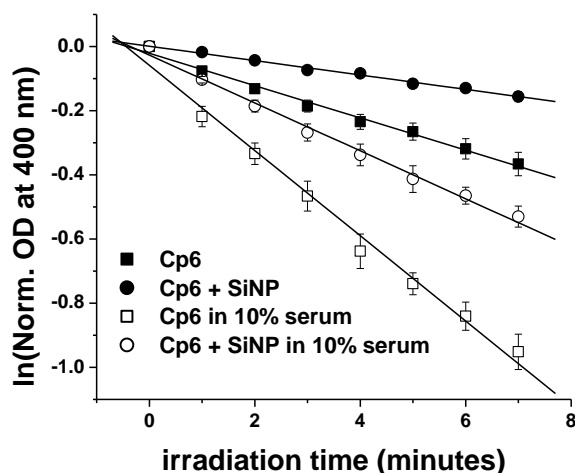


Figure 4.10 Photobleaching of $10 \mu\text{M}$ Cp_6 under irradiation at $660 \pm 20 \text{ nm}$. The kinetics was followed by monitoring the decrease in the optical density (OD) of the Soret band of the Cp_6 . ($\text{SiNP} = 200 \mu\text{g}/\text{mL}$)

4.4 Discussion

A decrease in pH causes successive protonation of the carboxylic groups of Cp_6 , which results in the formation of hydrophobic species corresponding to structures C-A in Fig. 4.1 [91]. The aggregation of these hydrophobic species in aqueous medium results in a progressive decrease in the absorbance and fluorescence intensities of the dye. The pH dependent spectroscopic property of the dye in aqueous medium is shown in Fig. 4.2a and c. In the presence of SiNP, this pH dependent spectroscopic property of the dye in aqueous medium is observed to alter significantly (Fig. 4.2b and d & Table 4.1). As the pH is lowered, the change in the intensity of the Soret and Q band is modest as compared to the change in the absence of SiNP (Fig. 4.2). However, it is accompanied by a gradual red shift at Q band. The Q band splits into two bands below pH 5.0. The emission of the dye also decreases to a much lesser extent (~ 1.3 times compared to ~ 12 times in the absence of SiNPs) and is accompanied by a noticeable red shift of the band maxima. In emission there is an appearance of a second band ($\sim 650 \text{ nm}$) as the pH is lowered (below 6.0), which gets prominent as the pH is lowered further and is clearly visible at pH 3.0. In

short till pH 5.0, the absorption and emission properties of the dye in the presence of SiNPs remain more or less unchanged (except the red shift) and below that the Q band and emission splits into two. These observations indicate that SiNPs are affecting the pH dependent acid-base equilibrium of the dye.

The observed changes may be due to the binding between the dye and nanoparticle which may arise due to both electrostatic and hydrophobic interaction. Electrostatic binding is possible at higher pH due to the presence of positively charged 3-amino propyl groups at the surface of the SiNPs and negatively charged carboxyl groups of Cp_6 . However, at low pH, hydrophobic binding between the dye (species A-C) and nanoparticle is also a possibility because the interior of these SiNPs are reported to be hydrophobic in nature [45].

At pH 8.0, where the trianionic form of the dye (species D, Fig. 4.1) is the most abundant, electrostatic binding between the dye and SiNP is expected. With the addition of increasing amounts of SiNP the fluorescence intensity and lifetime of the dye passes through a minimum at a SiNP concentration of 19.0 $\mu\text{g}/\text{mL}$ (Fig. 4.3 and Table 4.2). The occurrence of a minima can be explained by the fact that when dye:SiNP ratio is larger (i.e. at low SiNP concentration since concentration of the dye is fixed at 1 μM) the intermolecular separation between the dye molecules bound to the SiNP becomes sufficiently small. This induces self quenching of the fluorescence as there is a considerable overlap between the Q-band absorption and emission. It may be noted that similar behavior was observed earlier in the presence of positively charged surfactant CTAB and liposomes [134, 135, 136]. After that both intensity and lifetime increases steadily and at a SiNP concentration of 940 $\mu\text{g}/\text{mL}$ the absorption (Q band) and emission of the dye is red shifted by ~ 10 nm accompanied by a modest increase (1.25 times) in emission intensity and lifetime (1.2 times) at this pH (Table 4.1 & 4.2). The observed changes in the fluorescence intensity and lifetime of the dye at different SiNP concentrations suggest a strong electrostatic binding between the dye and SiNP at pH 8.0.

At pH 5.0, due to the partial protonation of the carboxylic acid groups, species like A-C will start to form aggregates, which will decrease the absorption and emission of the dye as noted earlier. The observed trend of the dye's fluorescence with increasing amount of SiNP at this pH is quite similar to those observed at pH 8.0 with the exception that here the minima of fluorescence intensity and lifetime occurs at different SiNP concentrations (Fig. 4.4 and Table 4.2). At a SiNP concentration of 940 $\mu\text{g}/\text{mL}$ the absorption (Q band) and emission of the dye is red shifted by ~ 25 nm accompanied by a 4 times enhancement in emission intensity and 1.4 times enhancement in the lifetime (Table 4.1 & 4.2). The magnitude of the changes observed at this pH is larger than that observed at pH 8.0. We also note from Table 4.1 & 4.2 that the spectroscopic properties like Q and emission band maxima and the lifetime of the dye in the presence of SiNP are quite similar at pH 5.0 and 8.0. These observations suggest that at pH 5.0 and 8.0, the species of the dye that are involved in the binding with SiNP is most likely to be the tri-anionic species (D) of the dye. It may be noted that a similar kind of behavior was observed in earlier studies where the binding of the dye with Cremophor EL at pH 5.0 and pH 7.0 was monitored by fluorescence spectroscopy [138]. The more hydrophilic species of the dye (species D) was observed to get bound preferentially with the hydrophobic Cremophor EL at pH 5.0, which was explained by a hindrance to the protonation of Cp_6 trianionic species caused by Cremophor EL.

At pH 3.0, the absorption and emission of the dye is much weaker because the hydrophobic species are in abundance due to the protonation of the carboxyl groups. However, the aggregation of the dye at this pH is significantly altered in the presence of SiNPs although the observed trend of the dye's fluorescence with increasing amount of SiNP at pH 3.0 is quite different to those observed at pH 5.0 or 8.0. At this pH the Q band of absorption and the emission spectra are clearly split into two bands (Fig. 4.2d & 4.5a). The presence of two peaks at ~ 645 and ~ 670 nm in the synchronous fluorescence spectra of the dye (Fig. 4.5e) suggests that there are two species of the dye at pH 3.0 in

the presence of SiNP. While the species responsible for fluorescence at 645 nm band is seen to be insensitive to SiNP concentration, the species responsible for fluorescence at 670 nm band is sensitive to changes in SiNP concentration (Fig. 4.5 b-d) and its spectroscopic parameters are similar to that observed at pH 5.0 & 8.0 which implies that it is most likely originating from the trianionic form of the dye (species D, Fig. 4.1) bound to SiNP.

The species responsible for fluorescence at 650 nm (with a lifetime of 2.0 ns) could either be due to free dye or dye bound to SiNP. To test this we have studied the effect of a quencher, acrylamide on the dyes fluorescence at this pH in the presence of SiNP. At pH 8.0 and 5.0, we have observed that acrylamide is only effective in quenching the fluorescence of the dye in the absence of SiNP (data not shown). The significant quenching of the fluorescence peak at 650 nm by acrylamide (Fig. 4.5f) suggests that the species emitting at 650 nm is coming from the free dye i.e. not bound to SiNP. The increase in emission intensity and lifetime of the 650 nm peak when approaching highest SiNP concentration as observed in Fig. 4.5a-d is most likely due to the contribution coming from the 678 nm emission. Although the binding between the dye and nanoparticle still remains at pH 3.0, the strength or amount of binding is obviously reduced as compared to pH 8.0 and 5.0 because a significant fluorescence from the unbound dye still persists at this pH. It seems that at this pH the strength of the hydrophobic attraction between the partially protonated species (A-C) competes with that of the electrostatic force of attraction between the negatively charged species (D) and the positively charged SiNP.

These spectroscopic studies show that conjugation of SiNP with Cp_6 modifies the pH dependent equilibrium of the Cp_6 . Therefore the PDT efficacy may also get affected as cellular uptake has been shown to be pH dependent [131]. For cellular uptake studies the cells were incubated in growth medium which contains serum proteins. It has been shown earlier that Cp_6 has affinity to bind to the hydrophobic sites of serum proteins

[140]. Therefore, in the growth medium, Cp_6 of the Cp_6 -SiNP conjugate has probability to competitively bind to protein or remain bound to the SiNP. The hydrodynamic radii of the free Cp_6 and its complexes with the serum proteins or nanoparticles will be different. As FCS measures hydrodynamic radii of the fluorescent particles and can give a quantitative estimation about the relative association of the Cp_6 with serum proteins and nanoparticles, the relative association of Cp_6 with SiNP and serum proteins was investigated by performing FCS experiments in presence of SiNP with varying amounts of serum. The fitting of the autocorrelation curves against Cp_6 -SiNP conjugates in the presence of 10% serum (Fig. 4.6) show two components with probability ratio 20 and 100 corresponding to free and SiNP bound Cp_6 respectively. Thus, results of FCS experiments indicate that the majority of the Cp_6 remains bound to SiNP even in the presence of serum proteins. As similar concentration of serum proteins are found in the cells also, the results suggest that the majority of the Cp_6 remains bound to SiNP even in cells when these cells were incubated with the Cp_6 -NP conjugates.

The cellular uptake and phototoxicity of free Cp_6 and Cp_6 -SiNP complex were examined in Colo-205 and Nt8e cells. Since the local cellular environment can interfere with the fluorescence yield of the photosensitizer and thus with the estimation of its relative amount, we measured the Cp_6 fluorescence in intact cells as well as in cell extracts prepared in detergent solution. The 3h incubation time was fixed on the basis of a time dependent analysis which showed that while the uptake of Cp_6 increases linearly up to 3 h and then saturates, for Cp_6 -SiNP the uptake was found to decrease beyond 3 h possibly because of an increase in dark toxic effect of Cp_6 -SiNP at later time points (data not shown).

The results of cellular uptake showed no difference in the relative amount of Cp_6 localized in the cells when it is given as free form or as SiNP complex (Fig. 4.7 a & b). Cellular microscopy studies (Fig.4.8) done in the Colo-205 and NT8e cells lines showed the presence of punctuate pattern of Cp_6 fluorescence in the cytoplasm. However,

the intracellular localization pattern of Cp_6 -SiNP in both the cell lines was similar to free Cp_6 . Interestingly, while lower concentration of Cp_6 -SiNP showed no significant difference in the phototoxic effect as compared to Cp_6 , for higher concentrations (10 μ M Cp_6 and 200 μ g/ml SiNP) the phototoxicity induced by Cp_6 -SiNP was much higher than free Cp_6 (Fig. 4.9a & b). There was however, considerable dark toxicity due to SiNP alone which also contributed to the dark toxicity of Cp_6 -SiNP at higher concentration. SiNP alone has been shown to induce cytotoxicity via induction of oxidative stress in human bronchoalveolar carcinoma-derived cells [129]. Whether such effect can contribute to the observed cytotoxicity of SiNP in Colo-205 and Nt8e cells is presently not clear. However, SiNPs alone in the presence of light showed no significant change in cytotoxicity as compared to SiNP in dark suggesting that SiNP did not contribute to the phototoxicity.

We also measured the photostability of free Cp_6 and Cp_6 -SiNP in serum media which is expected to significantly influence its photodynamic efficacy [141]. In aqueous medium, both with and without serum, the photostability of Cp_6 -SiNP was found to be higher than the free Cp_6 (Fig. 4.10). The improved photostability of the Cp_6 in the presence of SiNP in serum media is consistent with the results obtained from FCS experiments. Thus, due to the lower rate of photobleaching of Cp_6 -SiNP complex, the concentration of the active photosensitizer during the treatment is expected to be higher and this appears to be the main reason for the observed increase in phototoxicity of Cp_6 -SiNP complex.

4.5 Conclusion

Our experimental results demonstrate that the pH dependent acid-base equilibrium of Cp_6 in aqueous medium is affected in the presence of SiNP. In the absence of SiNP, the lowering of pH enhances the formation of partially/fully protonated species (Fig. 4.1, A-C) which are hydrophobic in nature and thus form nonfluorescent aggregates. However,

in the presence of SiNPs, these partially or fully protonated species of the dye get bound to SiNP by electrostatic force of attraction. The spectroscopic signature of the dye that is bound to SiNP at pH 5.0 is very similar to that at pH 8.0 and it is suggested that the tri-anionic form of the dye remains bound to the positively charged SiNP at these pH. The presence of electrostatic binding force was observed even at pH 3.0 which competes with intermolecular hydrophobic forces and as a consequence the formation of hydrophobic aggregates at this pH is disrupted significantly. Thus, pH is observed to play a significant role in controlling the binding between the dye and nanoparticle. The formation of a stable dye-nanoparticle complex around physiological pH is expected to affect the relative uptake and photodynamic efficacy of the free dye and the dye-nanoparticle complex in cancer cells. This was investigated using colon and oral carcinoma cell lines. Our study showed that the complex of Cp_6 with SiNPs produced higher phototoxic effect on both the cells as compared to free Cp_6 . The intracellular uptake and localization of the free Cp_6 and Cp_6 -SiNP complex showed no difference. However, the preferential binding of Cp_6 with SiNP in serum media was confirmed by FCS experiments which could result in an improvement of its photostability. This is suggested as the main reason for the observed increase in the phototoxicity of Cp_6 -SiNP. Thus, Cp_6 -SiNP was shown to provide better photodynamic efficacy as compared to free Cp_6 . It is also expected that SiNP bound Cp_6 would accumulate better in tumors due to EPR effect. At present, one major concern in use this formulation is toxic effect of SiNPs when used at higher concentrations. It is expected that covalent attachment of Cp_6 to SiNP should help reduce the required concentration of SiNP for more efficient drug delivery. Therefore, further investigations in cell culture using covalently coupled Cp_6 -SiNP are necessary to prove the potential advantage of such formulation.

CHAPTER 5

SPECTROSCOPIC INVESTIGATION OF CONVERSION OF PURPURIN 18 TO CHLORIN P_6 IN THE PRESENCE OF SILICA, LIPOSOME & POLYMERIC NPs

In this chapter we present the results of our study on effect of NP environment on the conversion of entrapped purpurin 18 (PP18) to its hydrolytic product Chlorin p_6 (Cp_6). The time dependent absorption and emission of the PP18 entrapped in four NPs: SiNP-V, SiNP-VA, PLGA NP and liposomes: suspended in buffer at physiological pH, in the presence and absence of serum, was investigated up to 24 hrs to study its conversion to Cp_6 . The results are presented in this chapter.

Work discussed in this chapter resulted in the following publication:

1. 'Conversion of purpurin 18 to chlorin p_6 in the presence of silica, liposome and polymeric nanoparticles: A spectroscopic study' B. Jain, A. Uppal, K. Das, A. Dube and P. K. Gupta, *Journal of Molecular Structure*, Vol. 1060, pp. 24–29 (2014).

5.1 Introduction

Photodynamic therapy (PDT) has gained considerable clinical acceptance in various countries for the treatment of cancer [142,143]. The selective accumulation of a photosensitizer in tumor is an important factor in the effectiveness of photodynamic therapy. It is believed that tumor selectivity depends on the hydrophobic character of the photosensitizer since this enables its better uptake in cells via interaction with low density lipoproteins and the cellular membrane [144,145]. However, the hydrophobic photosensitizers generally tend to aggregate in aqueous medium that can result in poor uptake in cells. The ability of nanoparticles (NPs) to carry hydrophobic photosensitizers has attracted tremendous interest for their use in PDT of cancer. Different types of nanoparticles are being currently explored for the delivery of such drugs [12, 146, 147, 148, 149]. For drug delivery it is required that the NPs are biocompatible, stable in physiological conditions and able to carry the drug without any chemical alteration [31]. Among these, organically modified silica nanoparticles (SiNPs) prepared using triethoxyvinylsilane and/or 3-aminopropyl triethoxysilane have shown to satisfy these features [45, 50, 51, 150]. Due to the presence of a hydrophobic core, these NPs can be loaded with hydrophobic drugs and since the surface is charged these can be easily solubilized in aqueous medium [31, 45, 50, 51, 150, 11-15, 151]. Such NPs have been used for gene delivery, entrapping dyes/probes for imaging, and hydrophobic photosensitizers for PDT, etc. [124].

Earlier, it has been reported that purpurin 18 (PP18), a hydrophobic chlorophyll derivative, can be incorporated in liposomes and the formulation was found to deliver the photosensitizer successfully in human colon cancer cells [152]. PP18 shows promising optical properties for use in PDT such as an absorption band at ~ 695 nm with extinction coefficient $\sim 41,800 \text{ M}^{-1} \text{ cm}^{-1}$ (in acetone). However, since PP18 contains an anhydride ring in the molecule, it undergoes rapid hydrolysis at physiological pH (shown in Figure 5.1) which results in the formation of chlorin p_6 (Cp_6), a water soluble photosensitizer,

having Q band absorption blue shifted to ~ 656 nm with decreased extinction coefficient ($\sim 24,800 \text{ M}^{-1}\text{cm}^{-1}$).

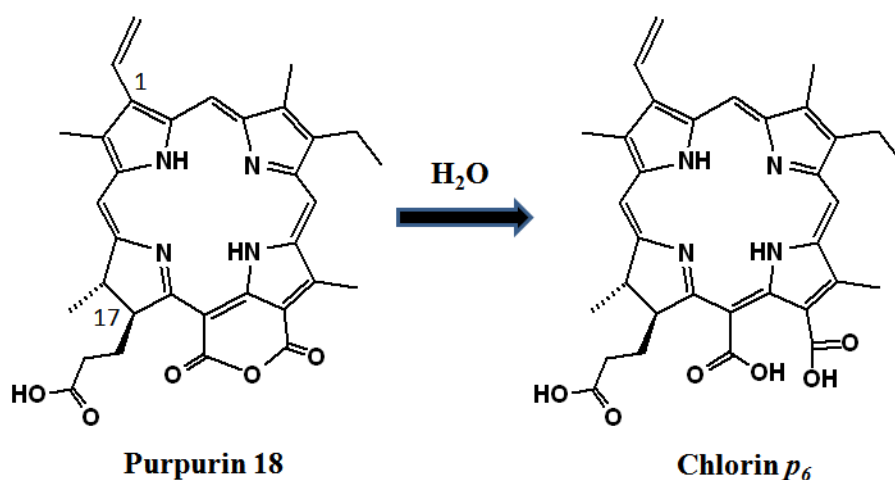


Figure 5.1 Chemical structure of PP18 and Cp_6 and the conversion of PP18 to Cp_6 , due to its hydrolysis in the presence of water.

Although it was possible to stabilize PP18 in liposomes prepared at lower pH (6.0) and thus deliver PP18 in cells [152], during incubation for time periods beyond 1 h significant conversion of PP18 into Cp_6 was observed [152]. Other carriers such as Cremophor EL and Poly L lactic acid nanofibers have also been used to carry PP18 [138, 153]. Recently, Droget et al reported synthesis of a stable and water soluble PP18 in which the anhydride ring is chemically modified into cycloimide and the carboxylic group at '17' carbon position (IUPAC system) is attached to polyethylenimine, a water soluble polycationic molecule [154]. However, the singlet oxygen yield of this derivative was substantially compromised (~ 4 times lower) as compared to PP18.

In this chapter we investigated spectroscopically the suitability of SiNPs as carriers of PP18 in comparison with liposomes and polymeric NPs, which are the conventionally used drug carriers. This was studied by monitoring the stability of PP18 against its conversion to its hydrolytic product Cp_6 in aqueous buffer (at physiological pH). To mimic biological environment, the same study was done in the presence of 10%

serum (as it forms the major part of a biological system). The conversion was monitored by measuring the absorption and fluorescence of the drug in the four NP systems at various time intervals, over the period of 24 hours.

5.2 Experimental details

Sample preparation

All the reagents used in the experiment were of spectroscopic grade. SiNP-V, SiNP-VA, polymeric NP and Liposomes were synthesized as described in chapter 2. Fetal bovine serum (FBS) from Himedia, Mumbai, India was used as received. Purpurin 18 was prepared from dry spinach leaves following the procedure reported in ref.155 and the stock was prepared in acetone. The size of the PLGA NP and liposomes was ~ 30 nm and the zeta potential was ~ -8 ± 2 mV, -41 ± 4 mV respectively.

Absorption and Fluorescence spectroscopy

Absorption and fluorescence spectra were recorded as described in chapter 2. All the experiments were performed at pH 7.4 in 10 mM Phosphate–citrate buffer and the concentration of PP-18 added to various preparations was 2 μ M unless otherwise specified. The ratio of NP to drug was maintained similar in the experiments. For time dependent studies, the absorption/emission of PP-18 added to SiNP-V, SiNP-VA, polymeric NP and liposome suspended in buffer and buffer containing 10 % serum was monitored at several time intervals up to 24 hours. The time point immediately after the addition of PP18 in the NP suspension was taken as $t=0$ and thereafter the spectra were taken at 1, 2, 4, 6, 8, and 24 hrs. Absorption and fluorescence spectra were recorded as described in chapter 2. All the experiments were performed at pH 7.4 in 10 mM Phosphate–citrate buffer and the concentration of PP-18 added to various preparations was 2 μ M unless otherwise specified. The ratio of NP to drug was maintained similar in the experiments. For time dependent studies, the absorption/emission of PP-18 added to

SiNP-V, SiNP-VA, polymeric NP and liposome suspended in buffer and buffer containing 10 % serum was monitored at several time intervals up to 24 hours. The time point immediately after the addition of PP18 in the NP suspension was taken as $t=0$ and thereafter the spectra were taken at 1, 2, 4, 6, 8, and 24 hrs.

5.3 Results and Discussion

First we present the spectroscopic properties of the two drugs in different environments without NPs. Figure 5.2 shows the absorption and fluorescence spectra of PP18 and Cp_6 in three environments: hydrophobic (acetone), hydrophilic (buffer) and buffer containing serum.

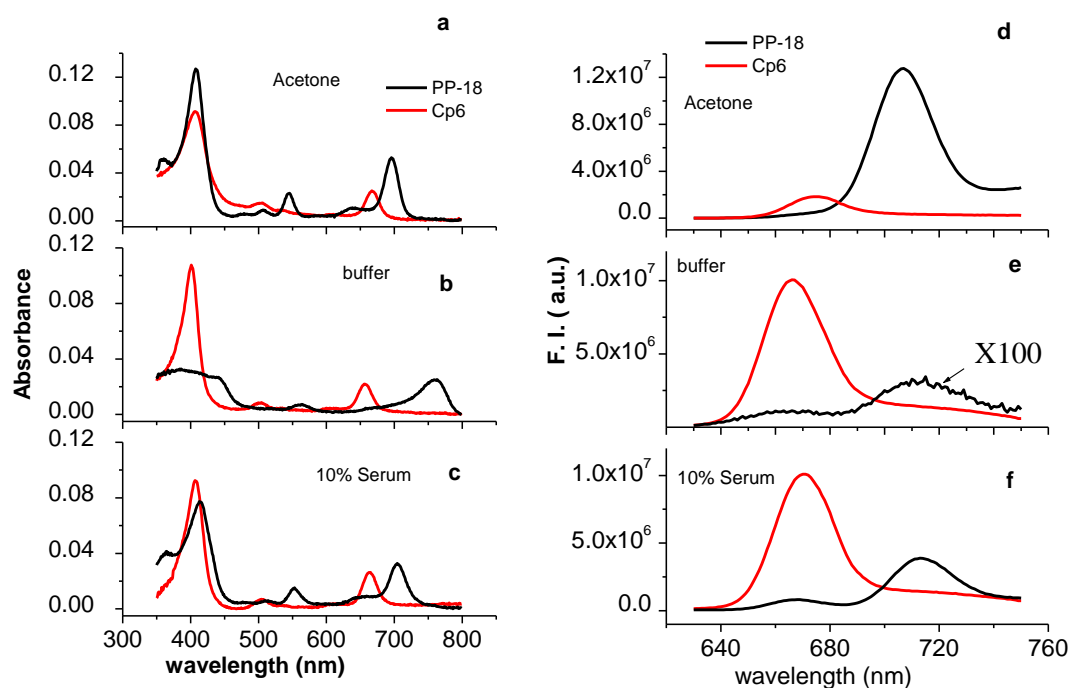


Figure 5.2 Absorbance and fluorescence spectra of PP18 (black) in acetone, buffer and serum at pH 7.4. The spectra for Cp_6 (red) are also shown for comparison. The concentration of dyes is $1 \mu M$.

In all the three environments, as shown in Fig. 5.2 a-c, while the Q band absorption peaks of the two molecules lie at different positions, their Soret band overlap at ~ 405 nm. Thus,

for emission spectroscopy, these were excited at 405 nm. In acetone (Fig. 5.2 a), the Q band absorption peak for PP18 and Cp_6 lies at 695 nm and 663 nm respectively, whereas the fluorescence is centered at ~ 710 and ~ 670 nm respectively (Fig. 5.2 d). Both, the absorption and emission peak of PP18 are sharp as well as intense indicating it to be in monomeric form. However, in buffer, shown in Fig. 5.2b, the absorption peaks of PP18 are considerably reduced and broadened with respect to that in acetone with the appearance of an additional peak at 760 nm. This indicates its aggregation [152], which is also seen in the emission spectra (Fig. 5.2 e, PP18 intensity is multiplied by a factor of 100 for comparison) where the intensity is reduced by \sim three orders of magnitude when compared to that in acetone. In the presence of serum, shown in Fig. 5.2 c, the spectral features are intermediate, as compared to acetone or buffer. The aggregate peak disappears whereas monomer peak at 702 nm appears and the Soret band is sharpened with respect to buffer. The emission intensity also increases but is significantly less as compared to that in acetone (Fig. 5.2 f). This indicates that in serum there is an equilibrium between the monomers and the aggregates of PP18. Cp_6 on the other hand, (shown as red curves in Fig. 5.2) owing to the presence of three negatively charged carboxyl groups at physiological pH, is readily soluble in buffer showing sharp absorption and emission peaks [156]. Cp_6 and PP18 show different spectroscopic signatures in the 600-750 nm region. The Q band absorption peak of PP18 monomer is at 702 nm and that for Cp_6 is at ~ 655 nm. The emission band of PP18 is located at ~ 712 nm whereas for Cp_6 it is at ~ 670 nm [152]. Therefore, in this study, the conversion of PP18 to Cp_6 was investigated by monitoring both absorption and emission in the 600-750 nm region in the four NP systems, suspended in buffer as well as in serum.

Conversion of PP18 to Cp_6 in aqueous buffer in the presence of different NPs.

Figure 5.3 shows the absorption and fluorescence spectra of PP18, taken at different time interval, in all the four NPs in the buffer medium. For clarity only two spectra, taken at 0

and 24 hrs, are shown. Spectra taken at all other time points are shown in supporting information Fig. 5.7. In all the nanoparticulate systems, immediately after the addition of PP18, i.e., at time $t=0$, two prominent bands around 405 and 702 nm due to monomer are observed. Also, there is a peak at ~ 760 nm due to aggregates, which is significantly higher in SiNP-V as compared to SiNP-VA and PLGA NP (where it is seen as a small hump) however in liposome it is not visible.

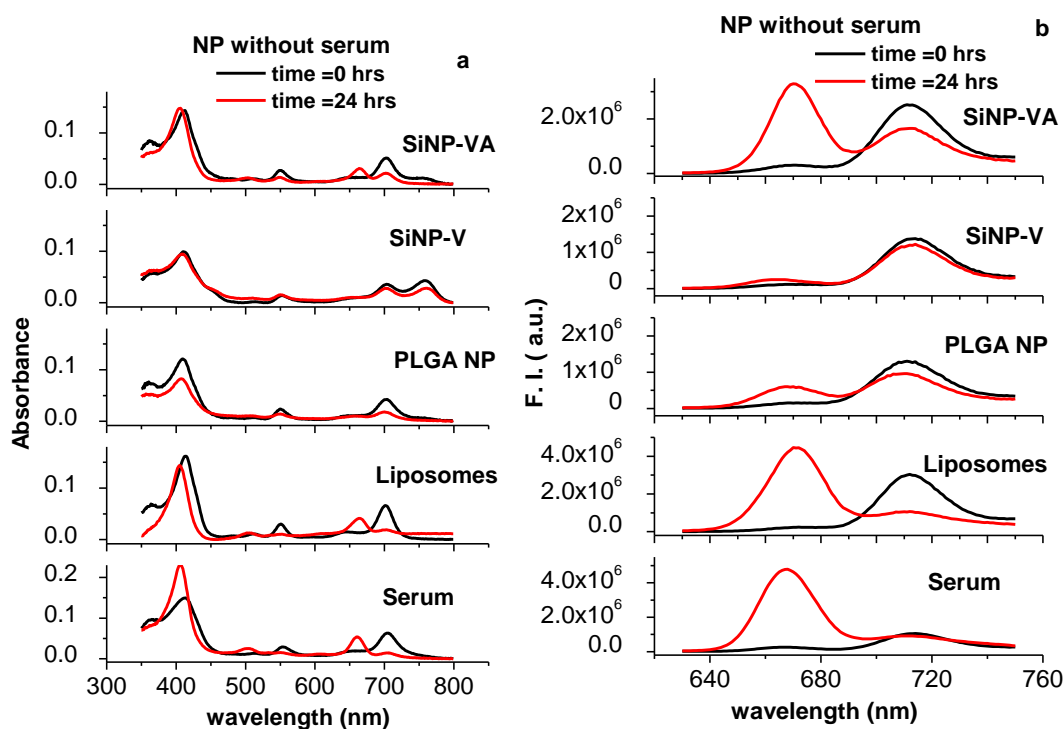


Figure 5.3 The absorption (a) and fluorescence (b) spectra of PP18 in SiNP-VA, SiNP-V, PLGA NP and liposome suspended in neat buffer at pH 7.4, monitored immediately after adding PP18 time $t=0$ (black) and after 24 hours (red). The spectra in 10% serum are also given for reference.

With the increase in time, the peak intensity due to aggregates decreases in all systems whereas the monomer peak (at 702 nm) first increases and then decreases (Supporting information Fig.5.7). Simultaneously, another peak appears at 655 nm due to the formation of Cp_6 , which is prominently seen in SNP-VA, liposomes and serum. This suggests that the aggregates of PP18 are getting dissociated with time (Supporting

information Fig.5.7), monomers are being formed which are also getting hydrolyzed to Cp_6 . It is to be noted that in SiNP-V the aggregate peak remains significantly high and does not vanish even after 24 hours. This suggests that aggregates are still attached to SiNP-V and their dissociation with time is a very slow process.

The corresponding time dependent fluorescence of PP18 in these particulate systems was also monitored up to 24 hours. The fluorescence spectra at time 0 hrs and 24 hrs are shown in Fig. 5.3b. Spectra taken at all other time points are shown in supporting information Fig.5.8. The spectra also show, in general, two peaks centered at 712 nm and 670 nm corresponding to PP18 and Cp_6 fluorescence.

With increase in time, PP18 intensity decreases and Cp_6 increases. From the Fig. 5.3 it is clear that the time dependent changes in intensities of these bands are different in all the four NPs. The change is largest in liposomes and SiNP-VA and smallest in SiNP-V. For comparison, the spectra of PP18 in buffer containing only serum is also shown which also shows large decrease in PP18 intensity.

Conversion of PP18 to Cp_6 in aqueous buffer containing 10% serum in the presence of different NPs.

To mimic the physiological condition the conversion was also monitored in the presence of 10% serum as it is a major constituent of blood and mammalian cell culture medium. Figure 5.4 shows the absorption and emission spectra of PP18, taken at time 0 and 24 hrs in the presence of all the four NPs suspended in buffer containing serum. Spectra taken at all other time points are shown in supporting information Fig.5.9 and Fig.5.10 respectively. In all the NP systems the decrease of absorption peak at 702 nm and increase in the intensity at 655 nm is faster in the presence of serum (Fig. 5.4a) as compared to neat buffer (Fig. 5.3a). In SiNP-V while the 760 nm peak (at t=0) disappears in few hrs, the peak at 702 nm is clearly seen even after 24 hrs whereas in the other NPs the 702 nm peak is not visible after 24 hrs. The emission spectra at time 0 hrs and 24 hrs

(corresponding to the absorption spectra described above) are shown in Fig. 5.4b. Compared to neat buffer (Fig. 5.3b), in the presence of serum, the increase in the intensity at 670 nm is higher in all NP systems.

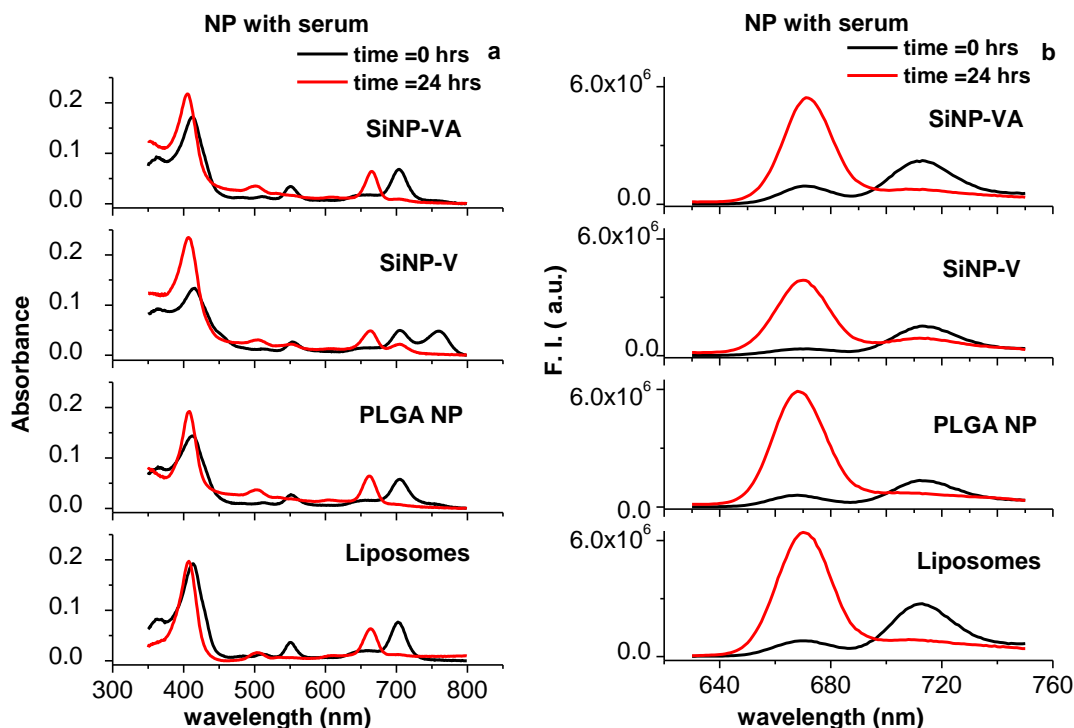


Figure 5.4 The absorption (a) and fluorescence (b) spectra of PP18 in SiNP-VA, SiNP-V, PLGA NP and liposome suspended in buffer at pH 7.4 in presence of 10% serum, monitored immediately after adding PP18 time $t=0$ (black) and after 24 hours (red).

The relative change in the fluorescence intensities at 670 nm and at 712 nm, corresponding to Cp_6 and PP18 monomer concentration in different NP systems, is plotted as a function of time and is shown in Figs. 5.5 and 5.6 respectively. It is clear from Fig. 5.5a that the intensity of Cp_6 is least for SiNP-V and polymeric NPs while it is highest for SiNP-VA and liposomes (~ 10 times compared to SiNP-V). Also the normalized fluorescence intensity of PP18 up to 24 hrs, in Fig. 5.6a shows a fast decrease in liposome ($\sim 75\%$) whereas in SiNP-V the intensity is almost constant over the period

of time (less than 15% decrease). This suggests that SiNP-V protect the drug from the environmental perturbations better as compared to liposome.

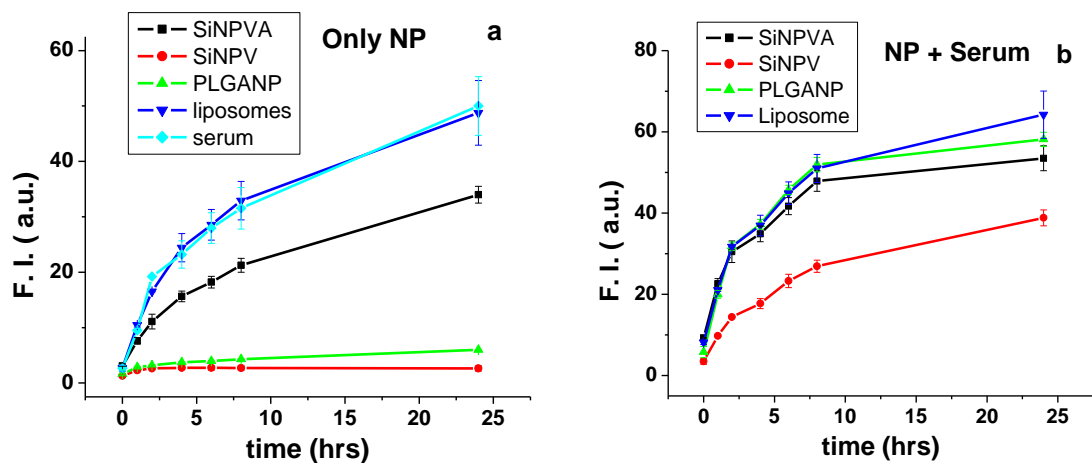


Figure 5.5 The plot of fluorescence intensity at 670 nm (corresponding to Cp_6 emission), in all four NPs suspended in buffer at pH 7.4, as a function of time in the absence of serum (a) and in the presence of 10% serum (b).

When the buffer medium is replaced with serum medium (Figs. 5.4 and 5.5b), the conversion to Cp_6 increases in all NP systems however the increase is significantly different among the particles.

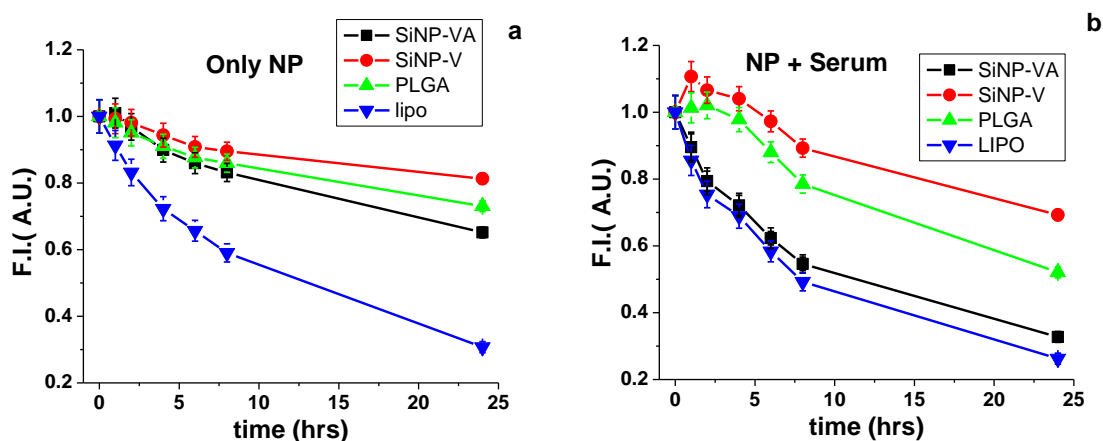


Figure 5.6 The plot of normalized fluorescence intensity, at 712 nm (corresponding to PP18 emission) in all four NPs suspended in buffer at pH 7.4, as a function of time, in the absence of serum (a) and in the presence of 10% serum (b).

While in the presence of liposome and SiNP-VA the conversion is increased by ~1.5 times, in the presence of SiNP-V and polymeric NPs this conversion increases by about 10-14 times as compared to that without serum (Fig. 5.5a). Still the absolute intensity of Cp_6 in the serum media is least in SiNP-V among all the four NPs and PP18 highest as shown in Fig. 5.6b.

From the results presented so far, in the presence of NPs, the time dependent changes in the PP18 absorption (at 702 nm) as well as fluorescence (at 712 nm, shown in Fig. 5.3b) spectra are modulated by the two effects, namely, dissolution of PP18 aggregates into monomers as well as monomer conversion to Cp_6 . This can be represented as follows:



The relative changes in PP18 fluorescence will depend upon rate of dissolution of PP18 aggregates and rate of conversion of PP18 to Cp_6 . As a result the changes in PP18 fluorescence are not expected to correlate to that of Cp_6 . Therefore, to get an idea about the conversion of PP18 to Cp_6 by fluorescence technique, the changes in Cp_6 fluorescence only might be considered.

The reason of increase in the conversion to Cp_6 in the presence of serum, as shown in Fig. 5.4 might be due to two factors. 1) The presence of hydrophobic pockets in the serum proteins solubilizes PP18 as monomer as seen in Figs. 5.2c and f [157]. Particularly in case of SiNP-V, in the presence of serum, a fast decrease in the aggregate peak is observed, as shown in the absorption spectra (Fig. 5.4a and S5.3). In Fig. 5.6b an initial increase in PP18 monomer peak in SiNP-V also supports the fast monomerization of PP18 aggregates. 2) Proteins contain amino groups which can catalyze the hydrolysis of the anhydride ring by working as base.

To compare among the two SiNPs, the conversion of PP18 to Cp_6 is significantly large in SiNP-VA as compared to SiNP-V (Fig. 5.5a). Although the two SiNPs are similar, there

are additional amino groups present on the surface of SiNP-VA (due to the additional silica precursor, APTS, used in the synthesis having 3-amino propyl group) [151]. At physiological pH ~2.5% of these amino groups are still neutral (as pK_a of amino groups is ~9) which therefore can act as base and thus catalyze the hydrolysis of the anhydride ring. This can be attributed to the enhanced conversion of PP18 to Cp_6 in SiNP-VA.

The conversion is larger in liposomes as compared to SiNP-VA. The reason is not clear, however it might be speculated that the polar head group of the lipid molecule in liposome might facilitate the hydrolysis of the monomeric PP18 sitting in the lipid bilayer.

5.4 Conclusion

In this chapter, the suitability of SiNPs as carrier of hydrophobic photosensitizer PP18 was investigated spectroscopically by comparing the stability of PP18 against its conversion to its hydrolytic product Cp_6 in four NP systems. The absorption and fluorescence of PP18 entrapped in NP formulations such as SiNP-V, SiNP-VA, PLGA NPs and PC liposome suspended in aqueous environment at pH 7.4 (buffer as well as in serum), monitored over the period of 24 hrs, was found to depend on the NP environment. The conversion was found to be lowest in SiNP-V and highest in liposome. The difference in the conversion is suggested to be the presence of the groups, which were able to catalyze the hydrolysis of the anhydride ring. Our results also suggest that SiNP-V could be used as carrier of PP18.

Supporting Information:

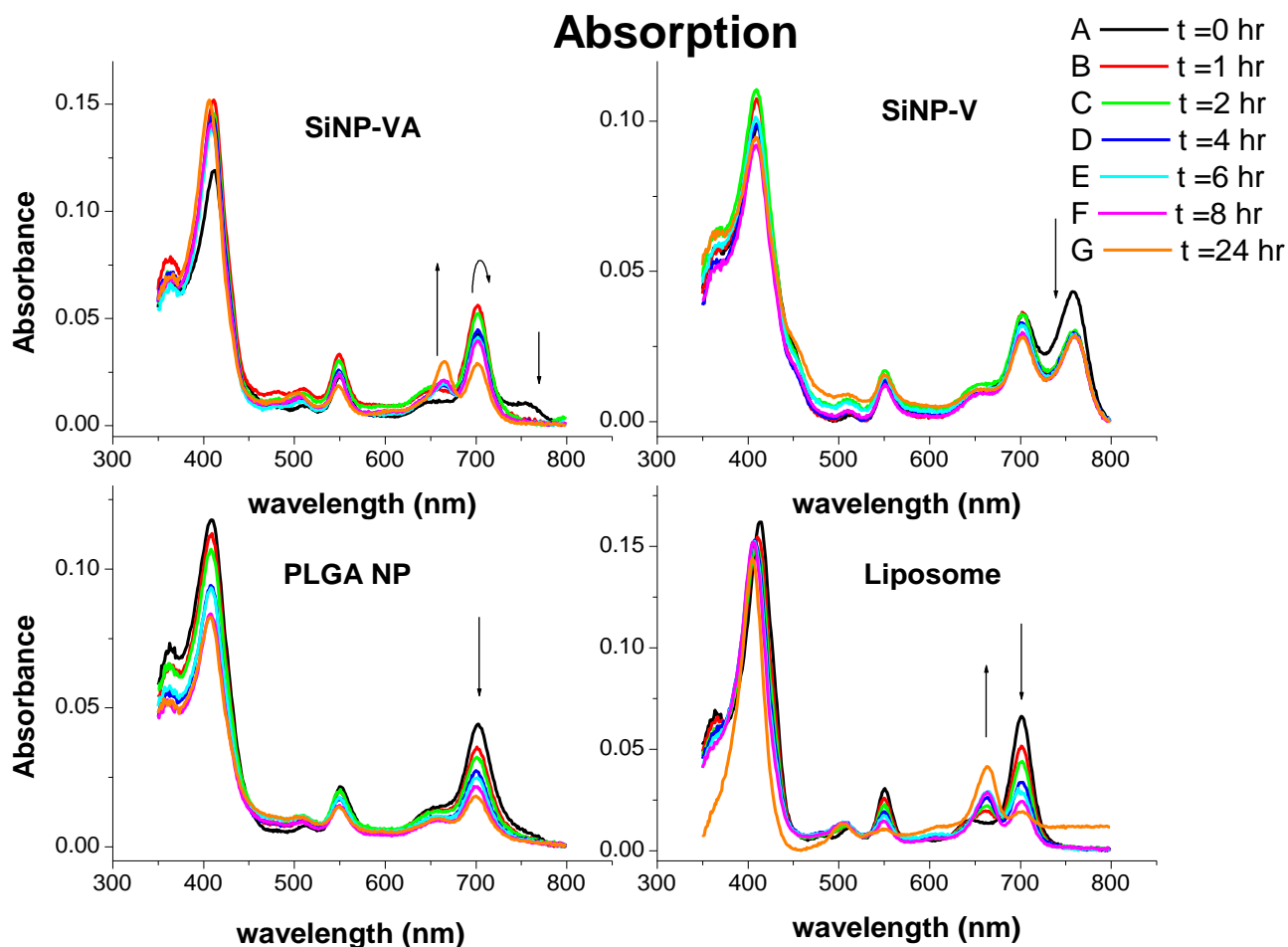


Figure 5.7 Time dependent absorption spectra of PP18 in SiNP-VA, SiNP-V, PLGA NP and liposome at pH 7.4. These are monitored, immediately after adding PP18, i.e., at time $t=0$, after 1, 2, 3, 5, 8, and 24 hours (shown as A, B, C, D, E, F, and G respectively). Arrows show the increase and decrease in the peak intensity at 655 nm, 702 nm and 760 nm corresponding to Cp₆ monomer and PP18 monomer and aggregate absorption respectively.

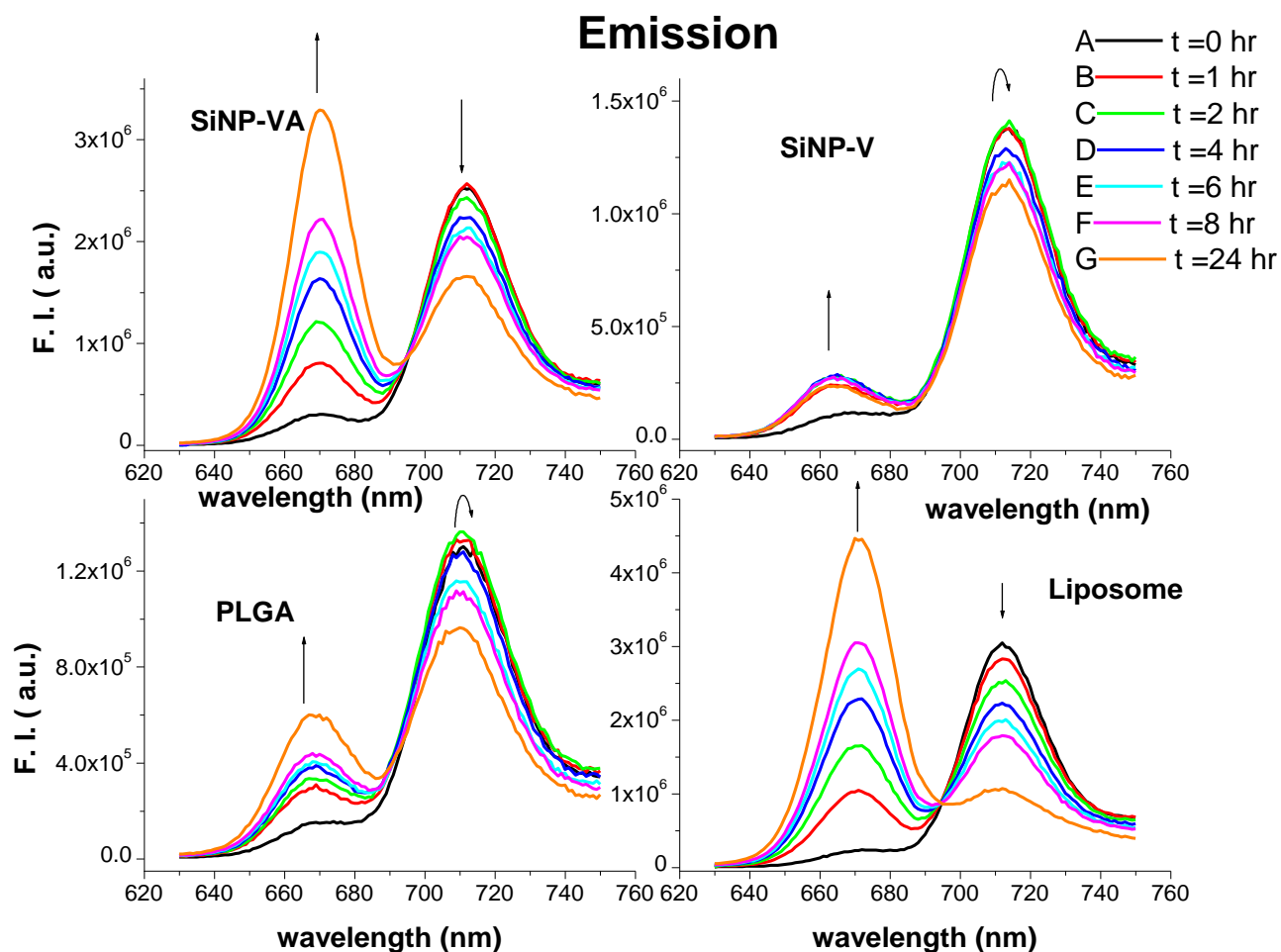


Figure 5.8 Time dependent fluorescence spectra of PP18 in SiNP-VA, SiNP-V, PLGA NP and liposome at pH 7.4. These are monitored immediately after adding PP18 (time $t=0$), after 1, 2, 3, 5, 8, and 24 hour (shown as A, B, C, D, E, F, and G respectively). Arrows show the increase and decrease in the peak intensity at 670 nm and 712 nm corresponding to Cp_6 and PP18 emission peak respectively.

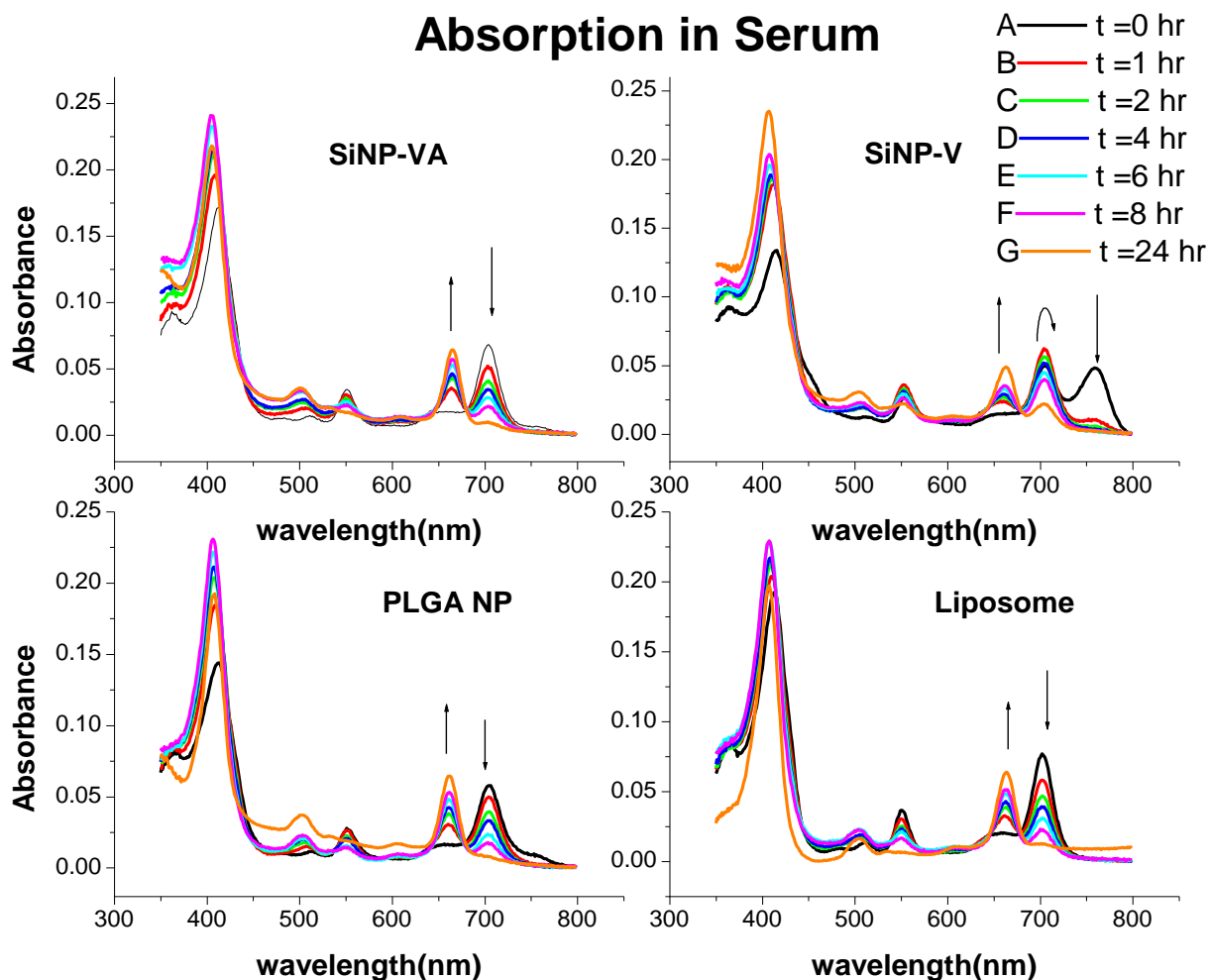


Figure 5.9 Time dependent absorption spectra of PP18 in SiNP-VA, SiNP-V, PLGA NP and liposome suspended in 10% serum at pH 7.4. These are monitored immediately after adding PP18 (time $t=0$), after 1, 2, 3, 5, 8, and 24 hours (shown as A, B, C, D, E, F, and G respectively). Arrows show the increase and decrease in the peak intensity at 655 nm, 702 nm and 760 nm corresponding to Cp_6 monomer and PP18 monomer and aggregate absorption respectively.

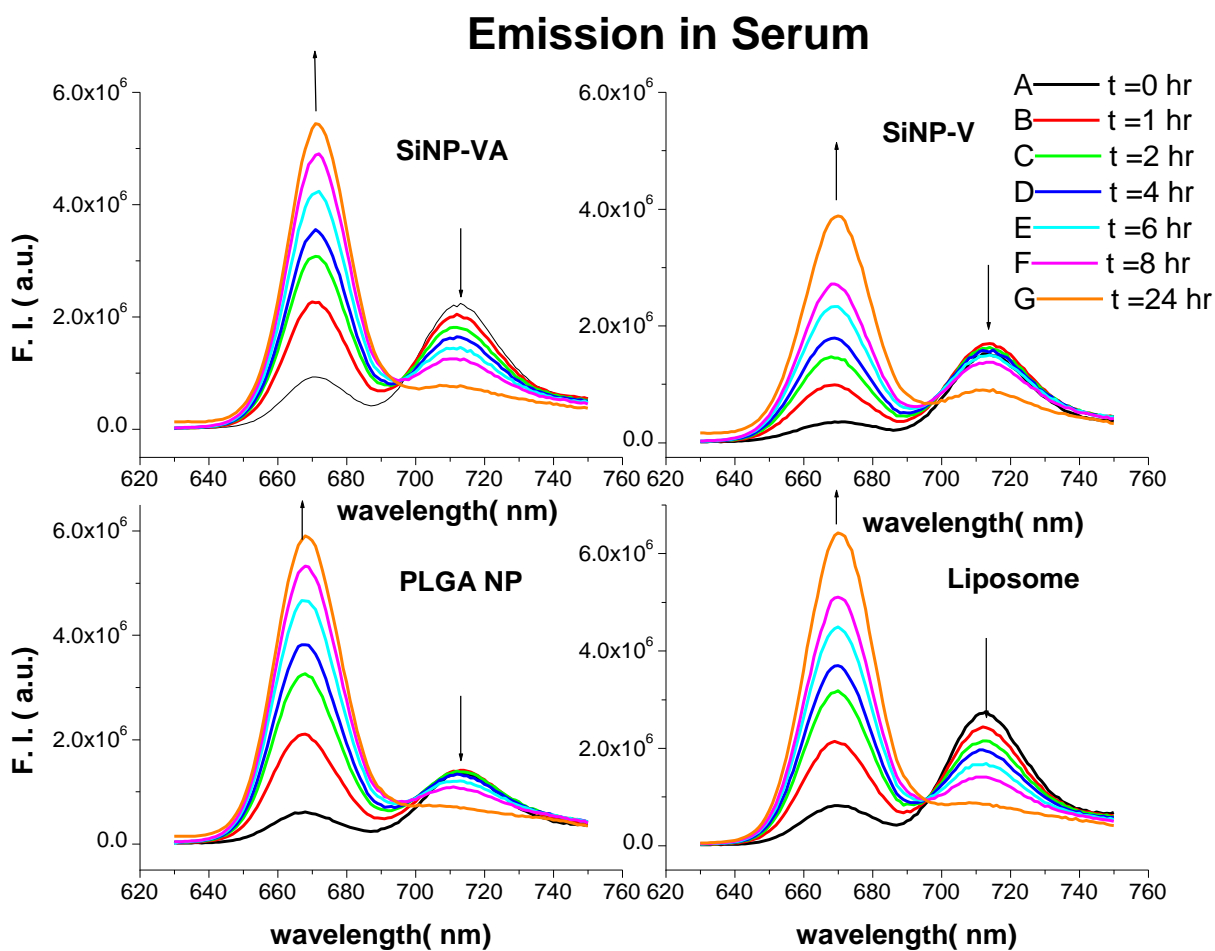


Figure 5.10 Time dependent fluorescence spectra of PP18 in SiNP-VA, SiNP-V, PLGA NP and liposome suspended in 10% serum at pH 7.4. These are monitored immediately after adding PP18 (time $t=0$), after 1, 2, 3, 5, 8, and 24 hours (shown as A, B, C, D, E, F, and G respectively). Arrows show the increase and decrease in the peak intensity at 670 nm and 710 nm corresponding to Cp_6 and PP18 emission peak respectively.

CHAPTER 6

SPECTROSCOPIC STUDIES ON METHYLENE BLUE AND NILE BLUE BOUND TO COATED GOLD NANORODS

In this chapter the results of our study on the effect of L-SP electric field of AuNRs on the optical (absorption and fluorescence) properties of two dyes Methylene Blue (MB) and Nile Blue (NB) are presented where the L-SP band was tuned and detuned with respect to the absorption maxima of the dyes. Binding between dyes and nanorods were established by electrostatic interaction by making the nanorods negatively charged after coating them with polystyrene sulphonate (PSS). The effect of dye/rod ratio on the extinction and fluorescence decay properties of the dye-AuNR complex is described.

Work discussed in this chapter resulted in the following publication:

1. 'Spectroscopic investigations on the binding of Methylene Blue and Nile Blue to negatively charged gold nanorods' R. Shrivastava, B. Jain and K. Das, *Journal of Molecular Structure*, Vol. 1020, pp. 56-62 (2012).

6.1 Introduction

The surface plasmon (SP) electric field of metallic nanoparticles (NP) can significantly affect the absorption and emission properties of molecular chromophores located nearby. Usually this results in a quenching of their fluorescence [158–163, 164–167], however, a good overlap between the molecular and plasmonic resonance may also result in resonant coupling between them [168–173, 174–179]. The radiative and nonradiative decay of the excited state of the chromophores is expected to depend critically on size and shape of the nanoparticle, the distance between the chromophore and the nanoparticle, the orientation of the molecular dipole with respect to the dye-nanoparticle axis, and the overlap of the molecule's emission with the nanoparticle's absorption spectrum [180].

In this chapter we have investigated how the SP field of gold nanorods affects the optical (absorption and emission) properties of two adsorbed dyes when their SP absorption is tuned to the absorption maximum of dye or away from it. For this we prepared PSS coated gold nanorods (AuNR) of different aspect ratio having their longitudinal surface plasmon band (L-SP) tuned with the absorption maxima of two dyes NB and MB and L-SP band tuned away from the absorption band of the dyes (the detuned condition). Earlier, the SP fields of different gold nanostructures have been utilized to enhance the Raman scattering from these dyes [181, 182].

6.2 Experimental Details

NB and MB from Exciton were used as received. The chemical structure of Nile Blue (NB), Methylene Blue (MB) and the repeating unit of PSS are shown in Fig. 6.1. AuNR samples with ensemble L-SP peaks at 730 nm and 700 nm, were grown in aqueous solutions varying the gold to seed ratio, and ascorbic acid to gold ratio as described in chapter 2 [98]. Shorter rods were prepared by oxidative shortening of an initial rod with L-SP at 700 nm, using H_2O_2 (50%) as the oxidizing agent [179].

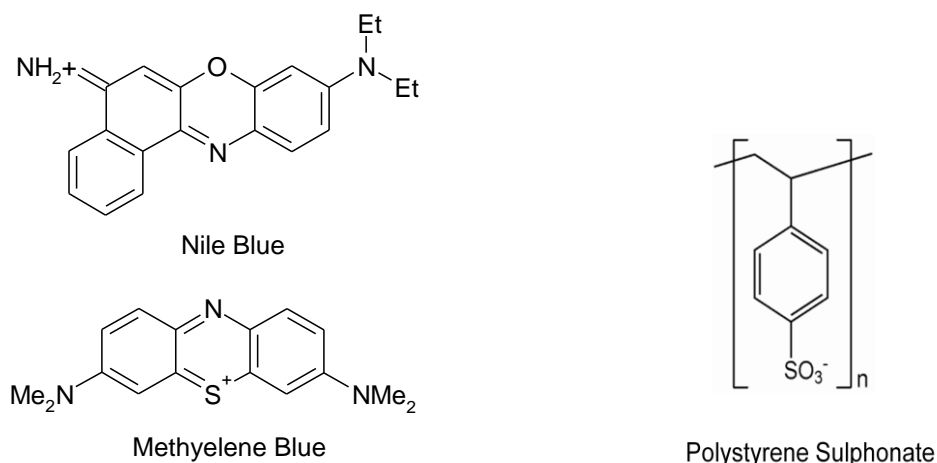


Figure 6.1 Chemical structures of the dyes and the polymer PSS used in this study

The ratio between the H₂O₂ solution and the as-grown nanorod solution was ~ 1:5. The oxidation reaction was stopped at controlled periods of time by centrifugation at 12,000 rpm for 2-3 min and washing twice with water and finally dispersing in water. This oxidation process led to the formation of two AuNR samples with L-SPR at 635 nm and 660 nm, matching to the molecular absorption of NB ($\lambda_{\text{max}} = 635$ nm) and MB ($\lambda_{\text{max}} = 664$ nm) respectively.

These prepared rods had a layer of CTAB over them which is positively charged. To make them negatively charged, PSS (75 KDa) was coated over these positively charged rods making their overall surface charge negative for binding to the positively charged dyes following the method as described in chapter 2. The excess PSS was removed by centrifuging and resuspending the pellet in Millipore water. The PSS coating changed the zeta potential (measured using a 90 Plus size and zeta potential analyzer) of the rods from ~ +50 mV to ~ -45 mV.

6.2.1 Absorption & Fluorescence spectroscopy

Absorption and fluorescence experiments were carried out in a cuvette of 1 cm path length. The absorption spectra of the dye-nanorod complex were recorded after addition

of a concentrated stock solution (typically few micro litres) of dye to a 0.06 nM nanorod solution. Similarly, the fluorescence spectra of the dye-nanorod complex were recorded after addition of a concentrated stock solution (typically few micro litres) of nanorods to a 5 μ M dye solution. The changes observed in the spectra after addition of dye was immediate and did not change with time during experiments. Steady state absorption and emission and time resolved fluorescence measurements of the rod-dye complex were done as described in chapter 2, section 2.3. NB and MB were excited at 635 and 665 nm respectively for steady state emission measurements. The emission lifetimes of the dyes were obtained by excitation at 635 nm using a picosecond diode laser. The fluorescence quantum yields (Φ_f) of MB and NB in aqueous environment were taken from previous reports [183,184] and the relative quantum yield in the presence of AuNRs were calculated accordingly. The radiative (k_r) and non radiative (k_{nr}) rates were calculated according to the relation: $k_r = \Phi_f/\tau_f$ and $k_{nr} = 1/\tau_f - k_r$, where τ_f is the average fluorescence lifetime.

6.3 Results

The normalized absorbance spectra of the AuNRs are shown in Fig. 6.2.

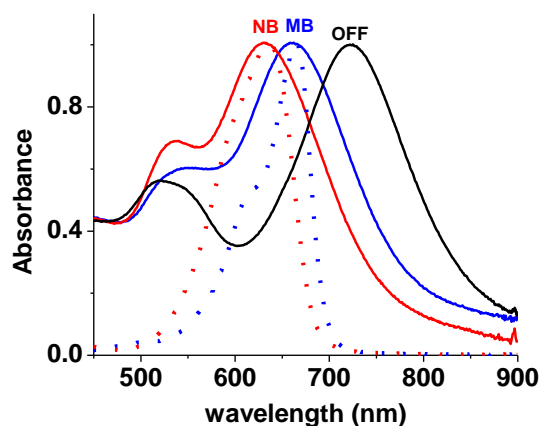


Figure 6.2 Normalized absorbance spectra of AuNRs used in this study along with the absorption spectra of MB and NB (as dots).

AuNRs with average aspect ratio of 3.5 ± 0.2 , 2.5 ± 0.2 and 2.3 ± 0.1 had the L-SP peaks centered at 730, 660 and 630 nm, respectively. The L-SP peak of AuNR at 630 nm, matches with the absorption of NB and the L-SP peak of another set of AuNR at 660 nm, matches with the absorption of MB while AuNRs having L-SPR at 730 nm is detuned from the absorption band of both the dyes.

6.3.1 Absorption properties of dye-AuNR systems

The changes observed in the absorbance spectra of the PSS coated AuNRs upon gradual addition of MB and NB is shown in Fig. 6.3 and 6.4 respectively for the tuned and detuned conditions.

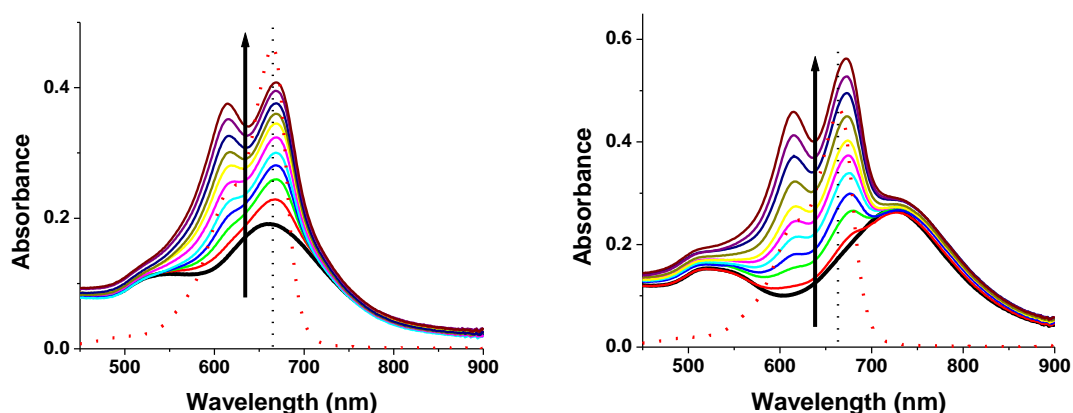


Figure 6.3 Changes in the absorbance spectrum of PSS coated AuNR (60 pM thick black curve) upon addition of MB. The arrow indicates increasing amount of the dye (in 0.5 μM steps). For comparison the spectra of 5 μM MB (dotted red curve) is also shown. The dashed line represents the absorption maxima of the free dye. Left: Tuned condition; right: detuned condition.

For comparison, the absorption spectra of 5 μM dye (the highest dye concentration used) are also shown in the figures. From these figures it is clear that with increasing amount of dye the resulting absorbance spectra becomes significantly different from the dye or nanorod absorbance spectra. The observed changes are likely to result from an electrostatic interaction between the positively charged dye and the negatively charged PSS coated AuNRs. The effect of addition of MB to an AuNR solution (0.06

nM) is described in Fig. 6.3. For the tuned condition, where the L-SP band of the AuNR matches with the absorption maxima of the dye, the gradual addition of the dye results in the appearance of two bands centred at 615 and 669 nm. For the detuned condition, where the L-SP band of the AuNRs were located at 730 nm, gradual addition of the dye again results in the appearance of two peaks located at 615 and 670 nm while the shoulder at 730 nm represents that of the L-SP band of the AuNRs. The effect of addition of NB to an AuNR solution (0.06 nM) is described in Fig. 6.4.

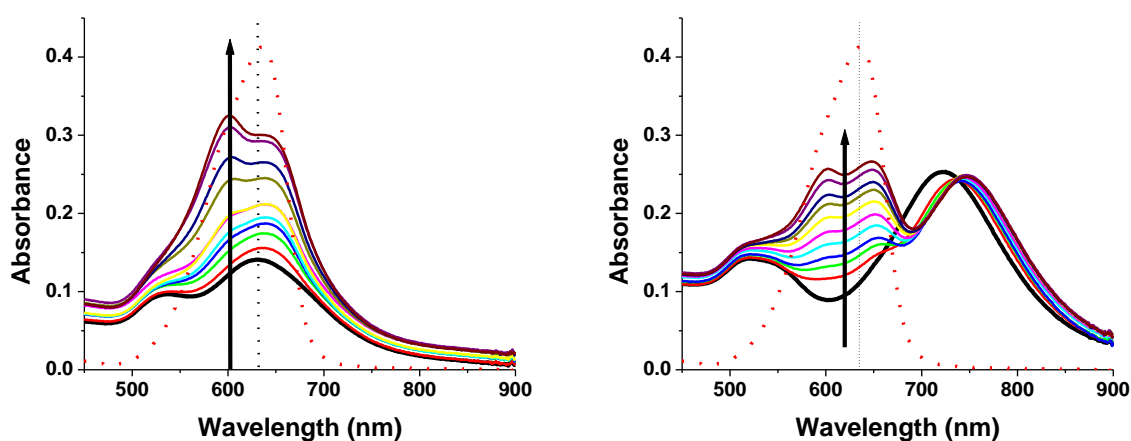


Figure 6.4 Changes in the absorbance spectrum of PSS coated AuNR (60 pM, thick black curve) upon addition of NB. The arrow indicates increasing amount of the dye (in 0.5 μM steps). For comparison the spectra of 5 μM NB (dotted red curve) is also shown. The dashed line represents the absorption maxima of the free dye. Left: Tuned condition; right: detuned condition.

For the tuned condition, the gradual addition of the dye results in the appearance of two bands centred at 603 and 640 nm. For the detuned condition, the gradual addition of the dye now results in the appearance of two peaks located at 600 and 645 nm with a shoulder at 525 nm (T-SP) and at ~ 730 nm (L-SP) representing the SP band of the rods. In addition the L-SP band of the AuNR shows a distinct red shift (from ~ 730 nm to ~ 750 nm) in the presence of the dye. The effect of only PSS on the absorption spectra of the dyes was also investigated as shown in Fig. 6.5. The absorption of MB decreases monotonically with increase in PSS concentration and at 10 μM concentration of the polymer it splits into two bands.

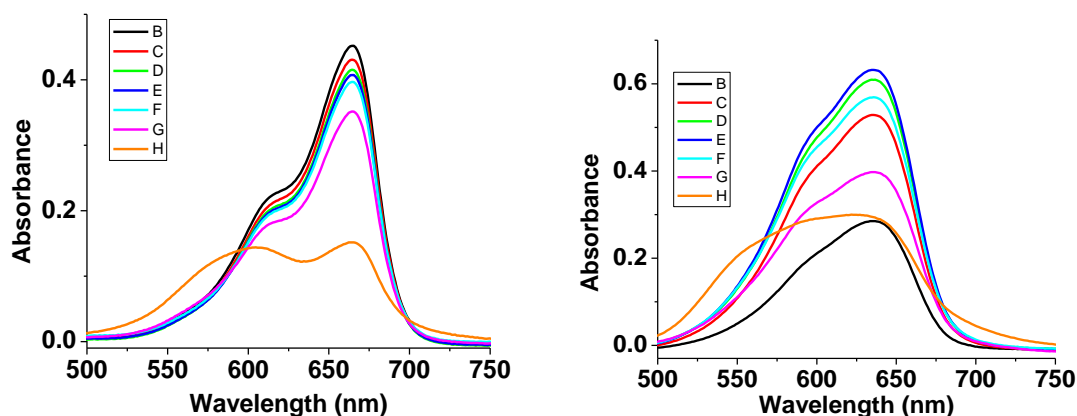


Figure 6.5 Absorption spectra of MB (left) and NB (right) in the presence of varying amount of PSS. B: No PSS; C: 0.1 nM PSS; D: 1 nM PSS; E: 10 nM PSS; F: 100 nM PSS; G: 1 μ M PSS and H: 10 μ M PSS

The absorption of NB, however, increases up to a PSS concentration of 10 nM and from there it starts to decrease and at 10 μ M concentration of the polymer the absorption band gets considerably broader. As stated in the introduction section, when the molecular and plasmonic resonances are overlapping, resonance coupling between them is a possibility, which is characterized by a splitting of the plasmon band. In this study, resonant coupling is expected to occur between-dyes and PSS coated AuNRs for the tuned condition because the absorption maximum of dyes matches with that of the L-SP band. In order to validate this, the absorption spectra of the dye-AuNR complex (in the range of 590-750 nm for MB-AuNR and 550-710 nm range for NB-AuNR) were fitted to two lorentzian line shapes (with an additional baseline).

Fig. 6.6 describes the changes of the absorption band maxima with increasing dye concentration. For the tuned condition, the separation between the high and low energy band increases with increasing dye concentration and seems to saturate when the dye concentration reaches 5 μ M. For the detuned condition, where the resonant coupling is expected to be weak, a similar Lorentzian fitting is done (in the range of 550-700 nm for MB-AuNR and 550-710 nm range for NB-AuNR; where the dye absorption is

dominating) to see how the band maxima evolve with increasing dye concentration. It is observed that the splitting of the high and low energy band occurs immediately after addition of 0.5 μM dye and thereafter stays same.

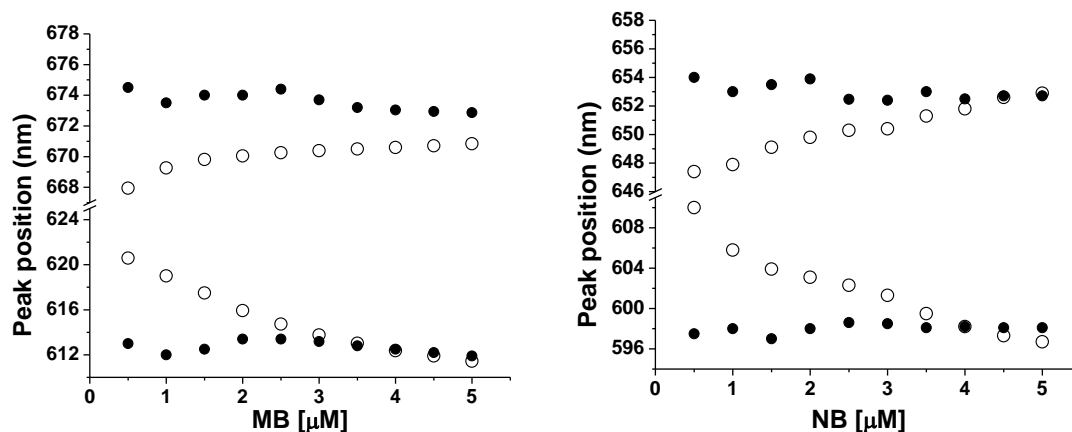


Figure 6.6 Changes in the absorption peak positions upon increasing amount of dye (in 0.5 μM steps). Hollow and solid circles represent the tuned and detuned conditions respectively. The spectra were fitted in the 590-750 nm (550-700 nm for detuned) and 550-710 nm (580-680 nm for detuned) range for MB and NB respectively by a pair of lorentzian line shapes along with a baseline.

6.3.2 Fluorescence properties of the dye-AuNR systems

In order to investigate how the SP field of the AuNRs affects the fluorescence properties of MB and NB, the fluorescence spectra of dyes were studied in the presence of increasing amount of AuNRs. For both tuned and detuned conditions, the fluorescence intensities of dyes were observed to be decreased in the presence of AuNRs (data not shown). The relative changes in the fluorescence quantum yield and the average lifetime for dyes upon sequential addition of PSS coated AuNRs are shown in Fig. 6.6.

For both tuned and detuned conditions, the quantum yield drops down significantly with the first addition of AuNRs (6 pM) and then increases slowly and starts to level off at higher rod concentrations. The quantum yield of fluorescence for MB decreases by 50% for the tuned condition whereas it decreases by 25% for the detuned

condition. In case of NB, the amount of decrease is 77% and 67% for the tuned and detuned condition respectively.

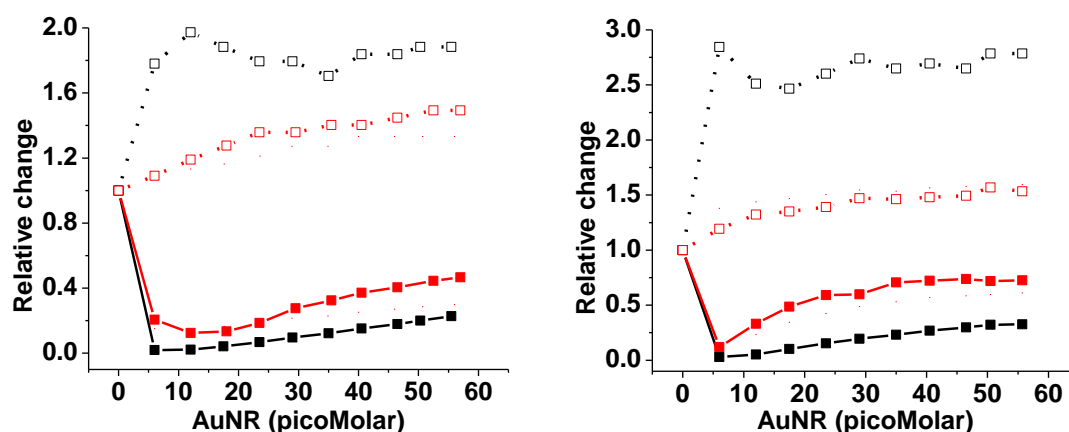


Figure 6.7 Relative changes in the fluorescence quantum yield (filled squares) and lifetime (hollow squares) of the two dyes (5 μM) in the presence of varying amount of PSS coated AuNRs. Left: tuned and right: detuned condition. NB: black; and MB: red.

The observed fluorescence decays of the two dyes in the absence of AuNRs can be well fitted by a sum of two exponentials. For MB and NB, the average lifetimes (in the absence of AuNRs) are observed to be similar as 220 ps. Since the fluorescence of dyes was significantly decreased in the presence of AuNRs, it is expected that their fluorescence lifetimes should also get decreased in the presence of AuNRs. However, the fluorescence lifetimes of dyes were observed to increase in the presence of AuNRs as shown in Fig. 6.8. Although the margin of increase is only modest for MB, it is quite significant for NB. At a rod concentration of 12 pM, the average lifetime of MB increases by 1.2 and 1.4 times for the tuned and detuned conditions respectively whereas for NB this amounts to 2 and 2.5 times. However, increasing the rod concentration further does not affect the lifetimes any more.

At the highest rod concentrations used in this study (~ 56 pM) the average lifetime of MB increases by 1.5 times for both tuned and detuned conditions whereas for NB this amounts to 2 and 2.8 times respectively. Since changes in the quantum yield and

lifetimes are governed by the radiative and the nonradiative processes in the excited state, how they change in the presence of the AuNRs is shown in Fig. 6.9.

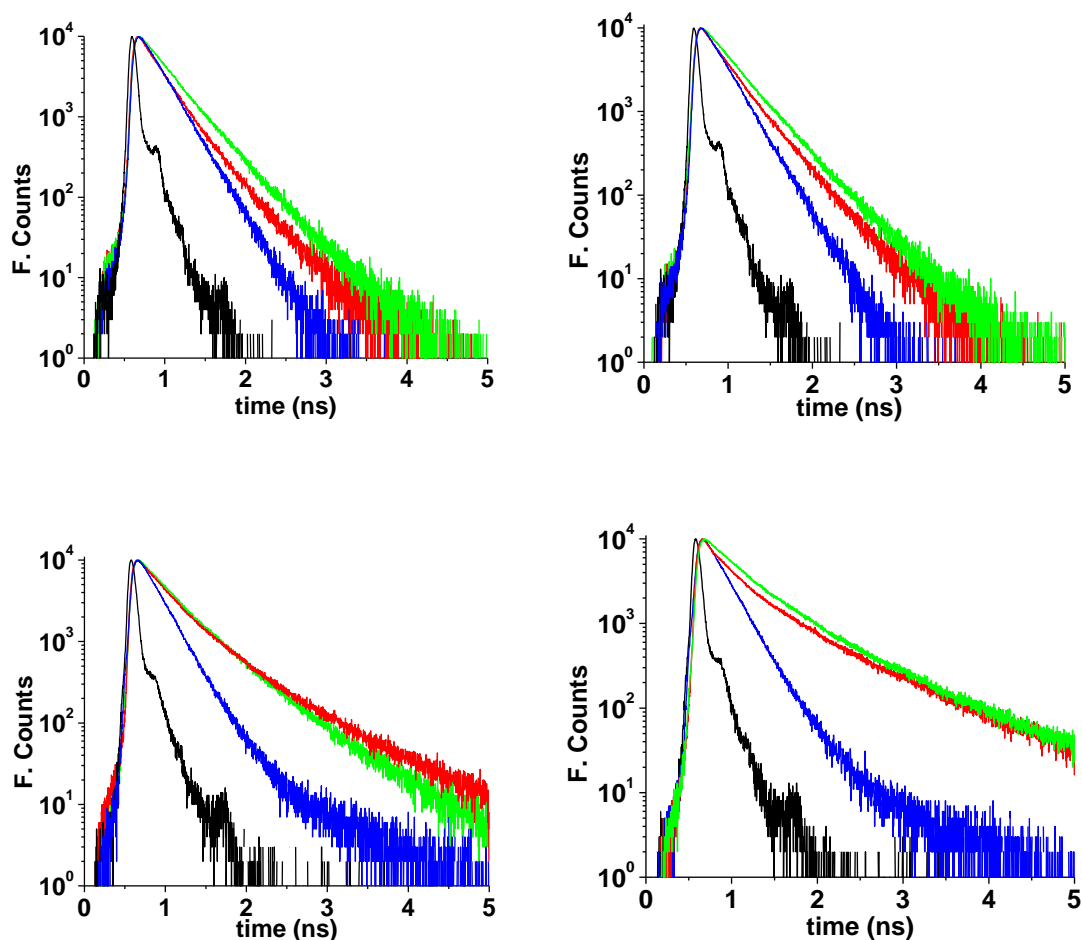


Figure 6.8 Changes in the fluorescence lifetimes of the two dyes ($5 \mu\text{M}$) in the presence of various amounts of AuNRs. Black: only dye; Red: dye + 12 pM AuNR and Green: dye + 60 pM AuNR. Top: MB and bottom: NB. The left panel shows the decays for the tuned and the right panel shows the decays for the detuned conditions.

For both tuned and detuned conditions, the radiative rate (k_r) decreases significantly ($> 80\%$) with the initial addition of AuNRs. After that, for the tuned condition, k_r increases only modestly for both the dyes. However, for the detuned condition, against increasing rod concentration, the observed trend of k_r is quite different for MB and NB. The nonradiative rates for both the dyes were observed to decrease in the presence of increasing amount of AuNRs.

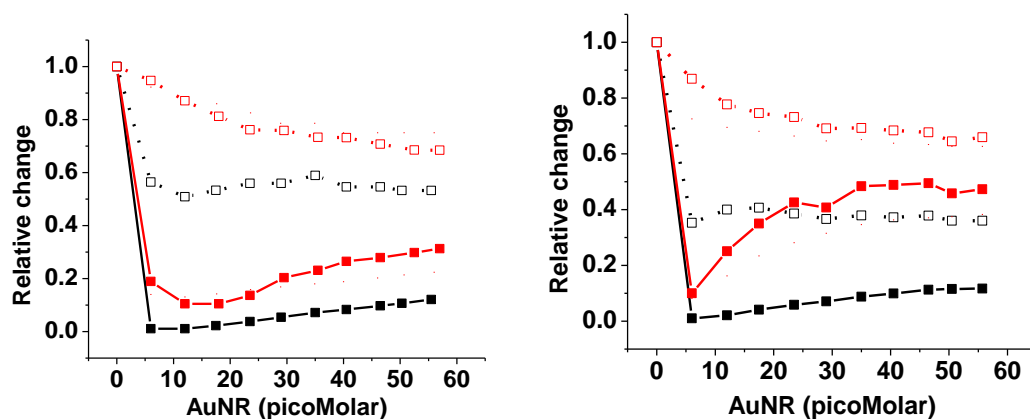


Figure 6.9 Relative changes in the k_r (filled squares) and k_{nr} (hollow squares) of the two dyes in the presence of varying amount of PSS coated AuNRs. Left: tuned and right: detuned condition. NB: black; and MB: red.

For NB, the magnitude of decrease in k_{nr} was observed to be significantly higher than MB. The values of fluorescence quantum yields, average lifetimes, radiative and nonradiative rates for the two dyes in the presence of varying amount of PSS coated AuNRs are given in Table 6.1.

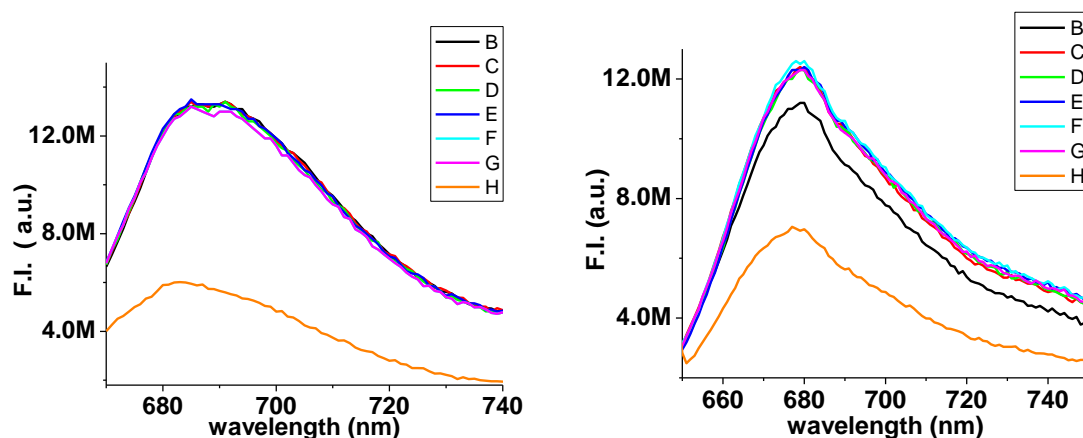


Figure 6.10 Fluorescence spectra of MB (left) and NB (right) in the presence of varying amount of PSS. B: No PSS; C: 0.1 nM PSS; D: 1 nM PSS; E: 10 nM PSS; F: 100 nM PSS; G: 1 μ M PSS and H: 10 μ M PSS.

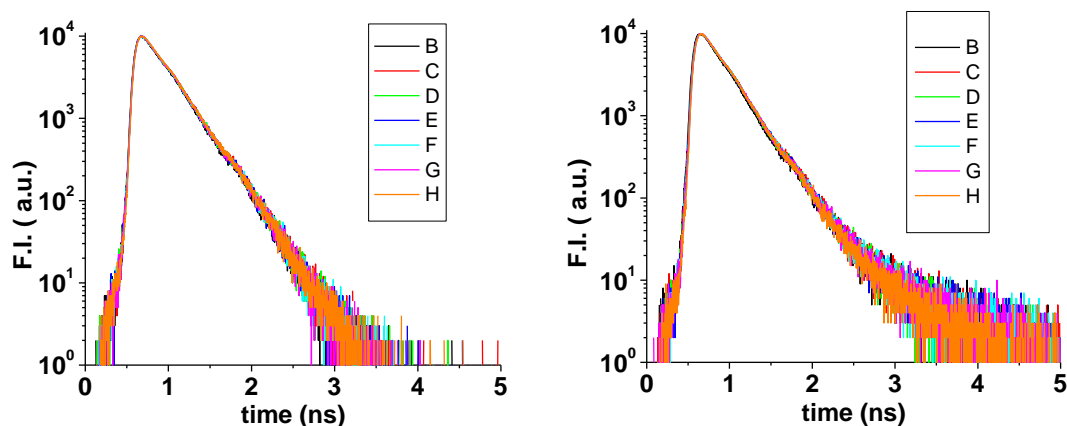


Figure 6.11 Fluorescence decay traces of MB (left) and NB (right) in the presence of varying amount of PSS. B: No PSS; C: 0.1 nM PSS; D: 1 nM PSS; E: 10 nM PSS; F: 100 nM PSS; G: 1 μ M PSS and H: 10 μ M PSS

We also studied the effect of PSS on the fluorescence properties of the dyes as shown in Fig. 6.10 and Fig.6.11. For PSS concentration range of 0.1 nM to 1 μ M, the changes in the fluorescence intensities of the dyes were modest and only at a polymer concentration of 10 μ M, it were observed to decrease significantly. However, lifetimes of the two dyes remains unchanged at all the concentrations (0.1 nM- 1 μ M) of the polymer.

6.4 Discussion

The objective of this study was to investigate how the optical properties of two dyes (MB and NB) are affected by the SP electric field of the AuNRs for the tuned and detuned conditions. The absorption spectrum of the dye-AuNR complex is significantly different from the free dye or the free AuNR for both tuned and detuned conditions. It has been reported that in aqueous solution both MB and NB can form aggregates (dimers) upon addition of different aggregating agents [185, 186, 187]. For example, electrostatic interaction between NB and silica colloids results in the formation of the dimeric species [187] while negatively charged polymers like PSS has been shown to favor the formation of dimeric MB [186]. The formation of dimeric species will reduce the concentration of the monomeric species and in absorption spectrum this would reflect in an increase in the

Table 6.1 Fluorescence parameters of MB and NB in the presence of various amounts of PSS coated AuNRs

Tuned					Detuned				
AuNR (pM)	Φ_f	τ_f (ns) (average)	k_r ($\times 10^8 s^{-1}$)	k_{nr} ($\times 10^8 s^{-1}$)	AuNR (pM)	Φ_f	τ_f (ns) (average)	k_r ($\times 10^8 s^{-1}$)	k_{nr} ($\times 10^8 s^{-1}$)
Methylene Blue									
0	0.040	0.22	1.80	43.0	0	0.040	0.22	1.80	43.0
6	0.008	0.24	0.18	37.4	6	0.005	0.27	0.34	41.2
12	0.005	0.26	0.45	33.4	12	0.013	0.30	0.19	37.8
18	0.005	0.28	--	--	17.5	0.019	--	0.19	35.3
23.5	0.007	0.30	0.76	31.5	23.5	0.024	0.31	0.25	33.1
29.5	0.011	0.30	0.73	29.8	29	0.024	0.33	0.37	33.0
35.5	0.013	0.31	0.87	29.8	35	0.028	0.33	0.42	31.8
40.5	0.015	0.31	0.86	29.4	40.5	0.029	0.33	0.48	31.8
46.5	0.016	0.32	0.89	29.1	46.5	0.030	0.33	0.51	30.7
52.5	0.018	0.33	0.82	27.8	50.5	0.029	0.35	0.54	29.8
57	0.019	0.33	0.85	28.4	55.7	0.029	0.34	0.57	29.7
Nile Blue									
0	400E-5	0.22	0.179	44.7	0	400E-5	0.22	0.179	44.7
6	7.6E-5	0.40	0.002	25.2	6	11.6E-5	0.62	0.002	16.0
12	8.7E-5	0.44	0.002	22.7	12	21.1E-5	0.55	0.004	18.2
17.5	16.7E-5	0.42	0.004	23.8	17.5	40.7E-5	0.54	0.008	18.5
23.5	27.2E-5	0.40	0.007	25.0	23.5	60.9E-5	0.57	0.010	17.5
29	38.6E-5	0.40	0.010	25.0	29	77.8E-5	0.60	0.013	16.7
35	48.9E-5	0.38	0.013	26.3	35	93.0E-5	0.58	0.016	17.2
40.5	60.9E-5	0.41	0.015	24.4	40.5	107.0E-5	0.59	0.018	16.9
46.5	71.7E-5	0.41	0.017	24.4	46.5	119.0E-5	0.58	0.021	17.2
50.3	80.3E-5	0.42	0.019	23.8	50.5	129.0E-5	0.61	0.021	16.4
55.5	91.3E-5	0.42	0.022	23.8	55.7	130.0E-5	0.61	0.021	16.4

intensity of the dimer band (usually located on the higher energy side of the monomer band) and a decrease for the monomer band. This is indeed seen in the presence of 10 μM PSS (Fig. 6.5).

For MB and NB, the higher energy band (located at 615 and 600 nm respectively) is likely to represent the dimeric species while the monomeric species absorb at 670 and 640 nm, respectively. However, the relative intensities of the band maxima for the dimeric and monomeric species are observed to be different for MB and NB. For MB, the intensity of the band corresponding to the monomeric species is observed to be higher than that of the dimeric species for both tuned and detuned conditions (Fig. 6.3). In case of NB they are reversed for the tuned condition and nearly equal for the detuned condition (Fig. 6.4). The absorption spectra of the dye-nanorod complex may result from aggregation of the dyes induced by nanorods or from resonance coupling between the dye and the nanorods.

As observed in earlier works [168-179] plasmon-molecular resonance coupling results in a splitting of the plasmon peak whose magnitude increases with increasing dye concentration and then saturates when full monolayer coverage of dye is approached. This is indeed observed for the tuned condition (Fig. 6.6). It is interesting to note that the magnitude of splitting observed at the highest dye concentration was observed to be ~ 20 nm for the NB-AuNR complex, double of that observed for MB-AuNR complex. In an earlier work, the coupling between MB and PSS coated AuNR having an L-SP band at 680 nm was studied [179]. The plasmon shift, defined as the difference between the lower-energy peak wavelength of the hybrid nanostructure and the L-SP peak of the PSS-coated AuNR was observed to be ~ 40 nm for dye:AuNR ratio of $\sim 130 \times 10^3$. The plasmon shift observed in our study corresponds to about ~ 10 nm for dye:AuNR ratio of $\sim 80 \times 10^3$. The observed spectral features of the dye-AuNR complexes are also different from the earlier study. This is probably due to significant differences in the dye:AuNR

ratio. For the detuned condition the observed trend of the peak splitting is significantly different which we attribute to nanorod induced aggregation of the dyes.

The fluorescence intensities of dyes in the presence of increasing amount of PSS coated AuNRs were observed to be decreased. This might arise due to: formation of dimeric species which are nonfluorescent in nature and/or quenching of fluorescence due to presence of SP electric field. However, the increase in the fluorescence lifetime of the dyes in the presence of increasing amount of PSS coated AuNRs is surprising because as shown in earlier reports, SP electric field generally quenches the lifetime of the chromophores near its vicinity [158-167]. Because of the good overlap between the fluorescence and L-SP band for the tuned condition, this effect is expected to be more pronounced due to energy transfer process. A look at Fig. 6.9 and Table 6.1, shows that both k_r and k_{nr} of dyes decreases in the presence of AuNRs. The magnitude of decrease for k_r is much greater than that for k_{nr} . For NB, k_r decreases by ~90% whereas k_{nr} decreases by 50-60% for both tuned and detuned conditions. For MB, k_r decreases by ~75-60% whereas k_{nr} decreases by 30% for tuned and detuned conditions, respectively. The much higher decrease of the radiative rates can be attributed to the combined effect of formation of the non-fluorescent dimeric species of dyes on the surface of the AuNRs and the presence of the L-SPR field. The decrease, in the nonradiative rates is most likely to be due to the binding of the monomeric species of the dye to the PSS coated AuNR surface, which reduces the nonradiative pathways for these dyes (such as, intramolecular proton transfer for NB [188, 189]).

It is interesting to note that the magnitude of the increase in lifetime is indeed affected by the spectral position of the L-SP electric field. From Fig. 6.7 and 6.8 and data presented in Table 6.1 it can be seen that for detuned condition the magnitude of the increase in lifetime is higher compared to the tuned condition. Thus, the observed changes in the optical (absorption and fluorescence) properties of these two dyes upon binding to AuNRs depends upon various factors like, binding geometry (monomer-

dimer), changes in the excited state decay channels and presence of L-SP field of the AuNRs.

6.5 Conclusion

We have studied how the spectroscopic (absorption and fluorescence) properties of MB and NB are affected by the L-SP electric field of PSS coated AuNRs. The electrostatic interaction between the negatively charged AuNRs and the positively charged dyes results in significant changes in the absorption and emission properties of the dyes. For both tuned and detuned cases, there are two absorption bands in the 550-700 nm regions of the dye-AuNR complex. For the detuned condition, the resulting changes in the absorption spectra of the dye are attributed to nanorod induced aggregation. However, for the tuned condition the formation of high and low energy bands are attributed to the resonance coupling between the L-SP of the AuNR and dye absorption. This is further supported by the observation that the splitting of the absorption bands increases with increasing dye concentration and then saturates. Although, the fluorescence intensity of the dyes in the presence of increasing amount of PSS coated AuNRs were observed to be decreased, the corresponding lifetimes were observed to increase. This is explained on the basis of the formation of nonfluorescent dimeric species, suppression of the excited state nonradiative decay channels and the influence of the L-SP.

CHAPTER 7

PHOTOPHYSICAL PROPERTIES OF CHLORIN P_6 BOUND TO COATED GOLD NANORODS

In this chapter we present the results on our study on the interaction of photosensitizer Cp_6 with coated gold nanorods. The effect of different coating materials (surfactant and polymers) and surface plasmon resonance of gold nanorods (AuNRs), on the photophysical properties of Cp_6 such as quantum yield, radiative and non-radiative decay, photobleaching etc is described.

7.1 Introduction

Since colloidal gold is stable, biocompatible and nontoxic [190] there exists a considerable interest in the development of multi-functional gold nanostructures for diagnostic and therapeutic applications [191, 192, 193, 194]. In particular, gold nanorods

Work discussed in this chapter has been published as follows:

1. 'Photophysical Properties of Chlorin p_6 Bound to Coated Gold Nanorods' B. Jain, A. Uppal, P. K. Gupta and K. Das, *Journal of Molecular Structure*, Vol. 1032, pp. 23-28 (2013).

(AuNR), with absorption in the near infra-red (NIR) spectral region (~650-900 nm), are being actively investigated for contrast based imaging and hyperthermia [195, 196]. This follows because the optical transparency of biological tissue is highest in this region and AuNR are particularly suited for these applications because of their large absorption cross-section and high photothermal conversion efficiencies [197]. A recent study suggests that a combination of photodynamic therapy (PDT) and hyperthermia can be more effective than either PDT or hyperthermia alone and this can be easily realised by conjugating NIR absorbing photosensitizers with NIR absorbing AuNRs [95]. One of the most popular methods for the preparation of AuNR is the use of rod-shaped micelles, formed from the surfactant, cetyl trimethylammonium bromide (CTAB), as templates [76, 77, 98]. However, the high concentration of CTAB employed in synthesis of AuNRs has raised some concerns regarding their toxicity [198, 199, 80, 200, 201]. Therefore, efforts have been made to remove the extra CTAB from the NP suspension and to overcoat the CTAB coating with other materials that lead to better biocompatibility and stability of the AuNRs [195-201].

AuNRs coated with positively charged polymers like poly allylamine hydrochloride (PAH) and poly diallyl dimethyl ammonium chloride (PDDAC) have been shown to have reduced cytotoxicity and improved cellular uptake [80, 200]. In this chapter we have used PAH and PDDAC coated AuNRs to study the binding between them and Cp_6 a negatively charged photosensitizer having substantial absorption in the 660 nm region. The binding is investigated by monitoring the absorption and fluorescence properties of Cp_6 in the presence of AuNRs with two different aspect ratios such that their L-SP was tuned to and away from the Q band absorption of Cp_6 .

We show that the photophysics of Cp_6 bound to AuNR depend significantly upon the nature of the coating material of the AuNRs. Chemical structures of Cp_6 and polymers PAH and PDDAC are shown in Fig. 7.1.

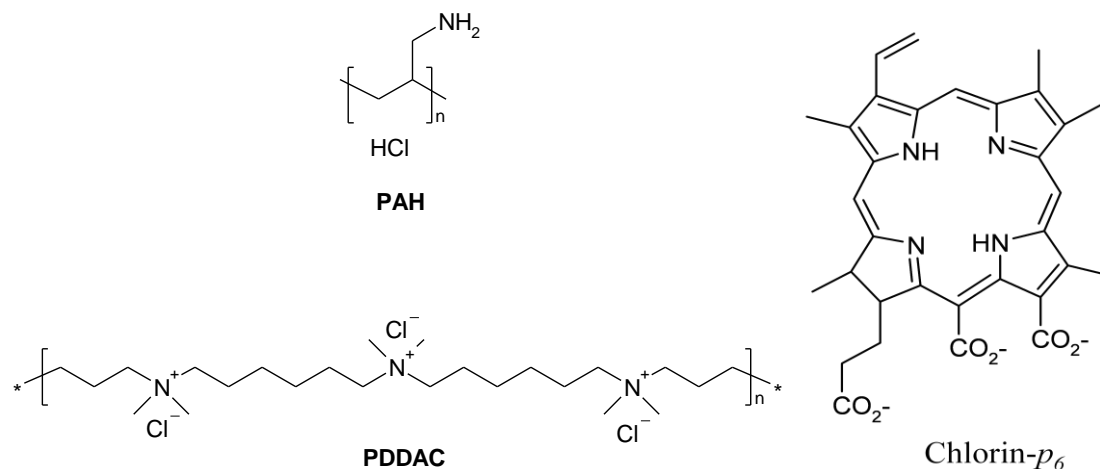


Figure 7.1 Chemical structure of Cp_6 and repeating unit of the two polymers PAH and PDDAC used in this study.

7.2 Experimental Details

CTAB-coated AuNRs having different L-SPR were synthesized described in chapter 2. These CTAB coated rods are positively charged. As these polymers are also positively charged, the rods were first coated with PSS which is negatively charged and then coated with PAH or PDDAC. The details of the procedure are given in chapter 2, section 2.1.2. These coated rods were finally suspended in Millipore water at pH 7.4 for further experiments. The molar extinction coefficient of AuNRs used in this study with aspect ratio of ~ 2.5 was estimated to be $\sim 3.17 \times 10^9 \text{ M}^{-1}\text{cm}^{-1}$ and aspect ratio of ~ 3.8 was estimated to be $\sim 4.75 \times 10^9 \text{ M}^{-1}\text{cm}^{-1}$ following the procedure given in reference 103.

For absorption and fluorescence measurements AuNR concentration of ~ 60 picomolars was used for both the rods. The complex of Cp_6 and AuNR were made by simply adding them together and mixing for a short while. Absorption and fluorescence measurements were done as described in chapter 2, section 2.3. The photobleaching of the drug and the drug nanorod conjugates was studied by photoillumination centered at $660 \pm 20 \text{ nm}$ at a light dose rate of $0.26 \text{ J/cm}^2/\text{min}$.

7.3 Results

Typical TEM images of the PAH and PDDAC coated AuNR are given in chapter 2, (Fig. 2.4). After PAH or PDDAC coating about 95% of the nano structures were observed to be rod shaped and rest were either spherical or irregular shaped. The coated AuNRs had an average aspect ratio of 2.5 ± 0.2 and 3.8 ± 0.3 . The absorption spectra of the AuNRs used in this study are shown in Fig. 7.2.

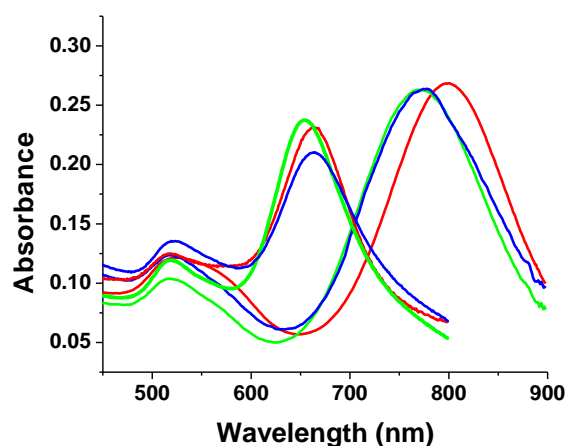


Figure 7.2 Absorbance spectra of CTAB (red), PAH (green) and PDDAC (blue) coated AuNRs at physiological pH. The two sets of rods are with L-SP peak at ~ 660 and ~ 800 nm. See also Table 7.1 for additional details.

For the shorter aspect ratio, the L-SPR peak was centred on ~ 660 nm and the effect of PAH or PDDAC coating on the L-SPR band position were observed to be insignificant. However for the longer aspect ratio AuNRs the PAH or PDDAC coating resulted in a significant blue shift of the L-SPR band (from 800 to 770 nm, see Table 7.1). The zeta potential of the coated AuNRs at physiological pH was observed to be positive. For the CTAB coated short aspect ratio AuNRs the measured zeta potential was 27 ± 5 mV. When these CTAB coated AuNRs were over coated with the negatively charged polymer PSS the zeta potential values became -44 ± 4 mV respectively. Upon further coating with positively charged polymer PAH (or PDDAC) the zeta potential values

became 33 ± 4 (or 34 ± 1 mV). For the long aspect ratio rods the trends in the zeta potential values upon successive coating with PSS and PAH (or PDDAC) are similar (Table 7.1).

Table 7.1 Size, zeta potential and SPR band position of different coated AuNRs

Coating	Aspect ratio 2.5 ± 0.2		Aspect ratio 3.8 ± 0.3	
	L-SPR band position (nm)	Zeta potential (mV)	L-SPR band position (nm)	Zeta potential (mV)
CTAB	653	26 ± 5	798	20 ± 7
PAH	654	33 ± 4	770	31 ± 6
PDDAC	662	35 ± 1	777	36 ± 2

Since the zeta potential of the AuNRs is positive and the drug is negatively charged at physiological pH, they can bind to each other by electrostatic interaction. The zeta potential of the drug-AuNR complex is an important parameter because it shows the stability of the complex. The observed zeta potentials of the various drug-nanorod complexes (drug: AuNR = $\sim 1.5 \times 10^3$) are shown in Fig. 7.3.

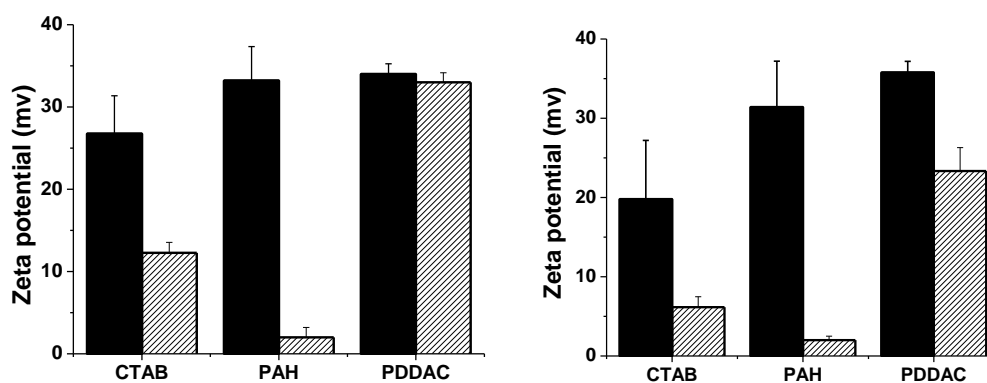


Figure 7.3 The observed zeta potentials of the coated AuNRs with L-SPR ~ 660 nm (left) and ~ 800 nm (right) and their complexes with Cp_6 (shaded bars).

The figure shows that change in the zeta potential of the AuNRs after addition of Cp_6 ($2 \mu\text{M}$) is significantly high in case of PAH coated AuNRs, where the measured zeta potential values are close to zero. The absorption, emission and fluorescence decay curves

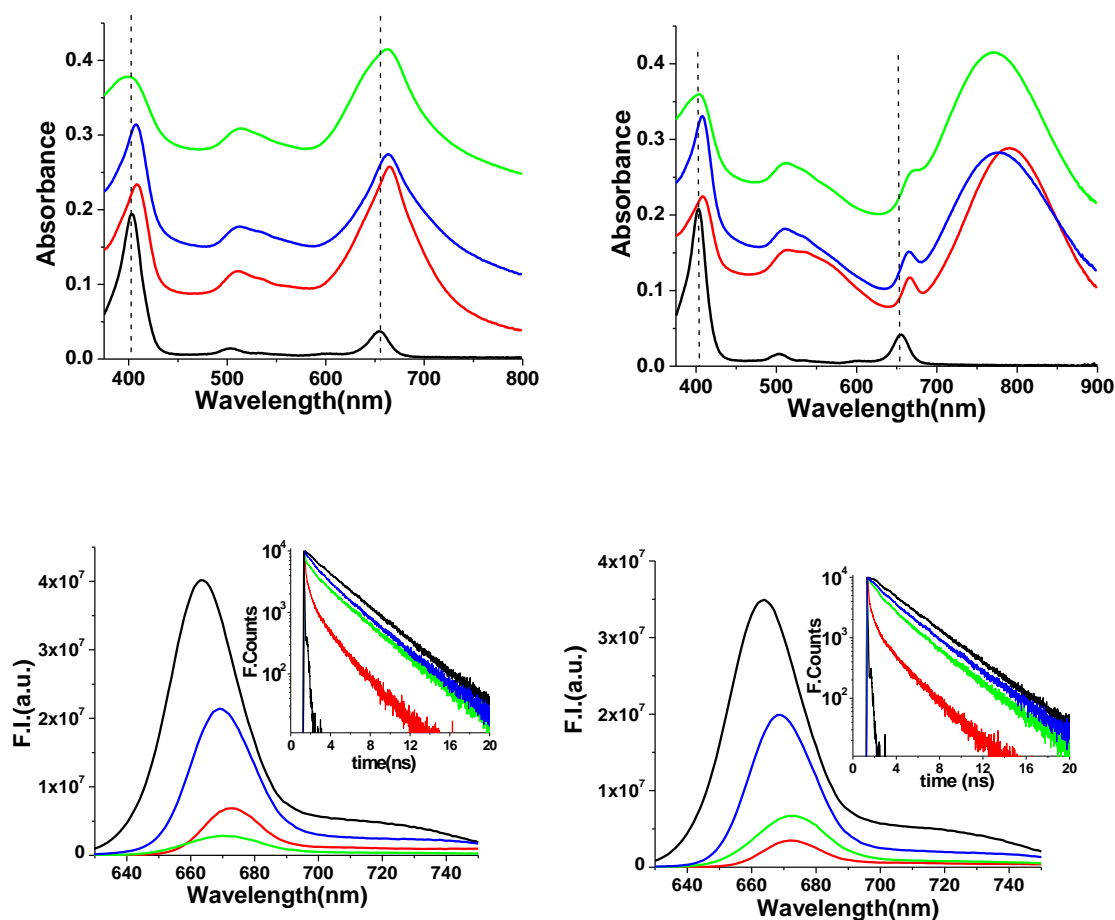


Figure 7.4 Absorption (top) and fluorescence (bottom) spectra ($\lambda_{ex} = 400$ nm) of Cp_6 in presence of different coated AuNR at physiological pH. The left and right panel corresponds to AuNRs having L-SPR at ~ 660 and ~ 800 nm respectively. The inset at bottom panel shows the corresponding fluorescence decay of the drug. Dashed vertical lines correspond to the Soret and Q-band maxima of the free drug.

Colour code: Cp_6 (black); CTAB coated AuNR- Cp_6 (red); PAH coated AuNR- Cp_6 (green) and PDDAC coated AuNR- Cp_6 (blue).

of free Cp_6 and Cp_6 in the presence of differently coated AuNRs (rod concentration ~ 60 pM) at physiological pH are shown in Fig. 7.4. As already discussed in the earlier chapters, the absorption spectra of the free drug shows two distinct peaks at ~ 400 (Soret band) and ~ 655 nm (Q-band) [91]. The composite absorption spectra of the drug-AuNR system (Fig. 7.4, top) show two distinct peaks at ~ 400 and ~ 660 nm which can be attributed to the Soret and Q-band of the drug modified by the plasmon resonance of the

AuNR. The emission band maxima of free Cp_6 is at ~ 663 nm, but in the presence of various coated AuNRs the band maxima are observed to be significantly red shifted (Fig. 7.4, bottom). In addition, the fluorescence of the drug is observed to quench significantly in the presence of coated AuNRs.

Interestingly, the amount of red shift and the amount of quenching is observed to depend upon the coating on the AuNRs. As expected, the fluorescence lifetime of the drug is also observed to quench in the presence of AuNRs, the amount of quenching being highest for CTAB coated AuNRs. In order to understand the nature of fluorescence quenching of the drug in the presence of the various coated AuNRs the radiative (k_r) and the nonradiative

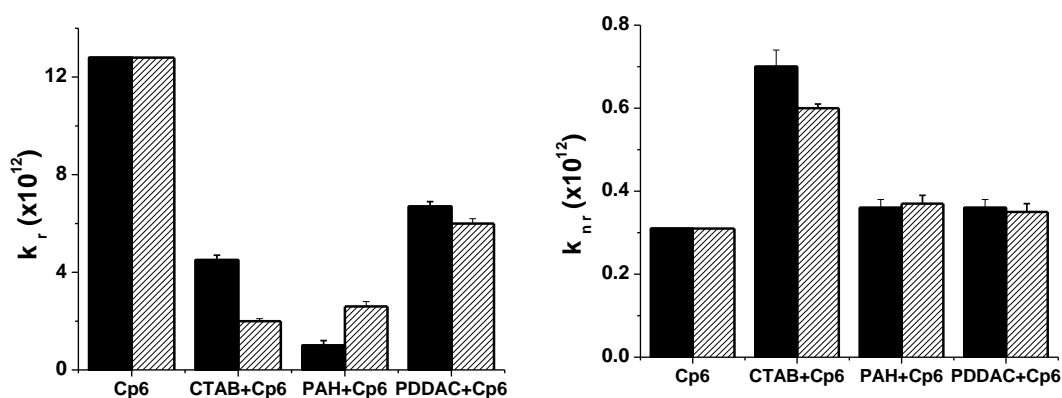


Figure 7.5 Radiative (left) and nonradiative (right) decay rates of the free Cp_6 and Cp_6 in the presence of coated AuNRs (black: L-SPR ~ 660 nm; shaded: L-SPR ~ 800 nm).

(k_{nr}) rates of the drug are calculated from the respective quantum yield (Φ_f) and average lifetime (τ) values (using the relations: $\Phi_f = k_r \tau$ and $k_{nr} = \tau^{-1} - k_r$). Fig. 7.5 shows the radiative and nonradiative decay rates of the free Cp_6 and Cp_6 in the presence of AuNRs. The figure shows that, in the presence of coated AuNRs, the radiative decay rates of Cp_6 decreases significantly especially for the PAH coated AuNRs, whereas the nonradiative decay rates of the Cp_6 are not affected by both PAH and PDDAC coating.

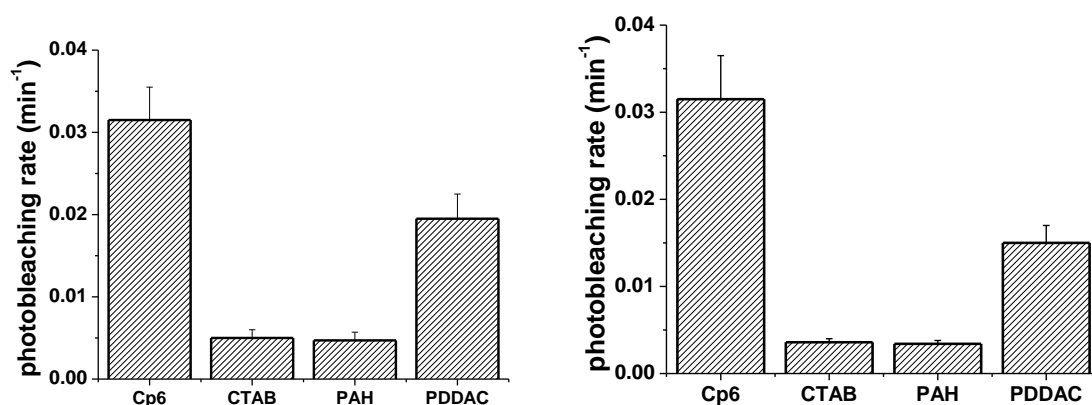


Figure 7.6 Percentage photobleaching of Cp_6 and its complexes with different coated AuNRs (left: L-SPR ~ 660 nm; right: L-SPR ~ 800 nm). See experimental section for more details.

The photobleaching of free Cp_6 and Cp_6 in presence of coated AuNR was studied by irradiating the samples at the Q-band absorption region of the drug. It was observed that photo illumination results in an overall decrease in the absorbance of the drug. This was quantified by monitoring the rate of change of the absorbance at the Soret peak (~ 400 nm) of the drug. The photobleaching rate of the free drug and drug-AuNR systems are shown in Fig. 7.6. Compared to Cp_6 , the photobleaching rate was observed to be lower for all drug-AuNR systems. The photobleaching rate of the free drug and drug-AuNR systems are shown in Fig. 7.6.

Table 7.2 Photophysical and photobleaching parameters of Cp_6 bound to different coated AuNRs at physiological pH¹

System	Emission parameters					Photobleaching rate (min ⁻¹)
	Maxima (nm)	Φ_f ($\times 10^3$)	τ_{av} (ns)	k_r ($\times 10^6 s^{-1}$)	k_{nr} ($\times 10^9 s^{-1}$)	
Cp_6	663	40*	3.1 \pm 0.1	12.8 \pm 0.3	0.31 \pm 0.2	0.0315
CTAB-AuNR- Cp_6	673	7 \pm 1	1.5 \pm 0.2	4.5 \pm 0.2	0.70 \pm 0.04	0.0050
	673	4 \pm 1	1.5 \pm 0.2	2.5 \pm 0.1	0.64 \pm 0.01	0.0042
PAH-AuNR- Cp_6	673	3 \pm 0.5	2.8 \pm 0.1	1.0 \pm 0.2	0.36 \pm 0.02	0.0034
	671	7 \pm 0.5	2.6 \pm 0.2	2.6 \pm 0.2	0.37 \pm 0.02	0.0031
PDDAC-AuNR- Cp_6	669	18 \pm 3	2.7 \pm 0.1	6.7 \pm 0.2	0.36 \pm 0.02	0.0195
	669	18 \pm 1	2.8 \pm 0.1	6.0 \pm 0.2	0.35 \pm 0.02	0.0150

¹The values in italics corresponds to longer aspect ratio rods

* Fluorescence quantum yield of Cp_6 at physiological pH has been taken from ref. 137.

Compared to Cp_6 , the photobleaching rate was observed to be lower for all drug-AuNR systems. In particular, the photostability of the drug was observed to increase by ~six and ~ten times respectively in presence of CTAB and PAH coated AuNRs. The photophysical as well as photobleaching parameters of the Cp_6 -AuNR systems as well as free Cp_6 are provided in Table 7.2.

7.4 Discussion

Cp_6 , a porphyrin based photosensitizer, has three ionizable carboxylic acid groups and at neutral pH it is tri-anionic in nature. The molecule absorbs over the entire visible spectrum and has two prominent bands at ~400 (Soret) and ~655 (Q-band) nm [156]. It has been reported earlier that the binding of the drug with other macromolecular systems affects the position of the Q-band maxima [91, 134, 136, 137, 156].

The major objective of this study was to investigate how the chemical nature of the coated material as well as the SPR of the positively charged AuNRs affects the photophysical properties of a negatively charged photosensitizer, Cp_6 . A change in the coating material (from CTAB to PAH or PDDAC) resulted in a slight increase of the zeta potential of the AuNRs (30-35 mV compared to 20-25 mV as shown in Table 7.1). For short aspect ratio AuNRs, a change in coating material hardly affected the SPR position but for longer aspect ratio AuNRs this resulted in a significant blue shift of the L-SPR band position (Fig. 7.2). This is expected because the dielectric sensitivity of the L-SPR band increases with increasing aspect ratio [76, 77, 98]. The zeta potential of the AuNR were observed to decrease upon addition of Cp_6 (Cp_6 : AuNR $\sim 1.5 \times 10^3$) indicating binding between the drug and AuNR. Interestingly, the relative decrease was observed to depend upon the nature of the coating (Fig. 2). On addition of Cp_6 , the maximum change in the zeta potential was observed for PAH coated AuNRs and the minimum for PDDAC coated AuNRs. The Soret band of the drug at 400 nm shows a slight red shift in the presence of coated AuNRs, in addition for PAH coated AuNR, it was observed to be

significantly broader. Results obtained from earlier studies indicate that this might be due to aggregation of the drug. The Q-band region of the drug (~660 nm) is convoluted with the L-SPR band of the AuNR and hence it is difficult to ascertain any changes in the band parameters compared to that of the free drug.

The fluorescence properties of the drug were observed to depend significantly upon the nature of the coating on the AuNR. While the PDDAC coating decreases the fluorescence quantum yield by half, it does not significantly affect the fluorescence lifetime. In case of PAH coating a significant quenching of the drug's fluorescence is observed but change in its lifetime is not significant. For CTAB coating significant quenching in both quantum yield and lifetime of the drug is observed. From Table 7.2 we see that polymer (PDDAC & PAH) coatings affect only the radiative rates of the drug but for CTAB coating, both radiative and nonradiative rates decrease significantly. Fluorescence quenching near gold nanoparticles have been studied earlier [202, 205] and it has been observed that quenching results from two effects, a decrease in the transition probability for radiative transitions [202] and due to energy transfer [203]. It has been observed that in certain cases both may be present [204, 205]. Thus the observed quenching of Cp_6 fluorescence in the presence of CTAB coated AuNRs may be attributed to both of these effects. However, no significant changes in the nonradiative rates of the drug in the presence of polymer (PDDAC or PAH) coated AuNRs suggest that the distance between Cp_6 and AuNR surface is large enough (due to the presence of three spacer layers: CTAB, PSS and PDDAC or PAH) to prevent energy transfer between the molecule and the metal. Between PDDAC and PAH coated AuNRs the observed changes in the fluorescence property of the drug were also different due to different magnitudes of decrease in the radiative rates of the drug.

At this point it is worthwhile to look at the chemical structures of the repeating units of the polymers PAH and PDDAC (Fig.7.1). The repeating unit of PAH contains one primary amine group while the repeating unit of PDDAC contains three tertiary

amino group. Cp_6 is expected to bind to these polymers by electrostatic interaction between the carboxyl group of the drug and the amino group of the polymers. It is clear that distances between binding sites will be larger for PDDAC. The zeta potential values of the drug-polymer coated AuNR complex shows that compared to PDDAC coating the PAH coating results in zeta potential values of almost zero for same drug:AuNR ratio indicating that charge neutralization is almost complete for the Cp_6 -PAH-AuNR complex. As a result, the observed shape change of the Soret band of the drug in the absorption spectra as well as its higher decrease in radiative rate may be attributed to the relatively close packing of the drug at the PAH coated AuNR surface.

Another important aspect of this study was to investigate how the photobleaching properties, of an adsorbed photosensitizer, are affected by the surface plasmon of AuNR as it could affect the photodynamic efficacy of the drug. We have observed that the photobleaching of the drug gets significantly reduced when it is bound to these coated AuNRs (Fig. 7.6). In particular the photobleaching rate is suppressed by ~six times in the presence of CTAB and PAH coated AuNRs. This shows that photostability can depend upon the nature of the coated material and hence it is important to choose the coating material accordingly when utilizing these for combined hyperthermia and PDT applications.

7.5 Conclusion

We prepared three types of coated AuNRs with two different aspect ratios. While the zeta potential did not change with changes in aspect ratios, the L-SPR band position changed significantly with changes in the coating material for the larger aspect ratio AuNRs. This has been attributed to the larger sensitivity of larger aspect ratio rods towards the dielectric medium. The binding of a negatively photosensitizer Cp_6 with these AuNRs resulted in coating specific reduction in the zeta potential. The spectroscopic properties of the drug also depended upon the nature of the coating. While the polymer (PDDAC &

PAH) coating affected only the radiative rates of the drug the CTAB coating resulted in decrease of both radiative and nonradiative rates. Interestingly, the decrease in radiative rates was observed to be much higher in presence of PAH coated rods as compared to PDDAC coated rods. The observed changes have been attributed to the difference in the distance between the Cp_6 and the AuNR surface which gets modified with additional layers of coated materials and also to the different chemical structure of the polymers PAH and PDDAC. The nature of the coated material was also observed to modulate the photostability of the drug. However, the effect of changing the L-SPR spectral position did not affected the photophysical and photobleaching properties of the drug.

CHAPTER 8

CONCLUSION

The main objective of the work reported in this thesis was to investigate interaction of organically modified silica nanoparticles (SiNP) and gold nanorods with some dyes of biomedical significance. SiNPs synthesized with 3 amino propyl and/or vinyl silica precursors and coated gold nanorods with their L-SP tuned to and away the absorption peaks of the dyes were used for the studies, while the dyes used were negatively charged polarity sensitive dyes (ANS, TNS and MC540) and photosensitizers (MC540, Cp_6 , PP18, MB and NB).

Photophysical studies on interaction of SiNPs with dyes ANS and TNS, showed significant shifts in the absorption and emission peak positions and enhancement in the fluorescence intensity of dyes in presence of the SiNP-VA in aqueous medium at physiological pH. The results obtained suggest that this was due to a strong electrostatic interaction between the positively charged SiNP-VA and the negatively charged dyes which lead to the suppression of the excited state charge transfer process in the dyes in presence of SiNP-VA, whereas it was absent in case of SiNP-V. This fluorescence was found to be pH dependent and decreased significantly after pH ~ 9.2 which is the pK_a of the amino propyl group. Therefore, this study shows that positively charged amino groups are present on the surface of SiNP-VA are at physiological pH, which is also confirmed by the Zeta potential measurements. In case of MC540 which is also a negatively charged dye, results of the photophysical studies suggest that the excited state photoisomerism process, which is the major non-radiative decay channel, is significantly suppressed due

to its binding to SiNP-VA. The observed enhancement in phototoxicity to cancer cells due to the dye-NP complex is consistent with the earlier observed enhanced singlet oxygen yield of the dye due to suppression of the excited state photoisomerism rate. Thus, these studies suggest that the interaction of SiNP-VA with negatively charged dyes is electrostatic in nature, which leads to significant changes in their excited state properties, suppressing non-radiative decay due to structural changes, enhancing their fluorescence properties and phototoxicity.

Our studies on the absorption and fluorescence properties of the photosensitizer Cp_6 in the presence of SiNP-VA indicated that the interaction is electrostatic in nature leading to significant changes in its acid-base equilibrium. Further, our studies showed that phototoxicity due to Cp_6 complexed to SiNP-VA, to cancer cell lines, was significantly higher as compared to free Cp_6 and was due to the enhanced photostability of the complex. We investigated the suitability of SiNPs as carriers of PP18 in aqueous medium at physiological pH. This was studied spectroscopically, by comparing its conversion to its hydrolytic product Cp_6 , among four nanoparticulate systems: SiNP-V, SiNP-VA, PLGA NP and Liposomes as its carrier. Our results showed that among these, SiNP-V is the most suitable carrier of PP18.

Interaction of negatively charged PSS coated gold nanorods and positively charged dyes MB and NB showed significant changes in the absorption and emission properties of the dyes. For both tuned and detuned cases, two absorption bands were shown in the 550-700 nm regions of the dye-AuNR complex. The high and low energy bands were attributed to the dimeric and monomeric species of the dyes for the detuned condition. However for the tuned condition (i.e. strong coupling regime) the interaction of the L-SP of the AuNRs with the dyes resulted in the formation of high and low energy bands whose splitting increased with increasing dye concentration and then saturated. This was attributed to arise from the coupling of L-SP band with the molecular absorption. Although the fluorescence intensity of the dyes in the presence of increasing

amount of PSS coated AuNRs were observed to be decreased the corresponding lifetimes were observed to increase. This was explained on the basis of the formation of nonfluorescent dimeric species, suppression of the excited state nonradiative decay channels and the influence of the L-SP field.

We also investigated binding of Cp_6 with CTAB, PAH and PDDAC coated rods. Due to binding, while the fluorescence intensity of Cp_6 decreased significantly in all the rods, the lifetime decreased significantly only for the CTAB coated rods. While, the polymer (PDDAC & PAH) coatings affected only the radiative rates of the drug, for CTAB coating, both radiative and nonradiative rates decreased significantly. The observed quenching of Cp_6 fluorescence in the presence of CTAB coated AuNRs was attributed to both, a decrease in the transition probability for radiative transitions and to energy transfer. This is suggested to be due to the difference in the distance between the Cp_6 and the gold surface of the rods, the distance being small in case of CTAB coated rods, due to single layer of CTAB coating, while there are two more coatings, PSS and PDDAC/PAH, in case of PAH and PDDAC coated rods which could prevent energy transfer. Another interesting result was that among the PAH and PDDAC coated rods, a significantly large decrease in quantum yield in presence of PAH coated rods as compared to PDDAC was observed. This has been attributed to the difference in the chemical structures of the two polymers. The photostability of Cp_6 bound to CTAB and PAH coated rods was found to be more as compared to PDDAC coated rods and free Cp_6 which suggests that it also depends upon the nature of the coated material. This study shows that CTAB and PAH coatings may be preferable while utilizing these rods for combined hyperthermia and photodynamic therapy applications.

The results of our studies presented in this thesis show that the conjugation of the photosensitizers with NPs changes their photophysical properties. Since this also affects their biological activity, it is suggested that a thorough study of the photophysical

properties of the photosensitizers conjugated to the NPs should be carried out before using such formulations for therapeutic applications.

REFERENCES

-
- 1 P. K. Sarkar and A. K. Chaudhery, “Ayurvedic bhasma: the most ancient applications of Nanomedicine”, *J. Scientific and Indian Res.* **69**, 909 (2010).
 - 2 T. K. Bhowmick, A. K. Suresh, S. G. Kane, A. C. Joshi and J. R. Bellare, “Physicochemical characterization of an Indian traditional medicine, Jasada Bhasma: detection of nanoparticles containing non-stoichiometric zinc oxide”, *J. Nanopart. Res.* **11**, 655 (2009).
 - 3 E. L. Armitage, “Stained Glass: History, Technology and Practice”, Publ. C. T. Branford Co, Newton, MA (1959).
 - 4 R. P. Feynman, “There’s plenty of room at the bottom”, *Engg. Sci.* **23**, 22 (1960).
 - 5 N. Taniguchi, “On the basic concept of 'Nano-Technology'”, *Proc. Intl. Conf. Prod. Eng.*, Tokyo, Part II, **18** (1974).
 - 6 K. E. Drexler, “Molecular Engineering: An approach to the development of general capabilities for molecular manipulation”. *Proc. Natl. Acad. Sci., U. S. A.* **78**, 5275 (1981).
 - 7 K. E. Drexler, “Engines of Creation: The coming era of nanotechnology”. Anchor Books, New York (1986).
 - 8 A. Sharma, J. Bellare and A. Sharma (Eds.), “Advances in nanoscience & nanotechnology” (2004).
 - 9 J. U. Menon, P. Jadeja, P. Tambe, K. Vu, B. Yuan and K. T. Nguyen, “Nanomaterials for photo-based diagnostic and therapeutic applications”, *Theranostics* **3**, 152 (2013).
 - 10 L. Dykmana and N. Khlebtsov, “Gold nanoparticles in biomedical applications: recent advances and perspectives”, *Chem. Soc. Rev.* **41**, 2256 (2012).
 - 11 R. K. Jain and T. Stylianopoulos, “Delivering nanomedicine to solid tumors”, *Nat. Rev. Clin. Oncol.* **7**, 653 (2010).

-
- 12 S. Parveen, R. Misra and S. K. Sahoo, “Nanoparticles: a boon to drug delivery, therapeutics, diagnostics and imaging”, *Nanomedicine: Nanotechnology, biology and medicine* **8**, 147 (2012).
- 13 M. Gaumet, A. Vargas, R. Gurny and F. Delie, “Nanoparticles for drug delivery: The need for precision in reporting particle size parameters”, *Review. Eur. J. Pharm. Biopharm.* **69**, 1 (2008).
- 14 M. Ferrai, “Cancer nanotechnology: Opportunities and challenges,” *Nat. Rev. Cancer* **5**, 161 (2005).
- 15 N. L. Rosi and C. A. Mirkin, “Nanostructures in biodiagnostics”, *Chem. Rev.* **105**, 1547 (2005).
- 16 M. Han, X. Gao, J. Z. Su and S. Nie, “Quantum-dot-tagged microbeads for multiplexed optical coding of biomolecules”, *Nature Biotechnology* **19**, 631 (2001).
- 17 A. Valizadeh, H. Mikaeili, M. Samiei, S. M. Farkhani, N. Zarghami, M. Kouhi, A. Akbarzadeh and S. Davaran, “Quantum dots: synthesis, bioapplications and toxicity”, *Nanoscale Research Lett.* **7**, 480 (2012).
- 18 E. C. Dreaden, A. M. Alkilany, X. Huang, C. J. Murphy and M. A. El-Sayed, “The golden age: gold nanoparticles for biomedicine”, *Chem. Soc. Rev.* **41**, 2740 (2012).
- 19 A. J. Wilson and K. A. Willets, “Surface-enhanced Raman scattering imaging using noble metal nanoparticles, *Wiley Interdiscip Rev. Nanomed. Nanobiotech.* **5**, 180 (2013).
- 20 I. Roy, “ORMOSIL nanoparticles. Nanomedicine approach for drug/gene delivery to the brain”, book chapter 5 in “Nanotechnology in health care” S. K. Sahoo (Ed.), Pan Stanford publishing (2012).
- 21 M. J. Rathbone, J. Hadgraft, M. S. Roberts and M. E. Lane (Eds.), “Modified release drug delivery technology” in *Drugs and the pharmaceutical sciences*, Second ed., vol 1 and 2, Marcel Dekker, New York (2008).

-
- 22 F. Perche and V. P. Torchilin, “Recent trends in multifunctional liposomal nanocarriers for enhanced tumor targeting”, Review article in *J. Drug delivery* **32**, 1 (2013).
- 23 J. M. Chan, P. M. Valencia, L. Zhang, R. Langer and O. C. Farokhzad, Chapter 11, “Polymeric nanoparticles for drug delivery”, S. R. Grobmyer and B. M. Moudgil (Eds.) in *Cancer nanotechnology, methods in molecular biology*, Springer Sci. + business media, LLC 163 (2010).
- 24 M. K. Yu, J. Park and S. Jon, “Targeting strategies for multifunctional nanoparticles in cancer imaging and therapy”, *Theranostics* **2**, 1 (2012).
- 25 T. K. Jain, I. Roy, T. K. De and A. N. Maitra, “Nanometer silica particles encapsulating active compounds: a novel ceramic drug carrier”, *J. Am. Chem. Soc.* **120**, 11092 (1998).
- 26 Y. R. Chiu, W. J. Ho, J. S. Chao and C. J. Yuan, “Enzyme-encapsulated silica nanoparticle for cancer chemotherapy”, *J. nanoparticle res.* **14**, 829 (2012).
- 27 F. Barandeh, P. L. Nguyen, R. Kumar, G. J. Lacobucci, M. L. Kuznicki, A. Kosterman, E. J. Bergey, P. N. Prasad and S. Gunawardena, “Organically modified silica nanoparticles are biocompatible and can be targeted to neurons in vivo”, *PLOS one* **7**, 29424 (2012).
- 28 R. Kumar, I. Roy, Tymish, Y. Ohulchanskyy, L. A. Vathy, E. J. Bergey, M. Sajjad and P. N. Prasad, “In vivo biodistribution and clearance studies using multimodal ORMOSIL nanoparticles”, *ACS Nano* **4**, 699 (2010).
- 29 A. J. Wilson and K. A. Willets, “Surface-enhanced Raman scattering imaging using noble metal nanoparticles”, *Wiley Inter. Discip. Rev. Nanomed. Nanobiotechnol.* **5**, 180 (2013).
- 30 U. Kreibig and M. Vollmer, “Optical properties of metal clusters”, *Springer Series in Material Science*, 25 (1995).

-
- 31 C. Barbé, J. Bartlett, L. Kong, K. Finnie, H. Q. Lin, M. Larkin, S. Calleja, A. Bush and G. Calleja, "Silica particles: a novel drug-delivery system", *Adv. Mat.* **16**, 1959 (2004).
- 32 G. W. Scherer and C. J. Brinker, "Sol-Gel Science", Academic Press, New York (1990).
- 33 W. Stöber, A. Fink and E. Bohn, "Controlled growth of monodispersed spheres in the micron size range", *J. Colloid and Interface Sci.* **26**, 62 (1968).
- 34 K. S. Rao, K. E. Hami, T. Kodaki, K. Matsushige and K. Makino, "A novel method for synthesis of silica nanoparticles", *J. Colloid and Interface Sci.* **289**, 125 (2005).
- 35 S. Santra, P. Zhang, K. Wang, R. Tapeç and W. Tan, "Conjugation of biomolecules with luminophore-doped silica nanoparticles for photostable biomarkers", *Anal. Chem.* **73**, 4988 (2001).
- 36 S. H. Wu, C. Y. Mou and H. P. Lin, "Synthesis of mesoporous silica nanoparticles", *Chem. Soc. Rev.* **42**, 3862 (2013).
- 37 H. Guo, H. Qian, S. Sun, D. Sun, H. Yin, X. Cai, Z. Liu, J. Wu, T. Jiang and X. Liu, "Hollow mesoporous silica nanoparticles for intracellular delivery of fluorescent dye", *Chem. Central J.* **5**, 1 (2011).
- 38 T. Xia, M. Kovichich, M. Liang, H. Meng, S. Kabehie, S. George, J. I. Zink and A. E. Nel, "Polyethyleneimine coating enhances the cellular uptake of mesoporous silica nanoparticles and allows safe delivery of siRNA and DNA constructs", *ACS Nano* **3**, 3273 (2009).
- 39 J. M. Rosenholm, E. Peuhu, L. T. Bate-Eya, J. E. Eriksson, C. Sahlgren and M. Lindén, "Cancer-cell-specific induction of apoptosis using mesoporous silica nanoparticles as drug-delivery vectors", *Small* **6**, 1234 (2010).
- 40 T. K. Jain, I. Roy, T. K. De and A. N. Maitra, "Nanometer silica particles encapsulating active compounds: a novel ceramic drug carrier", *J. Am. Chem. Soc.* **120**, 11092 (1998).

-
- 41 Y. R. Chiu, W. J. Ho, J. S. Chao and C. J. Yuan, "Enzyme-encapsulated silica nanoparticle for cancer chemotherapy", *J. nanoparticle research* **14**, 829 (2012).
- 42 R. E. Yanes and F. Tamanoi, "Development of mesoporous silica nanomaterials as a vehicle for anticancer drug delivery", *Therapeutic delivery* **3**, 389 (2012).
- 43 C. Kneuer, M. Sameti, U. Bakowsky, T. Schiestel, H. Schirra, H. Schmidt and C. M. Lehr, "A nonviral DNA delivery system based on surface modified silica-nanoparticles can efficiently transfect cells in vitro", *Bioconjug. Chem.* **11**, 926 (2000).
- 44 S. Das, T. K. Jain and A. Mitra, "Inorganic-organic hybrid nanoparticles from n-octyl triethoxy silane", *J. Colloid and Interface Sci.* **252**, 82 (2002).
- 45 I. Roy, T. Y. Ohulchanskyy, D. J. Bharali, H. E. Pudavar, R. A. Mistretta, N. Kaur and P. N. Prasad, "Optical tracking of organically modified silica nanoparticles as DNA carriers: A nonviral, nanomedicine approach for gene delivery", *Proc. Natl. Acad. Sci. U.S.A.* **102**, 279 (2005).
- 46 X. Wang, S. Yao, H. Y. Ahn, Y. Zhang, M. V. Bondar, J. A. Torres and K. D. Belfield, "Folate receptor targeting silica nanoparticle probe for two-photon fluorescence bioimaging", *Biomed. Opt. Express.* **1**, 453 (2010).
- 47 D. J. Bharali, I. Klejbor, E. K. Stachowiak, P. Dutta, I. Roy, N. Kaur, E. J. Bergey, P. N. Prasad and M. K. Stachowiak, "Organically modified silica nanoparticles: a nonviral vector for in vivo gene delivery and expression in the brain", *Proc. Natl. Acad. Sci. U. S. A.* **102**, 11539 (2005).
- 48 Y. Zhang, J. Wang, X. Bai, T. Jiang, Q. Zhang and S. Wang, "Mesoporous silica nanoparticles for increasing the oral bioavailability and permeation of poorly water soluble drugs", *Mol. Pharm.* **9**, 505 (2012).
- 49 J. Qian, Q. L. Chen, F. H. Cai, S. K. Kong, H. P. Ho and S. He, "Quantum-dots-doped ORMOSIL nanoparticles as optical probes for total internal reflection fluorescence imaging of cancer cells", *IEEE J. Select. Topics Quant. Elect.* **15**, 1374 (2009).

-
- 50 J. Qian, D. Wang, F. Cai, Q. Zhan, Y. Wang and S. He, "Photosensitizer encapsulated organically modified silica nanoparticles for direct two-photon photodynamic therapy and in vivo functional imaging", *Biomaterials* **33**, 4851 (2012).
- 51 I. Roy, T. Y. Ohulchanskyy, H. E. Pudavar, E. J. Bergey, A. R. Oseroff, J. Morgan, T. J. Dougherty and P. N. Prasad, "Ceramic-based nanoparticles entrapping water-insoluble photosensitizing anticancer drugs: a novel drug-carrier system for photodynamic therapy", *J. Am. Chem. Soc.* **125**, 7860 (2003).
- 52 E. Hutter and J. H. Fendler, "Exploitation of localized surface plasmon resonance", *Adv. Mater.* **16**,1685 (2004).
- 53 S. Eustis and M. A. El- Sayed, "Why gold nanoparticles are more precious than pretty gold: Noble metal surface plasmon resonance and its enhancement of the radiative and nonradiative properties of nanocrystals of different shapes", *Chem. Society Reviews* **35**, 209 (2006).
- 54 T. A. Klar, "Biosensing with plasmonic nanoparticles. Chap.8 in "Nanophotonics with surface plasmons", V. M. Shalaev and S. Kawata (Eds.), Pub. Elsevier B.V. in 'Advances in the nano-optics and nano-photonics' series (2007).
- 55 X. Huang and M. A. El-Sayed, "Gold nanoparticles: Optical properties and implementations in cancer diagnosis and photothermal therapy", *Review, J. Adv. Res.* **1**, 13 (2010).
- 56 J. Homola, S. Yee and G. Gauglitz, "Surface plasmon resonance sensors: review", *Sensors and Actuators B* **54**, 3 (1999).
- 57 R. C. Johnson, J. Li, J. T. Hupp and G. C. Schatz, "Hyper-Rayleigh scattering studies of silver, copper, and platinum nanoparticle suspensions", *Chem. Phys. Lett.* **356**, 534 (2002).
- 58 I. Alfred, M. D. Sherman and M. T. Pogossian, "Cancer lymph-node concentration of radioactive colloidal gold following interstitial injection", *Cancer* **6**, 1238 (1953).

-
- 59 Y. Pan, A. Leifert, D. Ruau, S. Neuss, J. Bornemann, G. Schmid and W. Brandau, "Gold nanoparticles of diameter 1.4 nm trigger necrosis by oxidative stress and mitochondrial damage", *Small* **5**, 2067 (2009).
- 60 C. J. Murphy, A. M. Gole, J. W. Stone, P. N. Sisco, A. M. Alkilany, E. C. Goldsmith and S. C. Baxter, "Gold nanoparticles in biology: Beyond toxicity to cellular imaging", *Acc. Chem. Res.* **41**, 1721 (2008).
- 61 P. K. Jain, K. S. Lee, I. H. El-Sayed and M. A. El-Sayed, "Calculated absorption and scattering properties of gold nanoparticles of different size, shape and composition: applications in biological imaging and biomedicine", *J. Phys. Chem. B* **110**, 7238 (2006).
- 62 Y. W. Wang, X. Y. Xie, X. D. Wang, G. Ku and K. L. Gill, "Photoacoustic tomography of a nanoshell contrast agent in the in vivo rat brain", *Nano. Lett.* **4**, 1689 (2004).
- 63 S. Lal, S. E. Clare and N. J. Halas, "Nanoshell-enabled photothermal cancer therapy: impending clinical impact", *Acc. Chem. Res.* **41**, 1842 (2008).
- 64 C. Sönnichsen, T. Franzl, T. Wilk, G. Von Plessen, J. Feldmann, O. Wilson and P. Mulvaney, "Drastic reduction of plasmon damping in gold nanorods", *Phys. Rev. Lett.* **88** 77402 (2002).
- 65 X. Huang, I. H. El-Sayed, W. Qian, M. A. El-Sayed, "Cancer cell imaging and photothermal therapy in the near-infrared region by using gold nanorods", *J. Am. Chem. Soc.* **128**, 2115 (2006).
- 66 R. Gans, "The form of ultramicroscopic gold particles", *Ann. Physik.* **37**, 881 (1912).
- 67 S. Link and M. A. El-Sayed, "Optical properties and ultrafast dynamics of metallic nanocrystals", *Annu. Rev. Phys. Chem.* **54**, 331(2003).
- 68 S. Link, C. Burda, M. B. Mohamed, B. Nikoobakht, M. A. El-Sayed, "Laser photothermal melting and fragmentation of gold nanorods: energy and laser pulse-width dependence", *J. Phys. Chem. A* **103**, 1165 (1999).

-
- 69 S. Link, C. Burda, B. Nikoobakht, M. A. El-Sayed, "Laser-induced shape changes of colloidal gold nanorods using femtosecond and nanosecond laser pulses", *J. Phys. Chem. B* **104**, 6152 (2000).
- 70 A. Kyrsting, P. M. Bendix and L. B. Oddershede, "Photothermal heating of optically trapped gold nanoparticles quantized using controlled vesicle cargo release", in *Optical trapping and optical micromanipulation IX*, K. Dholakia and G. C. Spalding (Eds.), *Proc. SPIE*, 8458.
- 71 Y. S. Chen, W. Frey, S. Kim, P. Kruizinga, K. Homan and S. Emelianov, "Silica-coated gold nanorods as photoacoustic signal nano-amplifiers", *Nano Lett.* **11**, 348 (2011).
- 72 F. Ratto, P. Matteini, F. Rossi, L. Menabuoni, N. Tiwari, S. K. Kulkarni and R. Pini, "Photothermal effects in connective tissues mediated by laser-activated gold nanorods", *Nanomedicine* **5**, 143 (2009).
- 73 T. Kawano, Y. Niidome, T. Mori, Y. Katayama and T. Niidome, "PNIPAM gel-coated gold nanorods for targeted delivery responding to a near-infrared laser", *Bioconjugate Chem.* **20**, 209 (2009).
- 74 J. A. Li, D. Day and M. Gu, "Ultra-low energy threshold for cancer photothermal therapy using transferrin-conjugated gold nanorods", *Adv. Mater.* **20**, 3866 (2008).
- 75 B. Nikoobakht, M. A. El-Sayed, "Preparation and growth mechanism of gold nanorods (NRs) using seed-mediated growth method", *Chem. Mater.* **15**, 1957 (2003).
- 76 X. C. Jiang and M. P. Pileni, "Gold nanorods: Influence of various parameters as seeds, solvent, surfactant on shape control", *Colloids and Surfaces A: Physicochemical and engineering aspects*, **295**, 228 (2007).
- 77 N. R. Jana, L. Gearheart and C. J. Murphy, "Seed-mediated growth approach for shape-controlled synthesis of spheroidal and rod-like gold nanoparticles using a surfactant template", *Adv. Mater.* **13**, 1389 (2001).

-
- 78 P. R. Sajanlal, T. S. Sreepasad, A. K. Samal and T. Pradeep, “Anisotropic nanomaterials: structure, growth, assembly, and functions”, *Nano Reviews* **2**, 5883 (2011).
- 79 B. Nikoobakht and M. A. El-Sayed, “Evidence for bilayer assembly of cationic surfactants on the surface of gold nanorods”, *Langmuir* **17**, 6368 (2001).
- 80 A. M. Alkilany, P. K. Nagaria, C. R. Hexel, T. J. Shaw, C. J. Murphy and M. D. Wyatt, “Cellular uptake and cytotoxicity of gold nanorods: molecular origin of cytotoxicity and surface effects”, *Small* **5**, 701 (2009).
- 81 Z. Zhang, J. Wang and C. Chen, “Gold nanorods based platforms for light-mediated theranostics”, *Review, Theranostics* **3**, 223 (2013).
- 82 J. R. Lakowicz, “Radiative decay engineering: Biophysical and biomedical applications”, *Anal. Biochem.* **298**, 1 (2001).
- 83 T. L. Chang and H. C. Cheung, “A model for molecules with twisted intramolecular charge transfer characteristics: solvent polarity effect on the nonradiative rates of dyes in a series of water—ethanol mixed solvents”, *Chem. Phys. Lett.* **173**, 343 (1990).
- 84 K. Sahu, S. K. Mondal, S. Ghosh, D. Roy and K. Bhattacharyya, “Temperature dependence of solvation dynamics and anisotropy decay in a protein: ANS in bovine serum albumin”, *J. Chem. Phys.* **124**, 124909 (2006).
- 85 K. G. David and F. Sieber, “Merocyanine 540-sensitized photoinactivation of soluble and membrane-bound enzymes in LI 210 leukemia cells”, *Cancer research* **50**, 7765 (1990).
- 86 A. S. Verkman, “Mechanism and kinetics of merocyanine 540 binding to phospholipid membranes”, *Biochemistry* **26**, 4050 (1987).
- 87 L. G. S. Brooker, A. C. Craig, D. W. Heseltine, P. W. Jenkins, L. L. Lincoln and J. R. Platt, “Wavelength formulas and configuration interaction in Brooker dyes and chain molecules”, *J. Chem. Phys.* **25**, 80 (1956).

-
- 88 M. R. Langne and S. W. Hui, "Merocyanine 540 as a fluorescence indicator for molecular packing stress at the onset of lamellar-hexagonal transition of phosphatidylethanolamine bilayers", *Biochim. Biophys. Acta.* **1415**, 323 (1999).
- 89 M. Krieg, "Singlet oxygen production and fluorescence yields of merocyanine 540: a comparative study in solution and model membrane systems", *Biochim. Biophys. Acta.* **1105**, 333 (1992).
- 90 J. Han and K. Burgess, "Fluorescent Indicators for Intracellular pH", *Chem. Rev.* **110**, 2709 (2010).
- 91 A. Datta, A. Dube, B. Jain, A. Tiwari and P. K. Gupta, "The effect of pH and surfactant on the aggregation behavior of chlorin p_6 : A fluorescence spectroscopic study", *Photochem. Photobiol.* **75**, 488 (2002).
- 92 W. H. Ni, H. J. Chen, J. Su, Z. H. Sun, J. F. Wang and H. K. Wu, "Effects of dyes, gold nanocrystals, pH, and metal ions on the plasmonic and molecular resonance coupling", *J. Am. Chem. Soc.* **132**, 4806 (2010).
- 93 Y. W. Hao, H. Y. Wang, Y. Jiang, Q. D. Chen, K. Ueno, W. Q. Wang, H. Misawa and H. B. Sun, "Hybrid-state dynamics of gold nanorods/dye J-aggregates under strong coupling", *Angew. Chem., Int. Ed. Engl.* **50**, 7824 (2011).
- 94 W. Ni, Z. Yang, H. Chen, L. Li and J. Wang, "Coupling between molecular and plasmonic resonances in freestanding dye-gold nanorod hybrid nanostructures", *J. Am. Chem. Soc.* **130**, 6692 (2008)
- 95 W.-S. Kuo, C.-N. Chang, Y.-T. Chang, M. -H. Yang, Y. -H. Chien, S. -J. Chen and C.-S. Yeh, "Gold nanorods in photodynamic therapy, as hyperthermia agents, and in near-infrared optical imaging", *Angew. Chem. Int. Ed.* **49**, 2711 (2010).
- 96 Y. Zhang, D. Xu, W. Li, J. Yu and Y. Chen, "Effect of size, shape, and surface modification on cytotoxicity of gold nanoparticles to human hep-2 and canine MDCK cells", *J. Nanomaterials* **2012**, 375496 (2012).

-
- 97 R. K. Sharma, S. Das and A. Maitra, "Surface modified ormosil nanoparticles", *J. Colloid Interface Sci.* **227**, 342 (2004).
- 98 T. K. Sau and C. J. Murphy, "Seeded high yield synthesis of short Au nanorods in aqueous solution", *Langmuir* **20**, 6414(2004).
- 99 M. M. Yallapu, B. K. Gupta, M. Jaggi and S. C. Chauhan, "Fabrication of curcumin encapsulated PLGA nanoparticles for improved therapeutic effects in metastatic cancer cells", *J. Colloid Interface Sci.* **35** (2010)19.
- 100 S. Batzri and E. D. Korn, "Single bilayer liposomes prepared without sonication", *Biochim. Biophys. Acta.* **16**, 1015 (1973).
- 101 A. Moscho, O. Orwar, D. T. Chiu, B. P. Modi and R. W. Zare, "Rapid preparation of giant unilamellar vesicles", *Proc. Natl. Acad. Sci. USA.* **93**, 11443 (1996).
- 102 T. Mosman, "Rapid colorimetric assay for cellular growth and survival: Application to proliferation and cytotoxicity assays", *J. Immunol. Meth.* **65**, 55 (1983).
- 103 C. J. Orendorff and C. J. Murphy, "Quantitation of metal content in the silver assisted growth of gold nanorods", *J. Phys. Chem. B* **110**, 3990 (2006).
- 104 S. Maiti, U. Haupts and W. W. Webb, "Fluorescence correlation spectroscopy: Diagnostics for sparse molecules", *Proc. Natl. Acad. Sci.* **94**, 11753 (1997).
- 105 N. Thompson, "Topics in fluorescence spectroscopy. Vol. I: Techniques," Joseph R. Lakowicz (Ed.), Plenum Press, N. York (2002).
- 106 D. V. O'Conner and D. Phillips, "Time correlated single photon counting", Academic press (1984).
- 107 J. M. Hicks, M. Vandersall, Z. Babarogic and K. B. Eisenthal, "The dynamics of barrier crossings in solution: The effect of a solvent polarity-dependent barrier", *Chem. Phys. Lett.* **116**, 18 (1985).

-
- 108 D. Zhong, S. K. Pal and A. H. Zewail, "Femtosecond studies of protein-DNA binding and dynamics: Histone I", *Chem. Phys. Chem.* **2**, 219 (2001).
- 109 W. Kirk, E. Kurian and F. Prendergast, "Characterization of the sources of protein-ligand affinity: 1-sulfonato-8-(1') anilino-naphthalene binding to intestinal fatty acid binding protein", *Biophys. J.* **70**, 69 (1996).
- 110 D. Matulis and R. E. Lovrien, "1-Anilino-8-naphthalene sulfonate anion-protein binding depends primarily on ion pair formation", *Biophys. J.* **74**, 422 (1998).
- 111 D. Sukul, S. Sen, P. Dutta and K. Bhattacharyya, "Photoisomerisation of merocyanine 540 in polymer-surfactant aggregate", *Proc. Ind. Acad. Sci. (Chem. sci.)* **114**, 501 (2002).
- 112 M. Vedamuthu, S. Singh, O. Onganer, D. R. Bessire, M. Yin, E. L. Quitevis and G. W. Robinson, "Universality in isomerization reactions in polar solvents", *J. Phys. Chem.* **100** 11907, (1996).
- 113 K. B. Eisenthal, "Liquid interfaces probed by second-harmonic and sum-frequency spectroscopy", *Chem. Rev.* **96**, 1343 (1996).
- 114 J. M. O. Brien, D. K. Gaffney, T. P. Wang and F. Sieber, "Merocyanine 540 sensitized photoinactivation of enveloped viruses in blood products: Site and mechanism of phototoxicity", *Blood* **80**, 277 (1992).
- 115 K. G. David and F. Sieber, "MC540 sensitized photoinactivation of soluble and membrane-bound enzymes in LI 210 leukemia cells", *Cancer research* **50**, 7765 (1990).
- 116 G. Salama and M. Morad, "Merocyanine 540, as an optical probe of transmembrane electrical activity in the heart", *Science* **191**, 485 (1976).
- 117 P. I. Lelkes and I. R. Miller, " Perturbations of membrane structure by optical probes: II. Differential scanning calorimetry of dipalmitoyllecithin and its analogs interacting with Merocyanine 540", *Membr. Biol.* **54**, 141 (1980).

-
- 118 P. Williamson, K. Mattocks and R. A. Schlegel, "Merocyanine 540, a fluorescent probe sensitive to lipid packing", *Biochim. Biophys. Acta* **732**, 387 (1983).
- 119 P. R. Dragsten and W. W. Webb, "Mechanism of the membrane potential sensitivity of the fluorescent membrane probe merocyanine 540", *Biochemistry* **17**, 5228 (1978).
- 120 M. Hoebeke, A. Seret, J. Piette and A. Van. de Vorst, "Singlet oxygen production and photoisomerization: two competitive processes for merocyanine 540 irradiated with visible light", *J. Photochem. Photobiol. B* **1**, 437 (1988).
- 121 K. Das, B. Jain and H. S. Patel, "Hydrogen bonding properties of coumarin 151, 500, and 35: The effect of substitution at the 7-amino position", *J. Phys. Chem. A* **110**, 1698 (2006).
- 122 K. Das, A. Uppal, B. Jain, B. Bose and P. K. Gupta, "Light induced toxicity of merocyanine-540-silica nanoparticle complex", *J. Nanosci. Nanotech.* **9**, 1 (2009).
- 123 S. Ong, X. Zhao and K. B. Eisenthal, "Polarization of water molecules at a charged interface: second harmonic studies of the silica/water interface", *Chem. Phys. Lett.* **191**, 327 (1992).
- 124 R. P. Bagwe, L. R. Hilliard and W. Tan, "Surface modification of silica nanoparticles to reduce aggregation and nonspecific binding", *Langmuir* **22**, 4357 (2006).
- 125 P. Dutta, S. Sen, S. Mukherjee and K. Bhattacharyya, "Solvation dynamics of TNS in polymer (PEG)-surfactant (SDS) aggregate", *Chem. Phys. Lett.* **359**, 15 (2002).
- 126 T. K. Das and S. Mazumdar, "Effect of adriamycin on the boundary lipid structure of cytochrome C oxidase: Picosecond time-resolved fluorescence depolarization studies", *Biophys. Chem.* **86**, 15 (2000).
- 127 D. Banerjee, S. K. Srivastava and S. K. Pal, "Spectroscopic studies on ligand-enzyme interactions: Complexation of alpha-Chymotrypsin by 4',6-diamidino-2-phenylindole (DAPI)", *J. Phys. Chem. B* **112**, 1828 (2008).
- 128 Y. Jin, S. Kannan, M. Wu and J. X. Zhao, "Toxicity of luminescent silica nanoparticles to living cells", *Chem. Res. Toxicol.* **20**, 1126 (2007).

-
- 129 W. Lin, Y.-W. Huang, X.-D. Zhou and Y. Ma, "In vitro toxicity of silica nanoparticles in human lung cancer cells", *Toxicol. & Appl. Pharmac.* **217**, 252 (2006).
- 130 R. K. Pandey, L. N. Goswami, Y. Chen, A. Gryshuk, J. R. Missert, A. Oseroff and T. J. Dougherty, "Nature: a rich source for developing multifunctional agents. Tumor-imaging and photodynamic therapy", *Lasers Surg. Med.* **38**, 445 (2006).
- 131 M. Sharma, A. Dube, H. Bansal and P. K. Gupta, "Effect of pH on uptake and photodynamic action of chlorin p_6 on human colon and breast adenocarcinoma cell lines", *Photochem. Photobiol. Sci.* **3**, 231 (2004).
- 132 A. Dube, S. Sharma and P. K. Gupta, "Evaluation of chlorin p_6 for photodynamic treatment of squamous cell carcinoma in the hamster cheek pouch model", *Oral Oncol.* **42**, 77 (2006).
- 133 Y. Matsumura and H. Maeda, "A new concept for macromolecular therapeutics in cancer chemotherapy: Mechanism of tumoritropic accumulation of proteins and the antitumor agent smancs", *Cancer. Res.* **46**, 6387 (1986).
- 134 P. P. Mishra, J. Bhatnagar and A. Datta, "Fluorescence monitoring of pH dependent complexation of chlorin p_6 with surfactants", *Chem. Phys. Lett.* **386**, 156 (2004).
- 135 P. P. Mishra, J. Bhatnagar and A. Datta, "The interplay of hydrophobic and electrostatic effects in the surfactant-induced aggregation/ deaggregation of chlorin p_6 ", *J. Phys. Chem. B* **109**, 24225 (2005).
- 136 K. Das, B. Jain, A. Dube and P. K. Gupta, "pH dependent binding of chlorin p_6 with phosphatidylcholine liposomes: Comparison between one and two-photon excited fluorescence" *Chem. Phys. Lett.* **401**, 185 (2005).
- 137 P. P. Mishra, R. Adhikary, P. Lahiri and A. Datta, "Chlorin p_6 as a fluorescent probe for the investigation of surfactant-cyclodextrin interactions", *Photochem. Photobiol. Sci.*, **5**, 741 (2006).

-
- 138 S. Patel and A. Datta, "pH Effect on the binding of chlorin derivatives with Cremophor EL, a potential dye delivery vehicle", *Chem. Phys. Lett.* **413**, 31 (2005).
- 139 O. H. Lowry, N. J. Rosebrough, A. L. Farr and R. J. Randall, "Protein measurement with the folin phenol reagent", *J. Biol. Chem.* **193**, 265 (1951).
- 140 S. Patel and A. Datta, "Steady state and time-resolved fluorescence investigation of the specific binding of two Chlorin derivatives with human serum albumin", *J. Phys. Chem. B* **111**, 10557 (2007).
- 141 A. Brandis, O. Mazor, E. Neumark, V. Rosenbach-Belkin, Y. Salomon and A. Scherz, "Novel water-soluble bacteriochlorophyll derivatives for vascular-targeted photodynamic therapy: synthesis, solubility, phototoxicity and the effect of serum proteins", *Photochem. Photobiol.* **81**, 983 (2005).
- 142 N. Shirasu, S. O. Nam and M. Kuroki, "Tumor-targeted photodynamic therapy" *Anticancer Res.* **33**, 2823 (2013).
- 143 M Kotulska, J Kulbacka and J Saczko, "Advances in photodynamic therapy assisted by electroporation", *Review, Curr Drug Metab.***14**, 309 (2013).
- 144 J. G. Levy, "Photosensitizers in photodynamic therapy", *Semin Oncol.* **21**, 4 (1994).
- 145 R Asano, A Nagami, Y Fukumoto, F Yazama, H Ito, I Sakata and A Tai, "Synthesis and biological evaluation of new chlorin derivatives as potential photosensitizers for photodynamic therapy", *Bioorg Med Chem.* **21**, 2298 (2013).
- 146 R. K. Chowdhary, I. Sharif, N. Chansarkar, D. Dolphin, L. Ratkay, S. Delaney and H. J. Meadows, "Correlation of photosensitizer delivery to lipoproteins and efficacy in tumor and arthritis mouse models; comparison of lipid-based and Pluronic P123 formulations", *Pharm Pharm Sci.* **6**, 198 (2003).
- 147 S. Wang, W. Fan, G. Kim, H. J. Hah, Y. E. Lee, R. Kopelman, M. Ethirajan, A. Gupta, L. N. Goswami, P. Pera, J. Morgan and R. K. Pandey, "Novel methods to

incorporate photosensitizers into nanocarriers for cancer treatment by photodynamic therapy”, *Lasers Surg Med.* **43**, 686 (2011).

148 L. Tang and J. Cheng, “Nonporous Silica Nanoparticles for Nanomedicine Application” *Nano Today* **8**, 290 (2013).

149 H. Eshghi, A. Sazgarnia, M. Rahimizadeh, N. Attaran, M. Bakavoli and S. Soudmand, “Protoporphyrin IX-gold nanoparticle conjugates as an efficient photosensitizer in cervical cancer therapy”, *Photodiagnosis Photodyn Ther.* **10**, 304 (2013).

150 D. Luo, E. Han, N. Belcheva and W. M. Saltzman, “A self-assembled, modular DNA delivery system mediated by silica nanoparticles” *J Control Release* **95**, 333 (2004).

151 B. Jain, A. Uppal and P. K. Gupta and K. Das, “Interaction of ANS and TNS with Organically Modified Silica Nanoparticles in Aqueous Media”, *Adv. Sci. Lett.* **3**, 225 (2010).

152 S. Sharma, A. Dube, B. Bose and P. K. Gupta, “ Pharmacokinetics and phototoxicity of purpurin 18 in human colon carcinoma cells using liposomes as delivery vehicles”, *Cancer Chemother. Pharmacol.* **57**, 500 (2006).

153 H. M. Wu, N. Chen, Z. M. Wu, Z. L. Chen and Y. J. Yan, “Preparation of photosensitizer-loaded PLLA nanofibers and its anti-tumor effect for photodynamic therapy in vitro”, *J. Biomater Appl.* **27**, 773 (2013).

154 N. Drogat, C. Gady, R. Granet and V. Sol, “Design and synthesis of water-soluble polyaminated chlorins and bacteriochlorins - With near-infrared absorption”, *Dyes and Pigments* **98**, 609 (2013).

155 J. K. Hooper, T. W. Sery and N. Yamamoto, “Photodynamic sensitizers from chlorophyll: purpurin 18 and chlorin p_6 ”, *Photochem. Photobiol.* **4**, 579 (1988).

-
- 156 B. Jain, A. Uppal, P. K. Gupta and K. Das, "Spectroscopic investigations on the binding of the photosensitizer chlorin p_6 with amine modified silica nanoparticles in aqueous media", *Photochem. Photobiol.* **85**, 927 (2009).
- 157 P. P. Mishra and A. Datta, "Difference in the effects of surfactants and albumin on the extent of deaggregation of purpurin 18, a model of hydrophobic photosensitizer", *Biophys. Chem.* **121**, 224 (2006).
- 158 A. Aguilera and R. W. Murray, "Monolayer-protected clusters with fluorescent dicyanide ligands", *Langmuir* **16**, 5949 (2000).
- 159 J. Hu, J. Zhang, F. Liu, K. Kittredge, J. K. Whitesell and M. A. Fox, "Quantitative photochemical reactivity in a self-assembled monolayer on a colloidal gold star", *J. Am. Chem. Soc.* **123**, 1464 (2001).
- 160 B. I. Ipe, K. G. Thomas, S. Barazzouk, S. Hotchandani and P. V. Kamat, "Photo-induced charge separation in a fluorophore-gold assembly", *J. Phys. Chem. B* **106**, 18 (2002).
- 161 T. Huang, R. W. Murray, "Quenching of $[\text{Ru}(\text{bpy})_3]^{2+}$ fluorescence by binding to Au nanoparticles", *Langmuir* **18**, 7077 (2002).
- 162 T. Gu, J. K. Whitesell, M. A. Fox, "Energy transfer from a surface-bound arene to the gold core in fluorenylalkane-1-thiolate monolayer protected gold clusters", *Chem. Mater.* **15**, 1358 (2003).
- 163 M. Montalti, L. Prodi, N. Zaccheroni, G. Battistini, "Modulation of the photophysical properties of gold nanoparticles by accurate control of the surface coverage", *Langmuir* **20**, 7884 (2004).
- 164 M. H. V. Werts, H. Zaim, M. Blanchard-Desce, "Excimer probe of the binding of alkyl disulfides to gold nanoparticles and subsequent monolayer dynamics", *Photochem. Photobiol. Sci.* **3**, 29 (2004).

-
- 165 Z. Gueroui and A. Libchaber, "Single-molecule measurements of gold-quenched quantum dots", *Phys. Rev. Lett.* **93**, 166108 (2004).
- 166 S. K. Ghosh, A. Pal, S. Kundu, S. Nath and T. Pal, "Fluorescence quenching of 1-methylaminopyrene near gold nanoparticles: size regime dependence of the small metallic particles", *Chem. Phys. Lett.* **395**, 375 (2004).
- 167 E. Dulkeith, M. Ringler, T. A. Klar, J. Feldmann, A. M. Javier, W. J. Parak, "Gold nanoparticles quench fluorescence by phase induced radiative rate suppression", *Nano Lett.* **5**, 589 (2005).
- 168 N. Kometani, M. Tsubonishi, T. Fujita, K. Asami, Y. Yonezawa, "Preparation and optical absorption spectra of dye-coated Au, Ag, and Au/Ag colloidal nanoparticles in aqueous solutions and in alternate assemblies", *Langmuir* **17**, 580 (2001).
- 169 G. P. Wiederrecht, G. A. Wurtz and J. Hranisavljevic, "Coherent coupling of molecular excitons to electronic polarizations of noble metal nanoparticles", *Nano Lett.* **4**, 2121 (2004).
- 170 J. Bellessa, C. Bonnard, J. C. Plenet, J. Mugnier, "Strong coupling between surface plasmons and excitons in an organic semiconductor", *Phys. Rev. Lett.* **93**, 036404 (2004).
- 171 Y. Sugawara, T. A. Kelf, J. J. Baumberg, M. E. Abdelsalam and P. N. Bartlett, "Strong coupling between localized plasmons and organic excitons in metal nanovoids", *Phys. Rev. Lett.* **97**, 266808 (2006).
- 172 J. Zhao, L. Jensen, J. Sung, S. Zou, G. C. Schatz and R. P. Van Duyne, "Interaction of plasmon and molecular resonances for Rhodamine 6G adsorbed on silver nanoparticles", *J. Am. Chem. Soc.* **129**, 7656 (2007).
- 173 J. Zhao, L. Jensen, J. Sung, S. Zou, G. C. Schatz and R. P. Van Duyne, "Interaction of plasmon and molecular resonances for Rhodamine 6G adsorbed on silver nanoparticles", *J. Am. Chem. Soc.* **129**, 7656 (2007).

-
- 174 N. T. Fofang, T.-H. Park, O. Neumann, N. A. Mirin, P. Nordlander and N. J. Halas. “Plexcitonic nanoparticles: Plasmon-exciton coupling in nanoshell-J-aggregate complexes”, *Nano Lett.* **8**, 3481(2008).
- 175 T. K. Hakala, J. J. Toppari, A. Kuzyk, M. Pettersson, H. Tikkanen, H. Kunttu and P. Törmä, “Vacuum rabi splitting and strong coupling dynamics for surface plasmon polaritons and Rhodamine 6G molecules”, *Phys. Rev. Lett.* **103**, 053602 (2009).
- 176 A. Yoshida, N. Uchida, N. Kometani, “Synthesis and spectroscopic studies of composite gold nanorods with a double-shell structure composed of spacer and cyanine dye J-aggregate layers”, *Langmuir* **25**, 11807 (2009).
- 177 A. Yoshida, Y. Yonezawa and N. Kometani, “Tuning of the spectroscopic properties of composite nanoparticles by the insertion of a spacer layer: effect of exciton-plasmon coupling”, *Langmuir* **25**, 6683 (2009).
- 178 B. K. Juluri, M. Lu, Y. B. Zheng, T. J. Huang and L. Jensen, “Coupling between molecular and plasmonic resonances: effect of molecular absorbance”, *J. Phys. Chem. C* **113**, 18499 (2009).
- 179 W. Ni, H. Chen, J. Su, Z. Sun, J. Wang and H. Wu, “Effects of dyes, gold nanocrystals, pH, and metal ions on the plasmonic and molecular resonance coupling”, *J. Am. Chem. Soc.* **132**, 4806 (2010).
- 180 C. B. Murphy, Y. Zhang, T. Troxler, V. Ferry J. J. Martin and W. E. Jones Jr, “Probing forster and dexter energy-transfer mechanisms in fluorescent conjugated polymer chemosensors”, *J. Phys. Chem. B* **108**, 1537 (2004).
- 181 A. Ivano, “Plasmonic heating assisted deposition of bare Au nanoparticles on titania nanoshells”, *J. Coll. Interf. Sci.* **351**, 576 (2010).
- 182 M. Xiao, J. Nyagilo, V. Arora, P. Kulkarni, D. Xu, X. Sun and D. P. Davé , “Gold nanotags for combined multi-colored Raman spectroscopy and x-ray computed tomography”, *Nanotechnology* **21**, 035101 (2010).

-
- 183 J. P. Tardivoa, G. A. Del, C. S. Oliveira, D. S. Gabrielli, D. B. Tada, D. Severino, R. Turchiello and M. S. Baptista, "Methylene blue in photodynamic therapy: From basic mechanisms to clinical applications", *Photodiag. & Photodyn. Ther.* **2**, 175 (2005).
- 184 K. Das, B. Jain and H. S. Patel, "Nile blue in Triton X-100/benzene/hexane reverse micelles: A fluorescence spectroscopic study", *Spectrochim. Acta A* **60**, 2059 (2004).
- 185 W. Spencert and J. R. Sutter, "Kinetic study of the monomer dimer equilibrium of methylene blue in aqueous solution", *J. Phys. Chem.* **83**, 1573 (1979).
- 186 I. M. Villoslada, C. T. Gallegos, R. A. Hermosilla and H. Nishide, "Influence of the linear aromatic density on Methylene Blue aggregation around polyanions containing sulfonate groups", *J. Phys. Chem. B* **114**, 4151 (2010).
- 187 C. Nasr and S. Hotchandani, "Excited-state behavior of Nile Blue H-aggregates bound to SiO₂ and SnO₂ colloids", *Chem. Mater.* **12**, 1529 (2000).
- 188 A. Douhal, "Photophysics of Nile Blue A in proton-accepting and electron-donating solvents", *J. Phys. Chem.* **98**, 13131 (1994).
- 189 S. Habuchi, H. B. Kim and N. Kitamura, "Water structures in ion-exchange resin particles: solvation dynamics of Nile Blue A", *Anal. Chem.* **73**, 366 (2001).
- 190 A. I. Sherman and M. Ter-Pogossian, "Lymphnode concentrative colloidal gold following interstitial injection", *Cancer* **6** 1238 (1953).
- 191 E. C. Dreaden, M. A. Mackey, X. Huang, B. Kang and M. A. El-Sayed, "Beating cancer in multiple ways using nanogold", *Chem. Soc. Rev.* **40**, 3391(2011).
- 192 L. M. Zanolli, R. D'Agata and G. Spoto, "Functionalized gold nanoparticles for ultrasensitive DNA detection", *Anal. Bioanal. Chem.* **402**, 1759 (2012).
- 193 X. Cao, Y. Ye and S. Liu, "Gold nanoparticle-based signal amplification for biosensing", *Anal. Biochem.* **417**,1 (2011).

-
- 194 M. A. Sayed and S. H. Bokhari, "Gold nanoparticle based microbial detection and identification", *J. Biomed. Nanotechnol.* **7**, 229 (2011).
- 195 L. Tong, Q. Wei, A. Wei and J.-X. Cheng, "Gold nanorods as contrast agents for biological imaging: optical properties, surface conjugation and photothermal effects" , *Photochem. & Photobiol.* **85**, 21 (2009).
- 196 X. Huang, I. H. El-Sayed, W. Qian, and M. A. El-Sayed, "Cancer cell imaging and photothermal therapy in the near-infrared region by using gold nanorods", *J. Am. Chem. Soc.* **128**, 2115 (2006).
- 197 C. H. Chou, C.D. Chen and C. R. C. Wang, "Highly efficient, wavelength-tunable, gold NP based optothermal nanoconvertors", *J. Phys.Chem. B* **109**,11135 (2005).
- 198 S. Wang, W. Lu, O. Tovmachenko, U. S. Rai, H. Yu and P. C. Ray, "Challenge in understanding size and shape dependent toxicity of gold nanomaterials in human skin keratinocytes", *Chem. Phys. Lett.* **463**, 145 (2008).
- 199 E. E. Connor, J. Mwamuka, A. Gole, C. J. Murphy and M. D. Wyatt, "Gold nanoparticles are taken up by human cells but do not cause acute cytotoxicity", *Small* **1**, 325 (2005).
- 200 T. S. Hauck, A. A. Ghazani and W. C.W. Chan, "Assessing the effect of surface chemistry on gold nanorod uptake, toxicity, and gene expression in mammalian cells", *Small* **4**, 153 (2008).
- 201 G. V. Maltzahn, J.-H. Park, A. Agrawal, N. K. Bandaru, S. K. Das, M. J. Sailor and S. N. Bhatia, "Computationally guided photothermal tumor therapy using long-circulating gold nanorod antennas", *Cancer Res.* **69**, 3892 (2009).
- 202 J. L. Burt, C. Gutierrez-Wing, M. Miki-Yoshida and M. Jose-Yacaman, "Noble-metal nanoparticles directly conjugated to globular proteins", *Langmuir* **20**, 11778 (2004).

-
- 203 G. Schneider, G. Decher, N. Nerambourg, R. Praho, M. H. V. Werts and M. Blanchard-Desce, “Distance-dependent fluorescence quenching on gold nanoparticles ensheathed with layer-by-layer assembled polyelectrolytes”, *Nano Lett.* **6**, 530 (2006).
- 204 T. L. Jennings, M. P. Singh and G. F. Strouse, “Fluorescent lifetime quenching near $d=1.5$ nm gold nanoparticles: probing NSET validity”, *J. Am. Chem. Soc.* **128**, 5462 (2006).
- 205 E. A. Dulkeith, A. C. Morteani, T. Niedereichholz, T. A. Klar and J. Feldmann, “Fluorescence quenching of dye molecules near gold nanoparticles: Radiative and nonradiative effects”, *Phys. Rev. Lett.* **89**, 203002 (2002).